Sensing of Heavy Metal Ions via Fluorescence Quenching of Femtosecond-Laser-Synthesized Nanoparticles

by

Ahmed Mohamed Shahin

A thesis
presented to the University of Waterloo
in fulfillment of the
thesis requirement for the degree of
Master of Applied Science
in
Mechanical and Mechatronics Engineering (Nanotechnology)

Waterloo, Ontario, Canada, 2020

AUTHOR'S DECLARATION

I hereby declare that I am the sole author of this thesis. This is a true copy of the thesis, including any required final revisions, as accepted by my examiners.

I understand that my thesis may be made electronically available to the public.

Abstract

Nanoparticles (NPs) for sensing of heavy metal ions (HMIs) via fluorescence quenching are becoming sought-after for their facile synthesis, cost effectiveness, and high degree of tunability. In this thesis, the sensitive and selective fluorescence-quenching detection of the four most toxic HMIs (Hg, Pb, Cd, and As), as listed by the World Health Organization (WHO), is demonstrated using femtosecond (fs)-laser-treated nanoparticles.

A fs laser is used to exfoliate 2D flakes of nitrogen-doped graphene oxide (NGO) and molybdenum disulfide (MoS_2) dissolved in acetonitrile and a 1:1 ethanol-water mixture and convert them into NPs. The chemically active NPs bond with atoms from the laser-dissociated acetonitrile (CH_3CN), ethanol (C_2H_5OH), and water (H_2O) molecules to form solvent-functionalized NPs, which are characterized by absorption spectroscopy, photoluminescence (PL) spectroscopy, Raman spectroscopy, X-ray photoelectron spectroscopy (XPS), and transmission electron microscopy (TEM).

The high degree of functionalization of the 2D NPs with nitrogen, oxygen, hydrogen, and carbon groups allowed highly sensitive detection of HMIs owing to binding and charge transfer between the HMIs and functional groups, which reduces the excess carriers associated with the functional groups and leads to quenching of the nanoparticles' PL. Selective sensing of the HMIs using the NP solutions is attributed to the different bond polarities associated with the different combinations of NPs and functional groups, which electrostatically attract HMIs with different affinities. The functional groups responsible for sensing HMIs selectively are studied by Fourier transform infrared spectroscopy (FTIR) and PL lifetime decay of the NPs before and after the addition of HMIs.

The method demonstrated here is faster than most previous techniques for functionalizing 2D NPs. The tunable functionalization enables sensitive and selective detection of the four most toxic HMIs with limits of detection (LOD) three times lower than the safe concentration limits of the HMIs in water.

Acknowledgements

In the first place, I would like to express my gratitude to Professor Kevin Musselman for expanding my academic potential. Your professionalism, organization, academic insight, and reachability taught me a lot on the academic and personal level. I was lucky to have you as my supervisor and team leader during my master's degree; this experience added a lot to my knowledge and personal growth. I would also like to thank Professor Joseph Sanderson and his team for their collaboration and reachability.

I would like to thank my funding sources: WIN and TQT. Your trust is appreciated; it made the completion of my project easier.

I'm very thankful to my team members for making my masters journey a unique experience by adding academic intuition and fun memories. I would like to personally thank Khaled Ibrahim for helping me learn most of the lab and intuitive skills that aided the completion of my degree. However, I'm more grateful for the quality time and the support you have always offered me, making this friendship unique.

Walking with a friend in the dark is better than walking alone in the light. My chosen family, Mahmoud Nasr and Ahmed Mamdouh, were the most supportive and collaborative ones in my journey; thank you is not enough. I'm very thankful for my friend Yasmeen Tarek for her support and the scientific intuition she helped with. I'm also very thankful for my lifelong friends Bassel Shehata, Mahmoud Hussein, Ahmed Elkashif, and Islam Abdelhadi for being constantly encouraging. Words are never enough to thank my closest friend and lifelong supporter Abdullah Amr; you stood by me in thick and thin. Last but never least, I would like to express my warm gratitude to my best friend Layla Umara for being an essential factor of support and encouragement.

Most significantly, home is where you are loved the most. I would like to express my cordial acknowledgement that my family is behind any successful step I take in life. I'm happily thankful for my mother Eman Youssef, and my lovely sisters Dina and Rinad Shahin for believing in me; your younger brother is making you proud finally. I would also like to thank my grandpa Youssef Abdalla for being my mentor and role model. Above all else, I would like to thank my late father, best friend, idol, and guardian angel Mohamed Shahin. I would have never been the person I'm today without you being my father; you are a blessing. You left, but your love and support are still with me.

Dedication

To my father in heavens, I made it solely for you. I dedicate this work to your loving soul; I know you are proud now.

Table of Contents

List of Figures

List of Tables

Chapter 1
Introduction

1.1 Chemical Sensing

Toxic HMIs are one of the main concerns of the WHO as they represent a major threat to many aquatic and human lives (Rasheed *et al.*, 2018). The WHO announced "ten chemicals of major public concern" including four toxic heavy metals (Arsenic, Cadmium, Lead, and Mercury). HMIs are discharged in water through several industries including pesticides (Carolin *et al.*, 2017), mining (Rasheed *et al.*, 2018), electroplating, microelectronics, and batteries (Vilela *et al.*, 2016). Irrigation water contaminated with HMIs affects the soil productivity and can be toxic to many plants at very low concentrations (Elgallal, Fletcher and Evans, 2016). HMIs' non degradability makes them capable of disrupting the human central nervous system's functionality. They accumulate in human fatty tissues, so even very low concentrations of HMIs can accumulate gradually and affect human health (Jiang *et al.*, 2018).

Methods of detection and extraction of HMIs in water are being developed to save aquatic life and improve human health. Atomic absorption spectroscopy (AAS) can detect HMIs (Kunkel and Manahan, 1973) through assessing the analytes in the sample from its atomic absorption spectrum (Culver and Surles, 1975). AAS uses the wavelengths absorbed by the sample to study their correspondence to the energies needed to excite electrons from the ground state to the higher energy level to determine the analyte (Levenson *et al.*, 2001). Inductively coupled plasma mass spectrometry (ICP-MS) is another technique that atomizes the samples into ions, including HMIs, and quantifies their concentrations (Dressler, Pozebon and Curtius, 1998). A fine aerosol of the samples is formed after injecting the liquid sample in the system, then the aerosol is transferred to the argon plasma (Wilschefski and Baxter, 2019). A high temperature plasma atomizes the liquid sample and generates ions that are extracted and focused by electrostatic lenses into a mass analyzer to separate ions according to their mass to charge ratio (Wilschefski and Baxter, 2019). However, a lot of setup and sample preparation steps are needed to minimize the interference in the ICP-MS signal with other polyatomic ions (Shih *et al.*, 2016). Electrochemical sensing, unlike AAS and ICP-MS, is an on-site technique that can detect HMIs. Electrochemical sensors are compact devices with working electrodes made of metal oxides, polymers, nanomaterials, carbon nanotubes, or even mercury (Bansod *et al.*, 2017). They can detect HMIs by generating a clear detectable electrical signal based on the water contaminant by passing current

through the water sample (Bansod *et al.*, 2017). Different HMIs concentrations are added to make a concentration versus current calibration curve (Buzica *et al.*, 2006). This curve can determine different HMIs concentrations along with the limit of detection (LOD), which is the lowest sensible analyte concentration based on a statistical analysis of experimental results (Needleman and Romberg, 1990). The drawback of electrochemical sensing is poor sensitivity, unlike ICP-MS (Bansod *et al.*, 2017). Fluorescence sensors offer an alternative solution of sensing HMIs on-site with high sensitivity, on the order of few nano molars (nM), which is in the range of the safe limit of HMIs in water (Guo, Zhou and Yang, 2017). Fluorescence sensors include a host material that can interact or bond with the HMIs. Upon binding with the HMIs, the fluorescence signal changes from the blank measurement due to changes in the electronic structure of the host material. Fluorescent sensors can operate by quenching or turning on the fluorescence of the host material.

2D nanomaterials are currently being utilized as fluorescence chemical sensors with very high sensitivity and stability. Graphene oxide (GO), black phosphorus (BP), and transition metal dichalcogenides (TMDs) have been used in many chemical sensing applications for their high surface areas that aid sensing (Ravikumar *et al.*, 2018), (Jiang *et al.*, 2015). 2D nanomaterials can be functionalized by several dopants to facilitate compatibility in different media and enhance their chemical structures to bind with HMIs with high sensitivity and selectivity (Long *et al.*, 2013). Graphene has a honeycomb structure with sp^2 hybridized carbon atoms that allow long-range weak forces to bind with HMIs. Likewise, transition metal dichalcogenide monolayers (TMDs) have a honeycomb-like structure with an active basal plane that allow van der Waals forces to detect HMIs (Lee, Suh and Jang, 2019). Inducing defects in 2D nanomaterials like GO, BP, and TMDs can modify their surfaces' reactivity. Surface chemistry modifications can be tuned to detect HMIs with high sensitivity and selectivity (Ping *et al.*, 2017).

2D nanomaterials utilized as fluorescence sensors can be in the form of sheets (Ravikumar *et al.*, 2018) composites (Su, Chen and Fan, 2018), and NPs (Lin *et al.*, 2019). Size reduction of bulk sheets to NPs changes the electronic structure of the 2D nanomaterials to be more absorbing and fluorescent, which enhances their sensing accuracy (Chen, 2008). However, current fabrication methods for 2D NPs require many steps with high operating temperatures and are not time efficient. Furthermore, few studies have addressed the selectivity of 2D NP sensors towards different HMIs. Lin *et al.*, 2019 modified the surface of MoS_2 NPs with different functional groups to selectively sense Cd, Pb, and Co.

However, a selective sensing study of the four most dangerous HMIs (As, Cd, Pb, Hg) has not been demonstrated with 2D NPs.

A femtosecond (fs) laser technique that was previously reported by our group can produce 2D NP solutions with flexible functionalization tunability without high operating temperatures and long synthesis times (Ibrahim *et al.*, 2018). The NPs can be functionalized by the solvent used, resulting in modification of the surfaces of the NPs with atoms of different electronegativities to selectively sense different HMIs. This thesis leverages this quick fs laser technique to synthesize NGO, MoS_2, and BP 2D NPs that are utilized as fluorescence chemical sensors with high selectivity and sensitivity for HMI detection. The fs laser technique simultaneously reduces the size of the 2D flakes to produce NPs and functionalizes the NPs with different functional groups to enhance their sensitivity and selectivity towards the four most toxic HMIs.

1.2 Thesis overview

Chapter 2 will discuss previously reported properties of NGO, MoS_2, and BP, along with their capabilities in sensing HMIs. The NPs solutions are designed to be on-site fluorescence sensors with high sensitivity and selectivity. This application requires highly absorbing and fluorescent NP solutions that are stable in water. Chapter 3 will outline the fs technique that was used to synthesize the NP solutions in acetonitrile and a 1:1 mixture of ethanol-water, as well as the techniques used to characterize the NPs and test the sensing performance. The detailed characterization of the NP solutions and the results of the sensing experiments will be discussed in Chapter 4. Lastly, Chapters 5 and 6 will summarize the conclusions of the thesis and discuss areas for future work, respectively.

Chapter 2

Properties of two-dimensional materials for sensing

2.1 Properties of the 2D sensing materials

Graphene is a 2D allotrope of carbon with a hexagonal lattice consisting of carbon atoms only (Xia *et al.*, 2009). Graphene is a semi-metal with zero bandgap, limiting its usage in electronic devices (Bai *et al.*, 2010). Different approaches for opening a bandgap in graphene have been demonstrated and it became a successful candidate for many devices (Balog *et al.*, 2010), (Zhou *et al.*, 2007), (Dvorak, Oswald and Wu, 2013). GO is a chemical derivative of graphene and the term oxide refers to the oxygen functional groups attached to it. Figure 1 illustrates the graphene and GO structures. GO is formed by strong oxidation of graphite and has a high tendency to be exfoliated into sheets that can be used in various applications when used as a monolayer (Robinson *et al.*, 2008). Furthermore, oxygen functional groups allow graphene to be hydrophilic. Such hydrophilicity allows GO to be used in water-compatible applications (Fan *et al.*, 2016). The emergence of graphene and graphene oxide in the field of devices and sensors engenders interest in TMDs and BP as they exhibit similar properties (Chhowalla, Liu and Zhang, 2015).

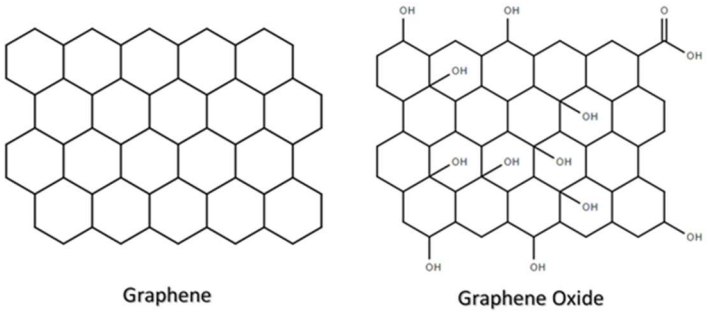

Figure 1. Graphene and graphene oxide sheets structures.

TMDs are a set of materials with the main formula MX_2, where M is a group 4-7 transition metal and X is a chalcogen from group 16 elements (oxygen, sulfur, selenium, tellurium, polonium, livermorium). Bulk TMDs have strong planar bonds and weak stack bonding among their layers (Chhowalla, Liu and Zhang, 2015). A TMD structure consists of a transition metal encapsulated between two chalcogen

atoms to form a hexagonal structure (Chhowalla, Liu and Zhang, 2015). MoS_2, a TMD, can acquire different 2D structures: 1T, 2H, and 3R. 1T consists of one layer of Mo atoms sandwiched between two S atoms in a hexagonal structure, 2H is a stack of 1T layers that are aligned to show a hexagonal structure from the top view, and 3R is a misaligned stack of hexagonal 1T sheets (Toh *et al.*, 2017), as shown in Figure 2.

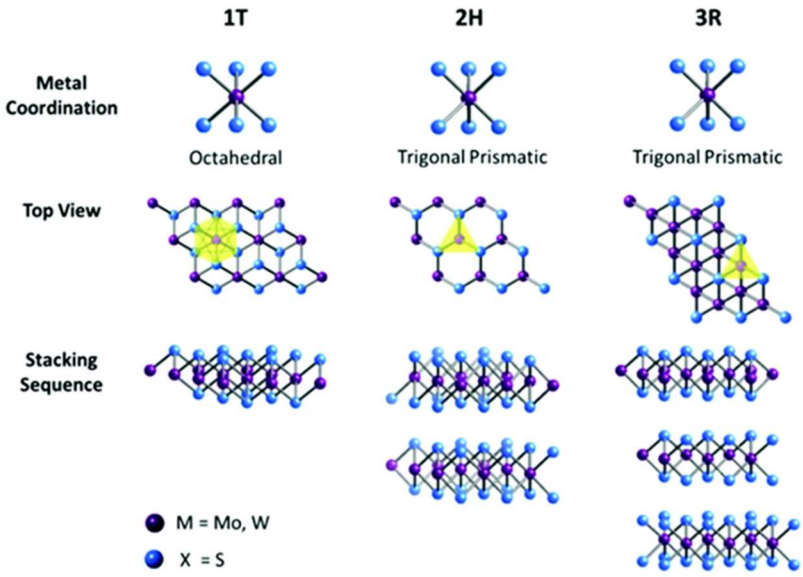

Figure 2. Different MoS_2 sheets atomic arrangements (Toh *et al.*, 2017) - Published by The Royal Society of Chemistry.

BP is the most stable allotrope of phosphorus (Xia, Wang and Jia, 2014). Its structure is stacked layers of puckered honeycombs that are weakly linked together, as shown in Figure 3. Each phosphorus atom is bonded to three other neighboring phosphorus atoms, taking all three valence electrons of phosphorus (Li *et al.*, 2014). BP has a unique structure that gives it anisotropic properties (Chen *et al.*, 2017). Intensive efforts have been attempted in utilizing BP in many applications including field-effect transistors (Buscema *et al.*, 2014), photodetectors (Engel, Steiner and Avouris, 2014), and optoelectronics (Miao, Zhang and Wang, 2019) due to its unique properties in its monolayer form.

These materials have tunable physical and chemical properties that make them strong candidates for various applications. The high surface-area-to-volume ratio of the 2D materials give them unique

sensing abilities, especially in chemical sensing (O'Brien *et al.*, 2014). Moreover, 2D materials possess advantageous electrical, optical, and mechanical properties that allows them to be fabricated as sensing devices (Akinwande *et al.*, 2017). Tuning of the properties of GO, TMDs, and BP can exploit new capabilities and limits in sensing applications (Anichini *et al.*, 2018).

Like all materials, 2D materials have defects according to the second law of thermodynamics. Defects in 2D materials can occur naturally or be induced artificially to modify their properties (Banhart, Kotakoski and Krasheninnikov, 2011). Dopant atoms can be introduced into the 2D material to change its properties. Vacancies are a type of defects that can alter the chemical, physical, electronic, and mechanical properties of materials (Akinwande *et al.*, 2017). Although NGO, TMDs, and BP are 2D materials with similar properties, the difference in their lattice structures and bonding energies can play an important role in how the defects alter the material's properties (Akinwande *et al.*, 2017).

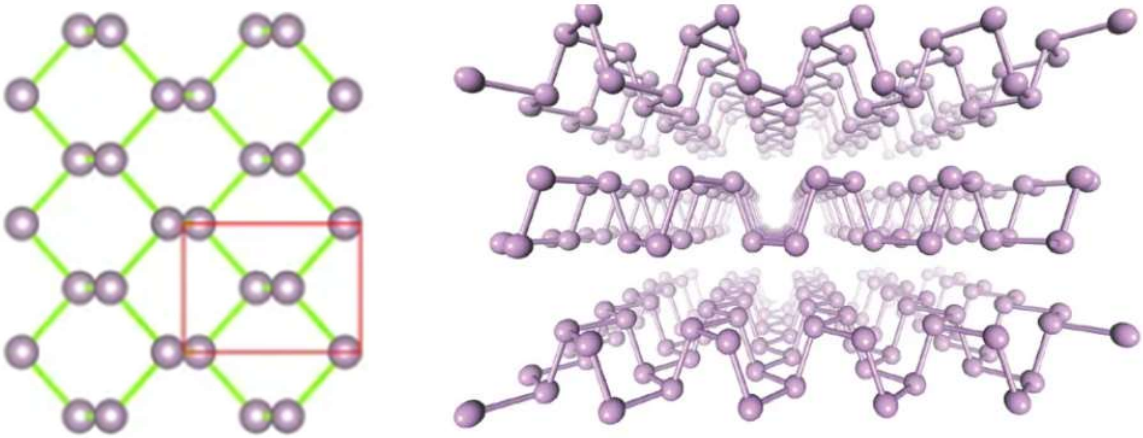

Figure 3. BP lattice and atomic arrangement (Li *et al.*, 2014) – Published by Springer Nature.

2.1.1 Nitrogen-doped graphene oxide properties

The structure of 2D materials facilitates the introduction of defects and the modification of material properties via doping. Graphene has superior material properties and its strength lies in the ability to modify its properties depending on the desired application. For instance, doping graphene with nitrogen can change its electronic properties, chemical reactivity, and electrocatalytic activity (Yang *et al.*, 2012). Nitrogen-doped graphene (NG) and NGO promote the electric conductivity of graphene since nitrogen is more electronegative than carbon. The electronegativity difference makes adjacent carbon

atoms lose electrons, thus n-doping the graphene (Wu *et al.*, 2016). Nitrogen doping of graphene can induce defects in different locations in the graphene sheets. Different properties and functions can arise according to the number of dopant atoms and their locations (Zhang, Xia and Dai, 2015). Graphitic, pyridinic, and pyrrolic nitrogen are the three main configurations of nitrogen. Pyridinic nitrogen is located at the edges of the carbon hexagons and is bonded with two sp^2 carbon atoms. Graphitic nitrogen, or quaternary nitrogen, is bonded with two carbon atoms to join the honeycombs together, and pyrrolic nitrogen is a nitrogen atom connected to two carbons atoms, present in five-sided honeycombs as seen in Figure 4. Controlling the doping sites is a hard task because the nature of doping is not uniform and is unpredictable. However, some techniques using covalent organic polymer precursors have more control over the configuration of nitrogen doping in graphene (Xiang *et al.*, 2014).

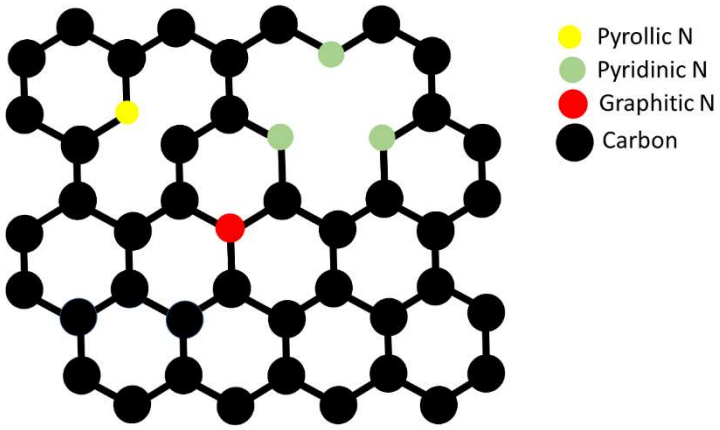

Figure 4. Pyrollic, pyridinic, and graphitic nitrogen-graphene binding configurations.

2.1.2 Transition metal dichalcogenides properties

TMDs, especially group 6 TMDs, are well-known for their superior stability and utilization in various applications (Schmidt, Giustiniano and Eda, 2015). The usual bandgap of group 6 TMDs is layer-dependent in the range of 1 – 2 eV (Schmidt, Giustiniano and Eda, 2015). TMDs in their bulk state have an indirect bandgap (Terrones, López-Urías and Terrones, 2013). Their weakly linked layers can be exfoliated via mechanical or chemical processes to obtain single sheet or monolayer TMDs (Berkelbach, Hybertsen and Reichman, 2013). Due to the charge confinement in only two dimensions, monolayer TMDs possess totally different characteristics in comparison with their bulk forms. The

main change is the transformation from an indirect bandgap to a direct one (Chhowalla, Liu and Zhang, 2015).

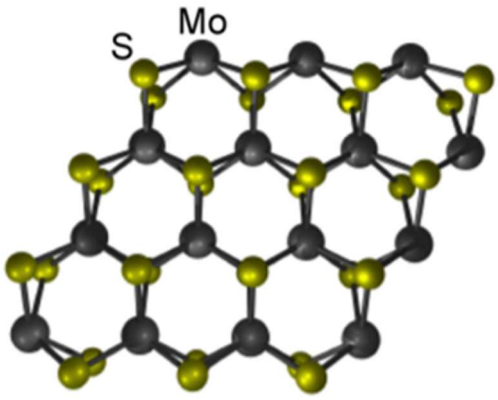

Figure 5. MoS_2 atomic arrangement (Schmidt, Giustiniano and Eda, 2015) – Reproduced by permission of the Royal Society of Chemistry.

Dual element 2D materials like MoS_2 shown in Figure 5 can have vacancies from the absence of either Mo or S. In contrast, GO and BP can have only one type of vacancy, which is the absence of a carbon or a phosphorus atom, respectively (Kiraly *et al.*, 2017). The probability of occurrence of vacancies depends exponentially on the formation energy, where lower formation energy leads to higher defect probability (Akinwande *et al.*, 2017).

Table 1. 2D material formation energy, depicting the occurrence probability of defects

Material	Graphene	MoS_2	BP
Formation Energy (eV)	7.57 (Cai *et al.*, 2016)	1.22 - 2.25 (Zou, Liu and Yakobson, 2013)	1.65 (Cai *et al.*, 2016)

According to Table 1, it is easier to create defects in MoS_2 and BP than in graphene. The ability to introduce defects has triggered the utilization of TMDs and BP in many applications based on how the materials are engineered.

The honeycomb structure of TMDs and graphene allows dopants to reside above the centers of the repetitive hexagonal structures (Fang *et al.*, 2013). This type of doping doesn't depend on the vacancy energy of formation. For example, (Fang *et al.*, 2013) doped MoS_2 and graphene with potassium to enhance their electrical properties, where the potassium atoms reside above the center of some of the hexagonal units, as shown in Figure 6.

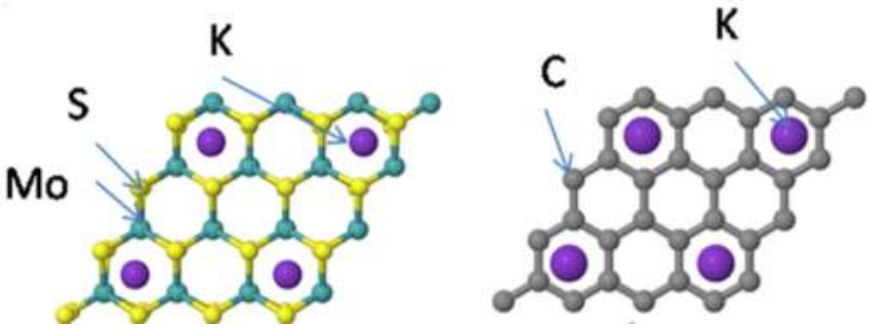

Figure 6. Potassium atom dopants residing above the hexagonal centers of MoS_2 (left panel) and graphene (right panel) Reprinted with permission from (Fang *et al.*, 2013). Copyright (2020) American Chemical Society.

2.1.3 Black phosphorus properties

BP has also been investigated thoroughly owing to its excellent material properties. However, BP is unstable in humid air and water (Musselman, Ibrahim and Yavuz, 2018). Upon exposure to water, BP degrades first by the appearance of some bumps that can be seen through atomic force microscopy (AFM), then the bumps form large droplets that confirm the degradation of BP and its transformation into phosphoric acid (Favron *et al.*, 2015). The instability of BP limits the number of applications it can be used in. However, doping BP with sulfur (Lv *et al.*, 2018), titanium sulfonate (Zhao *et al.*, 2016), and other functional groups enhance its environmental stability. The role of the dopants is to transfer charges with BP to prevent it from actively forming oxygen bonds (Musselman, Ibrahim and Yavuz, 2018). Exfoliating the bulk BP to monolayer increases the bandgap due to quantum confinement (Li *et al.*, 2015). More layers lead to a smaller direct bandgap at the Z point, while exfoliating BP into a single

layer produces a direct bandgap of around 2 eV at the Γ point. The number of BP layers control the bandgap (0.3 – 2) eV and carrier mobility values up to 1000 $cm^2 V^{-1}s^{-1}$ are obtained in monolayer BP (Li *et al.*, 2014).

Lopez-Bezanilla, 2016 discussed that doping BP can be achieved through substitution of phosphorus with nitrogen dopants, as illustrated in Figure 7(a). The defective nature of BP can also aid the intercalated doping of BP with atoms that fit in the defective sites (Lopez-Bezanilla, 2016). Vacancies in the BP lattice can correspond to the removal of a single phosphorus atom (see Figure 7(b)) or two phosphorus atoms (Figure 7(c)), which is called a di-vacancy in the latter case.

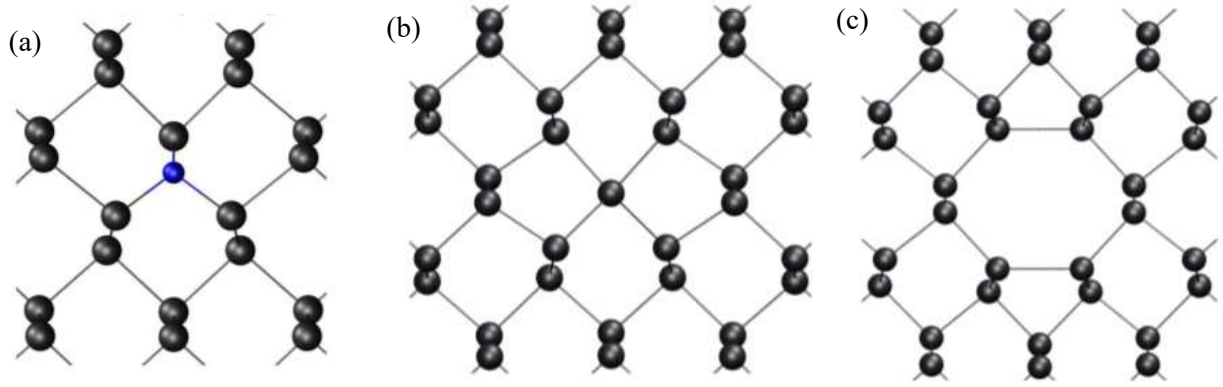

Figure 7. BP (a) nitrogen doping, (b) single vacancy, and (c) di-vacancy. (Lopez-Bezanilla, 2016) (https://doi.org/10.1103/PhysRevB.93.035433)

2.2 Two-dimensional nanoparticles

Decreasing the dimensions of 2D sheets to the scale of NPs led to the exploration of different functionalities and properties due to quantum confinement (Khan, Saeed and Khan, 2019)(Jayanthi *et al.*, 2007). Quantum confinement, due to size reduction, decreases the number of allowed states and shifts the energy levels resulting in an increase in the band gap, more discretization of energy levels, and the emergence of multiple peaks in the absorption spectra (Chen, 2008). NPs are used in drug delivery systems (De Jong and Borm, 2008), cancer cell detection (Conde, Doria and Baptista, 2012), and chemical sensing (Thakar, Chen and Snee, 2007), among other applications. Materials that can be synthesized into 2D NPs include TMDs, graphene or carbon, GO, BP, silica, antimonene, bismuthine,

etc. The 2D NPs can have different properties based on the synthesis technique (Dong *et al.*, 2016)(Buso *et al.*, 2008), giving another degree of freedom in tuning the materials' properties.

2.2.1 Optical and structural properties of two-dimensional nanoparticles

In addition to the properties of 2D NPs discussed in the previous section, size reduction to NPs enhances their optical properties for many applications including optoelectronics (Dong *et al.*, 2016) and optical sensors (Chen, 2008) with very high sensitivity. As discussed in the previous section, the size reduction of TMDs alters the bandgap from indirect to direct, which applies to TMD NPs as well (Zhang *et al.*, 2014). The multiplicity and elevated intensity of the absorption peaks lead to multiple and high intensity PL peaks as observed in the work of (Thirumalai, Jagannathan and Trivedi, 2007) that emphasize the superb optical properties of 2D NPs. Quantum confinement slows down the electronic relaxation, hence increasing the photoluminescence quantum yield (PLQY) (Dong *et al.*, 2016)(Amani *et al.*, 2015), which is the ratio of the photons emitted to the photons absorbed (Amani *et al.*, 2015). The overlap between the electron and hole wavefunctions increases upon the size reduction, yielding higher radiative recombination rates and stronger luminescence (Chen *et al.*, 1997).

Due to the highly reactivity nature of NPs, functionalizing them with multiple ligands is typically part of their synthesis process (He, Gao and Ma, 2013). The functionalization step promotes the compatibility of the NPs in different media. Some sensing and detection applications require biocompatibility (Shi *et al.*, 2007) or water-compatibility (Ma *et al.*, 2015), which is possible by the attachment of the appropriate functional groups to the NPs' surfaces. The NPs can be made stable in water via functionalization with oxygen functional groups (Liu *et al.*, 2017). GO, BP, and TMD NPs are used in sensing HMIs due to the tunable nature of the surface functional groups. The NPs are also more stable, absorbent, and fluorescent when compared to their parent bulk material. Accordingly, their utilization as fluorescent HMIs sensors can produce highly sensitive and selective results. Sensing selectivity is achievable by functionalizing the 2D NPs with various functional groups that are expected to have different affinities towards HMIs. Moreover, NPs' enhanced optical properties can play a vital role in achieving high sensing sensitivity (low LOD), allowing NPs to be strong candidates for early HMIs detection.

NGO

The absorption spectrum of GO QDs shown in Figure 8(a) possesses two main characteristic peaks at 234 and 320 nm. The 234 nm peak corresponds to π-π^* transitions of aromatic groups in the sp^2 domain and the 320 nm shoulder is attributed to n-π^* transitions in the sp^3 domain (Bhargava and Khan, 2018). Bhargava and Khan, 2018 found the band gap of GO QDs to be ~2.1 eV based on the Tauc plot of the absorption spectrum of GO, as shown in Figure 10(b). The PL spectrum of GO QDs is excitation-dependent, where it can be seen in Figure 8(c) that different excitation wavelengths produce peaks with various intensities and slight red or blue shifts (Gao *et al.*, 2019). Tuning the optical properties of GO QDs is possible by modifying their surfaces' chemistry by attaching several functional groups (Gao *et al.*, 2019). The nitrogen doping alters the absorption and band gap of GO QDs, leading to a shifted PL spectrum as shown in Figure 8(c).

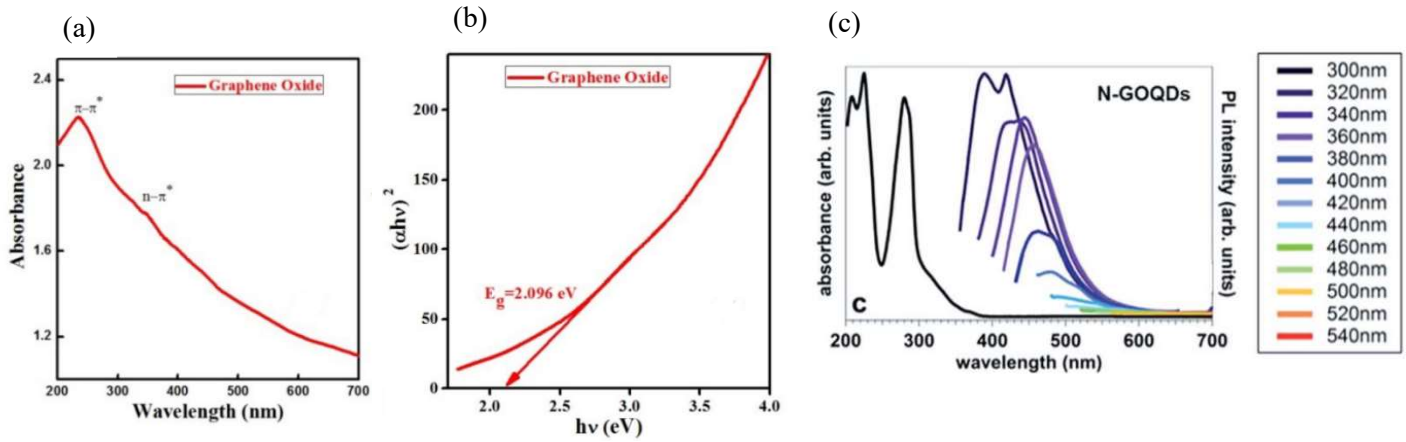

Figure 8. GO (a) absorption spectrum, (b) bandgap. "Bhargava and Khan, Structural, optical and dielectric properties of graphene oxide, Vol. 1953, 030011, (2018) (c) absorption and PL spectra of NGO QDs Reproduced from Ref. (Gao *et al.*, 2019) with permission from The Royal Society of Chemistry.

Doping GO with nitrogen alters its Raman spectrum and X-ray photoelectron spectrum by incorporating new nitrogen bonds and by increasing the number of defects. The Raman spectrum of pristine GO QDs possesses two main peaks: D (1348 cm^{-1}) and G (1588 cm^{-1}) peaks that correspond to the defects in the carbon domain and a phonon mode of the sp^2 carbon domain, respectively as shown in Figure 9. A 2D peak is also observed in the Raman spectra of graphene and GO, which is a second order Raman scattering process (Yadav and Dixit, 2017). The D and G intensities ratio, I_D/I_G, can be

used to characterize the defective nature of the material, where a higher ratio corresponds to a more defective domain (Yadav and Dixit, 2017). Figure 10(a) shows a previously reported XPS spectrum of NGO QDs, where the C1s, N1s, and O1s peaks have been highlighted. The C1s XPS spectrum of the NGO QDs presented in Figure 10(b) has major peaks at 284.6, 285.6, 286.5, 287.5, and 288.9 eV that correspond to C–C, C–N, C–O, C=O, and O–C=O bonds, respectively (Yeh *et al.*, 2014). The N1s spectrum in Figure 10(c) has three main characteristic peaks owing to pyridinic (398.1 eV), pyrrolic (399.6 eV), and quaternary or graphitic (400.9 eV) nitrogen atoms (Yeh *et al.*, 2014).

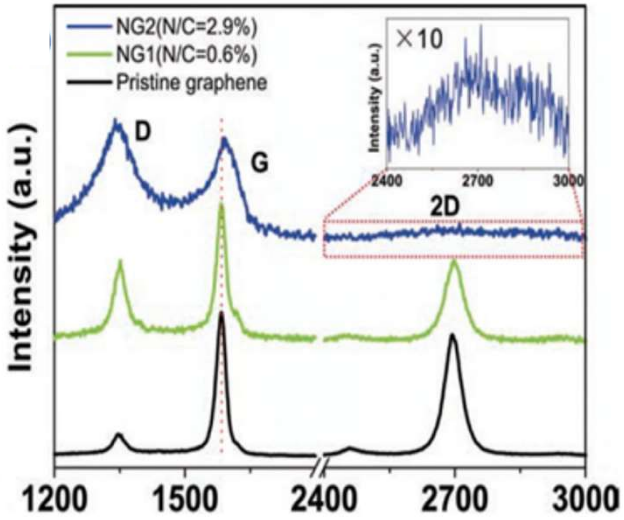

Figure 9. Increase of defective nature of graphene sheets doped with nitrogen using different nitrogen compositions observed by Raman spectroscopy. (Yadav and Dixit, 2017) by permission from Elsevier.

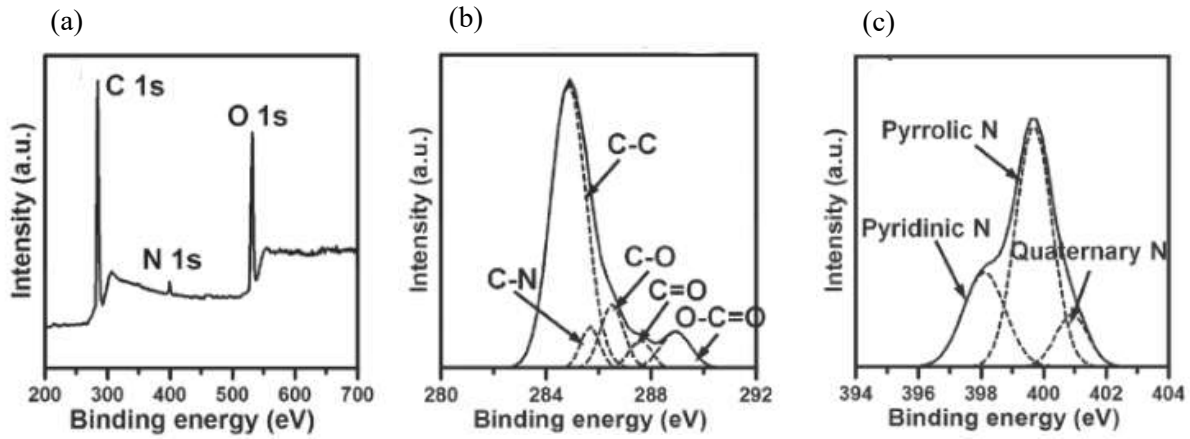

Figure 10. NGO QDs XPS spectra (a) survey, (b) C 1s, and (c) N 1s Reprinted from (Yeh *et al.*, 2014) by permission from Wiley.

TEM images of NGO QDs obtained by (Yeh *et al.*, 2014) are shown in Figure 11. The QDs averaged a particle size of 8 nm with a lattice spacing of 0.21 nm, which corresponds to the $\{1\bar{1}00\}$ planes of graphene. Different zones can be seen on the same particle, which is due to different atomic arrangements. This can be attributed to irregular doping or stress formed during the characterization procedure.

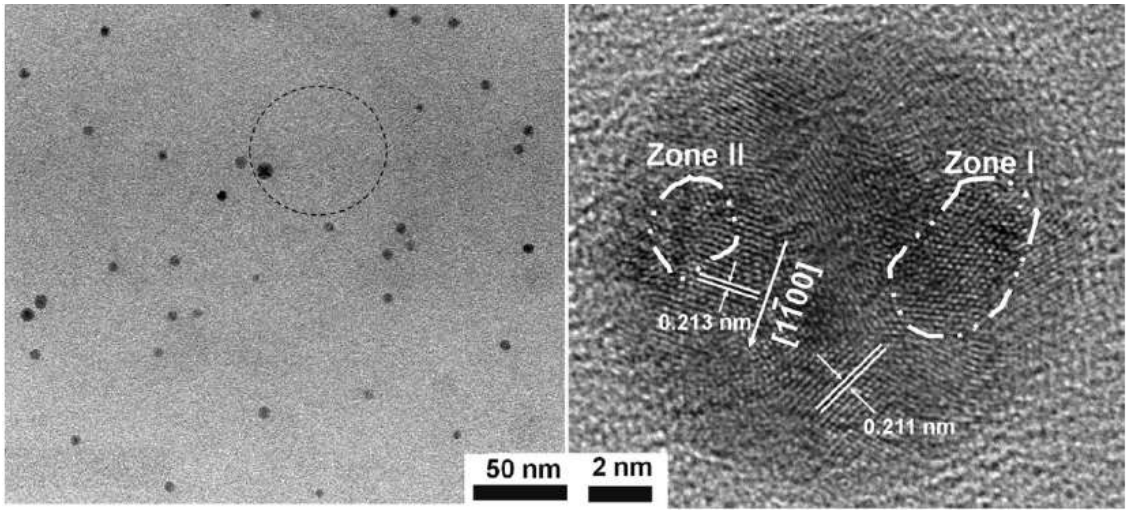

Figure 11. TEM images of NGO QDs showing different lattice spacings owing to intrinsic graphitic domains and carbon nitrogen bonds Reprinted from (Yeh *et al.*, 2014). by permission from Wiley.

MoS_2

The absorption spectrum of MoS_2 NPs presented by Zhao *et al.*, 2017 showed two characteristic peaks at 230 and 301 nm that can be attributed to the excitonic transitions of the MoS_2 NPs (Ibrahim *et al.*, 2018). The PL features of MoS_2 NPs are also excitation wavelength dependent like NGO, as seen in Figure 12(a). It can be seen in Figure 12(b) that the absorption spectra of MoS_2 flakes (black curve) and ethanol-water functionalized NPs (red curve) differ significantly. The A and B peaks are attributed to excitonic transitions in the MoS_2 flakes, while their intensities are reduced and the spectrum is red-shifted due to quantum confinement in the NPs (Ibrahim *et al.*, 2018). The absorption and PL features of MoS_2 NPs also depend on the functional groups attached to their periphery. Due to the introduction of carbon domains and the size reduction from flakes to NPs in Figure 12(b), the main peak of the MoS_2 flakes (C peak) blueshifts to 260 nm (Ibrahim *et al.*, 2018) and a F peak is present in the PL spectrum, which is attributed to the carbon domains.

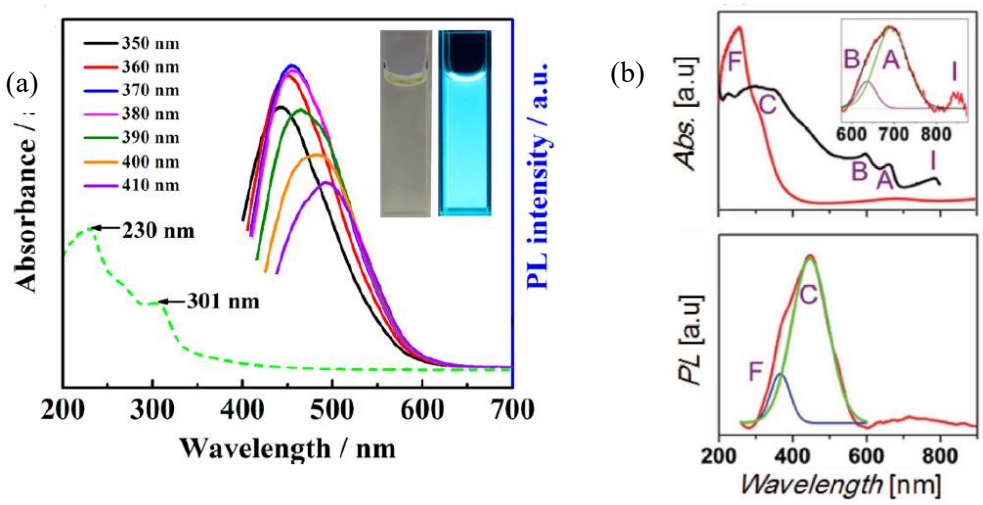

Figure 12. (a) Excitation dependent PL of MoS2 QDs. Reprinted (adapted) with permission from (Zhao *et al.*, 2017). Copyright (2018) American Chemical Society. (b) Absorption spectrum of bulk MoS_2 (black curve) and functionalized MoS_2 NPs (red curve). The PL spectrum of MoS_2 NPs with the green curve resembling the blue emission peak of MoS_2 NPs and the blue curve represented the carbon domains attached to the surface of the NPs. Reprinted from (Ibrahim *et al.*, 2018) by permission from Wiley.

Functionalization of MoS_2 NPs has also been confirmed by Ibrahim *et al.*, 2018 and Zhang *et al.*, 2018 via Raman spectroscopy. MoS_2 NPs possessed in-plane E_{2g} and out-of-plane A_{1g} vibrational modes like their bulk form. The vibrational modes were redshifted due to the functional groups-induced vibration softening (Ibrahim *et al.*, 2018). New peaks were observed in the Raman spectrum owing to the functional groups. In Figure 13(a), a Mo-O peak and D+G peak can be seen to appear for carbon- and oxygen-functionalized MoS_2 NPs (f-MoS_2). The D+G peak was observed in the Raman spectrum of NGO presented earlier. The XPS spectra of the pristine MoS_2 flakes and carbon- and oxygen-functionalized MoS_2 NPs in lower panel of Figure 13(b) also depict the influence of functionalization, as a variety of new bonds associated with carbon and oxygen appear, confirming that the properties of the MoS_2 NPs have been changed.

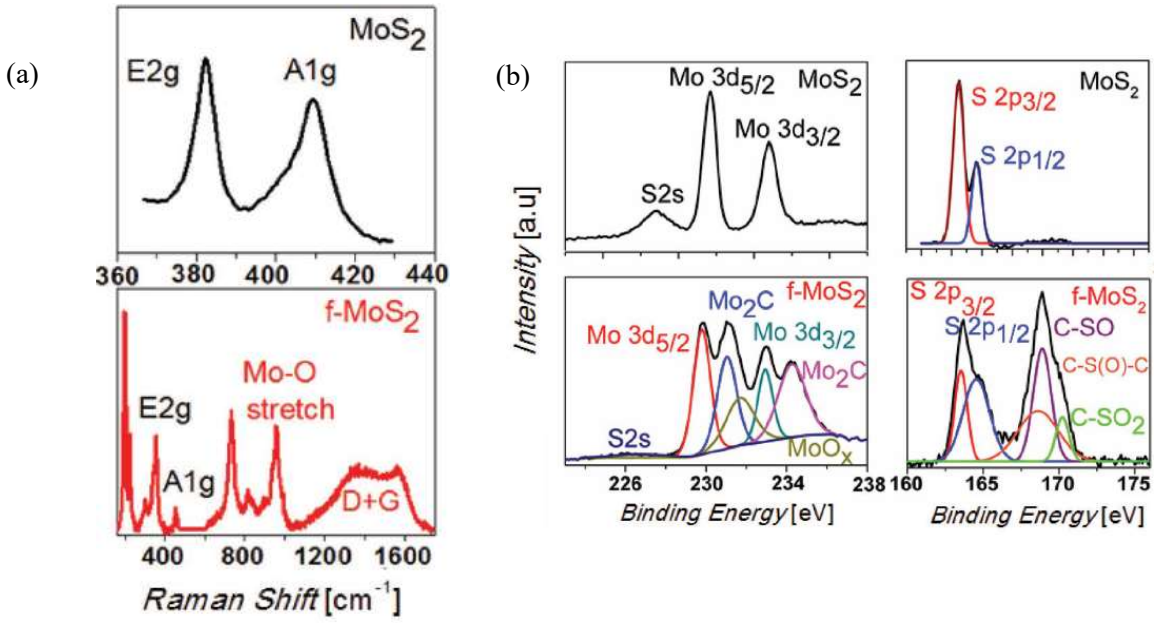

Figure 13. Characteristic and functional based (a) Raman and (b) XPS peaks of MoS_2 NPs with the upper panel being the bulk MoS_2 flakes and the lower panel being the oxygen and carbon functionalized NPs. Reprinted from (Ibrahim *et al.*, 2018) by permission from Wiley.

MoS_2 NPs have been reported to have a d-spacing of 0.23 nm, corresponding to (103) planes as shown in Figure 14(b). Zhang *et al.*, 2018 and Ibrahim *et al.*, 2018 showed that carbon functionalization of MoS_2 NPs altered the lattice spacing at the periphery of the particles. The lattice spacing in the middle of the particles was 0.27 nm, corresponding to (100) planes of MoS_2, whereas the spacing was 0.35 nm at the sides of the particle, consistent with the attachment of carbon domains as shown in Figure 14(a).

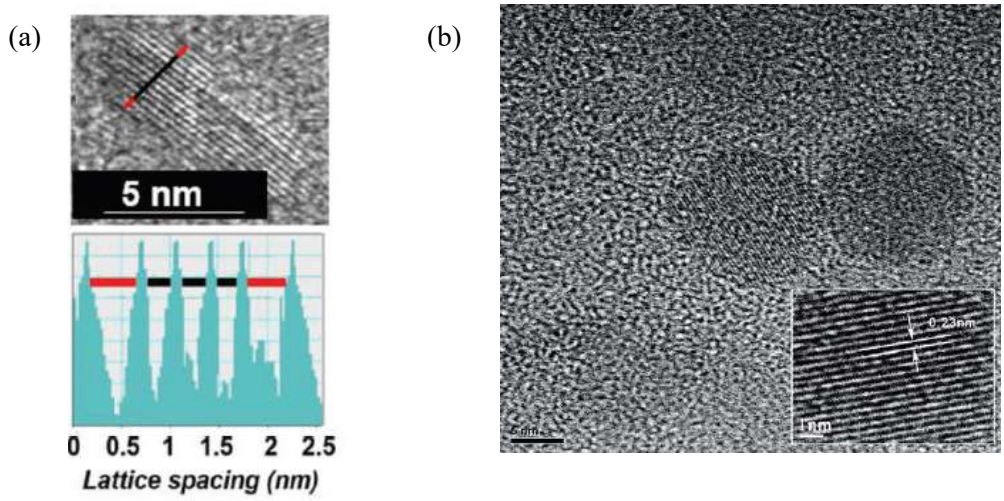

Figure 14. (a) TEM image and lattice spacing of carbon and oxygen functionalized MoS_2 NPs. Reprinted from (Ibrahim *et al.*, 2018) by permission from Wiley. (b) TEM image of MoS_2 NPs with 0.23 nm spacing of (103) planes visible. Reprinted (adapted) with permission from (Zhao *et al.*, 2017). Copyright (2017) American Chemical Society.

Black Phosphorus

BP's reactive nature and anisotropic properties allow it to be used in multiple applications. Previously reported absorption and PL spectra of BP NPs are shown in Figure 15. BP NPs are strongly absorbing in the region below 500 nm with an extended tail to 800 nm. BP NPs exhibit a strong PL peak centered around 500 nm, as demonstrated in Figure 15 (Zhang *et al.*, 2017). Nitrogen doping of BP NPs shifts the absorption peak from ~300 nm to ~340 nm and results in the emergence of three PL peaks corresponding to new electronic transitions from the lowest unoccupied molecular orbitals to orbitals below the highest occupied molecular orbitals added by nitrogen doping, as shown in Figure 16 (Ozhukil Valappil *et al.*, 2018).

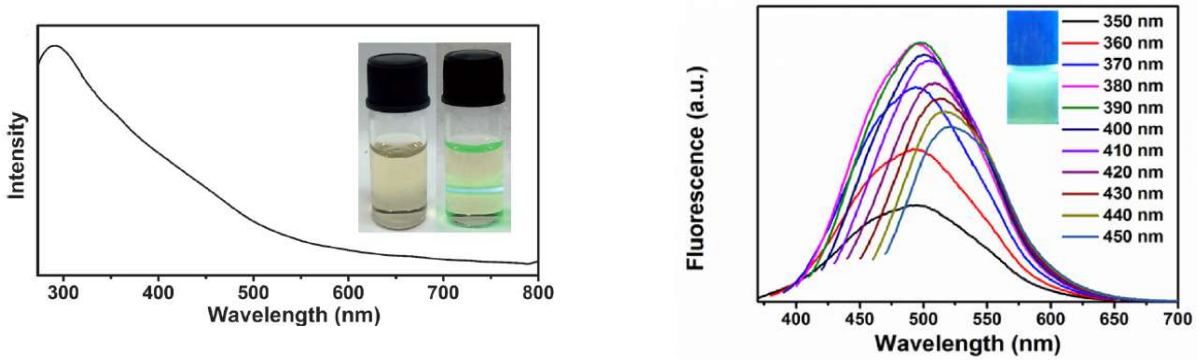

Figure 15. (a) Absorption spectrum of BP NPs. Reprinted from (Zhang *et al.*, 2017) by permission from Wiley. (b) PL spectra of BP NPs. Reprinted from Fluorescent black phosphorus quantum dots as label-free sensing probes for evaluation of acetylcholinesterase activity, Volume 250, (Gu, Yan, *et al.*, 2017), Copyright (2017), with permission from Elsevier.

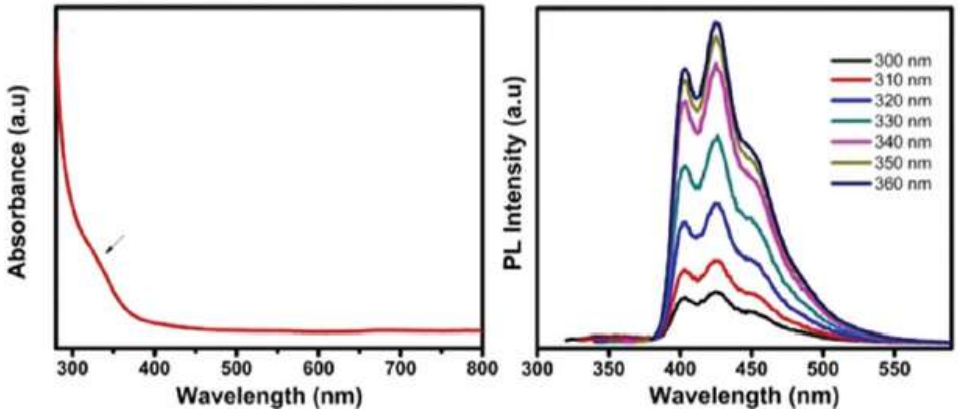

Figure 16. Absorption and PL spectra of nitrogen doped BP QDs. Reproduced from (Ozhukil Valappil *et al.*, 2018) with permission from The Royal Society of Chemistry.

The Raman spectrum of bulk BP has three main peaks at 465.19 and 437.98 cm^{-1} owing to in plane vibration modes A^2_g and B^2_g, respectively and 361.8 cm^{-1} corresponding to the out of plane phonon mode A^1_g (Ozhukil Valappil *et al.*, 2018)(Gu, Yan, *et al.*, 2017)(Zhang *et al.*, 2015). It is seen in Figure 17(a) that size reduction of bulk BP to QDs blueshifts its characteristic Raman peaks (Zhang *et al.*, 2015), whereas nitrogen doping has been reported to redshift them (Ozhukil Valappil *et al.*, 2018). The degree of size reduction and doping controls the amount of shift. It is seen in Figure 17(b) that the P 2p

XPS spectrum of BP NPs exhibit two characteristic peaks $2p_{3/2}$ and $2p_{1/2}$ of elemental P^0 and the peaks attributed to P^V correspond to the oxidation of BP QDs, proving their easy oxidation (Gu, Yan, *et al.*, 2017). Nitrogen doping of BP QDs has been confirmed in the N 1s spectrum with two peaks at 398.3 and 400.5 eV, as shown in Figure 17(c) (Ozhukil Valappil *et al.*, 2018). The TEM images of BP NPs reported by (Zhang *et al.*, 2015) show a lattice spacing of 0.34 nm for (021) planes and 0.52 nm for (020) planes of BP as shown in Figure 18.

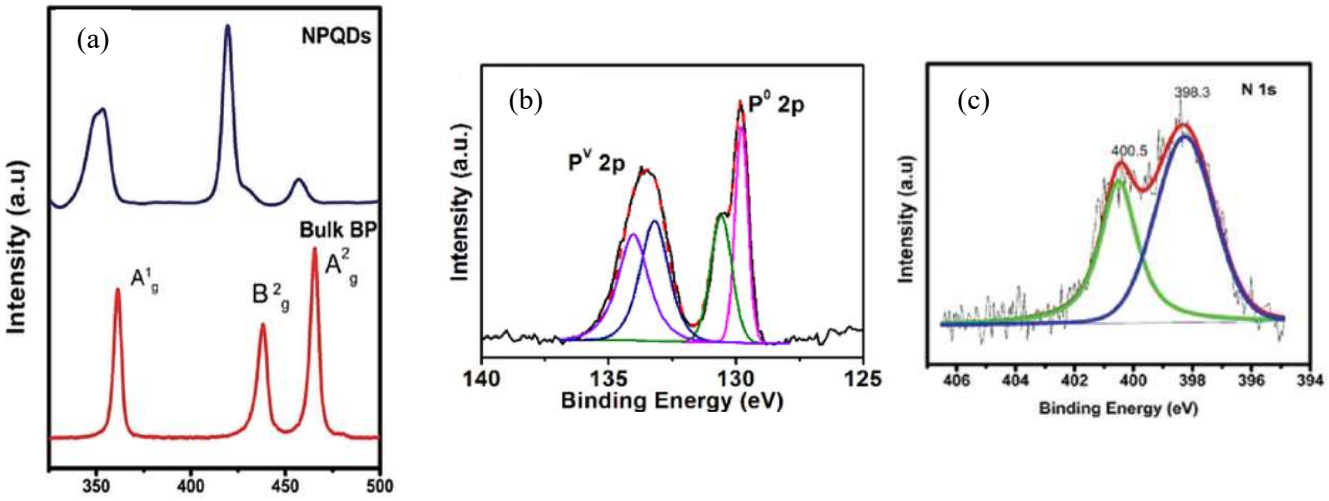

Figure 17. (a) Raman spectra of BP in bulk form and nitrogen doped NPs form. Reprinted from (Ozhukil Valappil *et al.*, 2018) by permission from Wiley Characteristic. BP XPS peaks of the spectra (b) P 2p, and (c) N 1s. Reproduced from Ref. (Gu, Yan, *et al.*, 2017) with permission from The Royal Society of Chemistry.

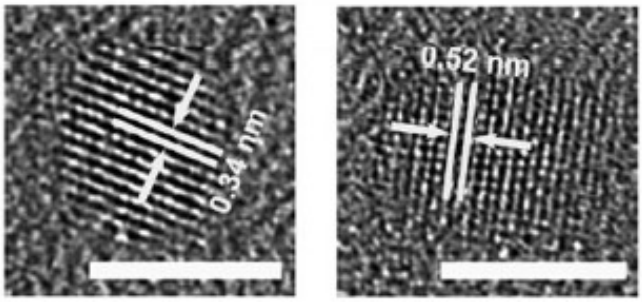

Figure 18. TEM images of BP NPs with different lattice spacings of 0.34 and 0.52 nm owing to the (021) and (020) characteristic planes of BP, respectively. Reprinted from (Zhang *et al.*, 2015) by permission from Wiley.

2.2.2 2D quantum dot synthesis techniques

The utilization of NPs and QDs in many applications engendered various synthesis techniques that produce NPs with a range of sizes and functional groups. One of the most common techniques used in QDs synthesis is the hydrothermal process (Baykal, 2014), which is a derivative of the solvothermal process. The solvothermal synthesis technique is a chemical process that takes place in a sealed container of a precursor dispersed in a solvent with high temperatures (above the boiling point) and pressure (Ouyang *et al.*, 2019). The role of elevated temperature and pressure is to change the chemical reactivity of the ingredients and enhance their solubilities and functionality (Ouyang *et al.*, 2019).

For example, Gu, Pei, *et al.*, 2017 synthesized BP NPs via the solvothermal method with N-Methyl-2-pyrrolidinone as a solvent and bulk BP as the starting material. The solution is rapidly stirred under 140 ºC for 12 hours. The QDs are then obtained by centrifuging the sample to elevate the smallest particles to the top of the solution. Wang *et al.*, 2020 also synthesized BP NPs using the solvothermal technique by dispersing bulk BP in NMP and NaOH with mild stirring at 150 ºC for 8 hours.

The long time required to fabricate NPs using the solvothermal process triggered the development of other techniques that are more time efficient. Shorie *et al.*, 2019 produced graphitic carbon nitride NPs using a microwave tube reactor at 150 ºC for 5 minutes. They obtained a residue that was washed with hexane to produce a dispersed solution of QDs. Batmunkh *et al.*, 2019 and Du *et al.*, 2020 succeeded in producing BP NPs by microwave assisted exfoliation that controls the size and morphology of the NPs depending on the temperature and time of the microwave irradiation. This process is illustrated in Figure 19.

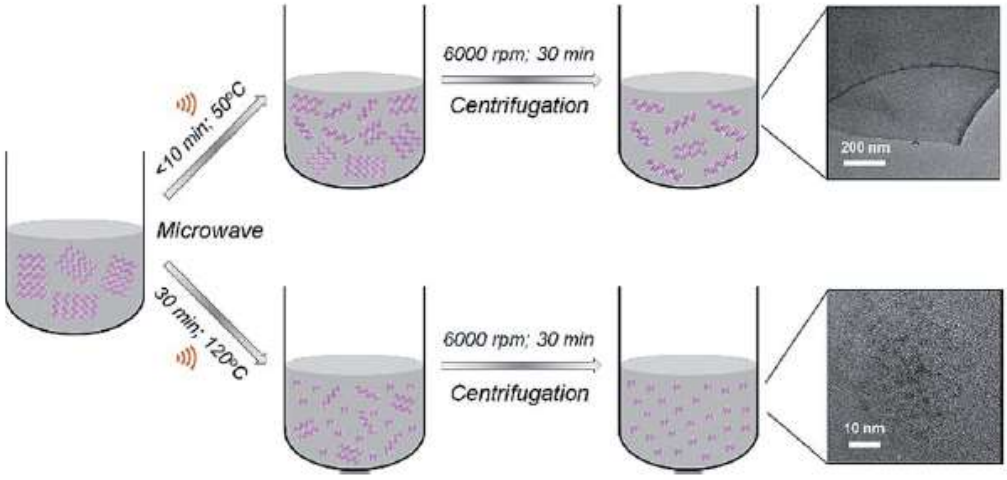

Figure 19. Microwave tube reactor synthesis of graphitic carbon nitride NPs. Reproduced from Ref. (Batmunkh *et al.*, 2019) with permission from The Royal Society of Chemistry.

Synthesis techniques that require lower operating temperatures have also been used to produce 2D QDs and NPs. Kanazawa *et al.*, 2019 produced MoS_2 NPs through laser ablation by first dissolving the MoS_2 flakes in different solvents to obtain different surface modifications, followed by stirring and ultrasonicating the solutions to reach homogeneity. The solutions were then irradiated by laser pulses (wavelength of 532 nm, 10 ns pulse width, and 55 mJ $pulse^{-1}$) for two hours. Upon laser treatment, the 2D flakes were broken down into NPs and the solution was evaporated to get rid of the solvent and to obtain MoS_2 NPs in powder form.

Our group previously synthesized MoS_2, WS_2, and BN NPs using a fs laser technique (Ibrahim *et al.*, 2018). The bulk 2D flakes were dispersed in different solvents and irradiated with the fs laser (800 nm pulses of 35 fs duration and 2 mJ of energy). The strong electric field near the focal point of the laser beam results in Coulombic explosion that dissociates the solvent molecules and the 2D flakes, as shown in Figure 20. The solutions were magnetically stirred and irradiated for 70 mins to produce 2D NPs with a lateral dimension of 3 nm. Xu *et al.*, 2019 and Nguyen *et al.*, 2019 used the same fs laser technique to synthesize MoS_2 and WS_2 NPs with different laser parameters for 30 mins followed by sonication and centrifugation to ensure the separation of the sheets and the filtration of bulk particles.

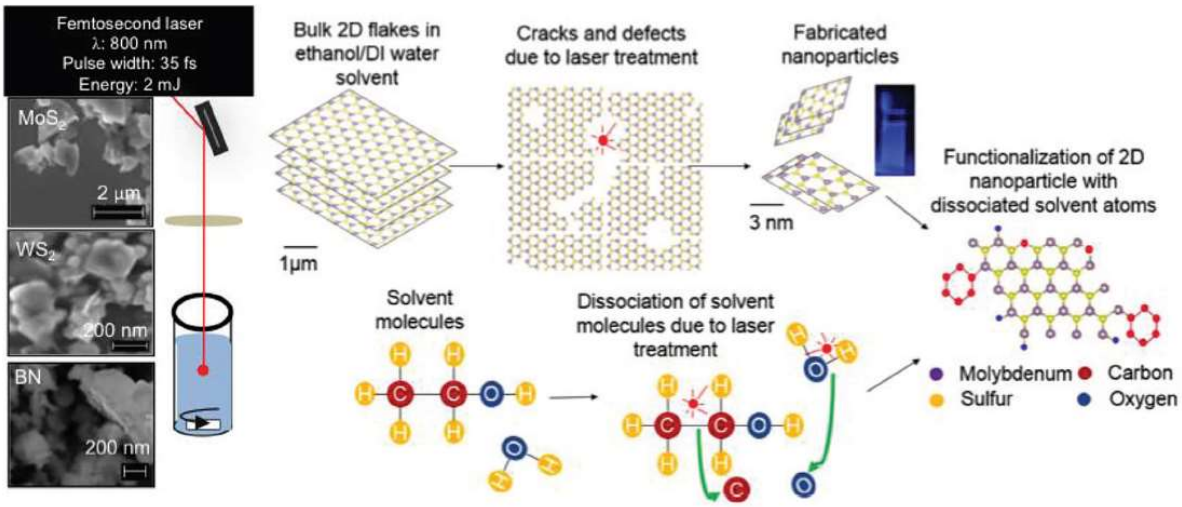

Figure 20. Fs laser exfoliation and defect creation of MoS_2 flakes dissolved in ethanol-water. Reprinted from (Ibrahim *et al.*, 2018) by permission from Wiley.

The fs laser treatment is a quick method for fabricating NPs, the properties of which can be tuned by varying the laser properties. In addition to that, dangling bonds on the laser-cleaved NP surfaces bond with dissociated solvent atoms to produce NPs with hybrid optical properties (Ibrahim *et al.*, 2018). The simultaneous fabrication and functionalization of 2D NPs by fs laser synthesis is useful for tailoring 2D NPs for various applications, including chemical sensing.

2.2.3 Heavy metal fluorescent sensing with 2D NPs

The utilization of 2D NPs as fluorescent sensors has gained a lot of attention due to the reasonable sensitivities demonstrated and the potential for on-site usage. The selectivity of the sensors towards different HMIs is the main challenge, so different fabrication techniques and precursors have been used to determine the selectivity of the sensors.

Shorie *et al.*, 2019s was able to sense Hg through quenching of the light emitted by graphitic carbon nitride NPs. The NPs were fabricated in a microwave reactor and the sensing mechanism depended on the trapping of Hg in the nitrogen defect locations in carbon. The LOD of the sensor was 250 nM and the selectivity of the sensor was not addressed. HMIs sensing can be achieved by substituting dopants attached to NPs with HMIs to change the electronic properties of the NPs. Mn-doped ZnSe NPs synthesized by a microfluidic reaction by Zhou *et al.*, 2018 were able to sense Hg selectively as shown

in the right panel of Figure 21 with a LOD of 7 nM via the substitution of Mn ions with Hg as shown in left panel of Figure 21.

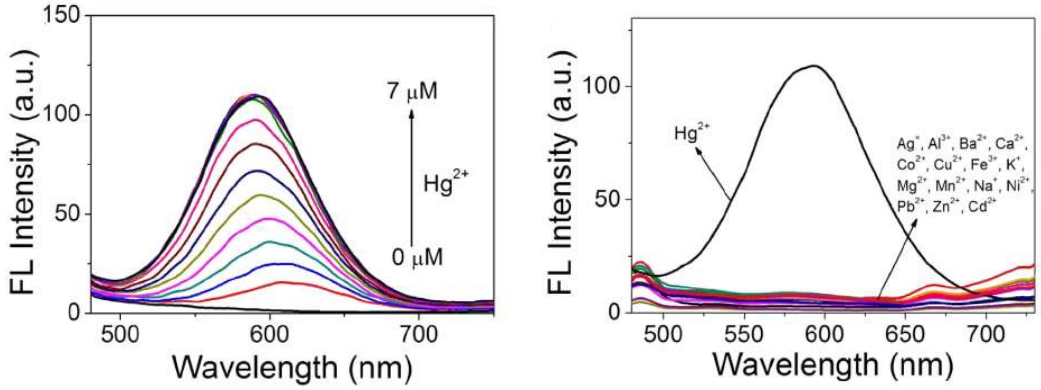

Figure 21. Fluorescence turn-on selective sensing of Hg using Mn-doped ZnSe QDs. Reprinted from Highly selective and sensitive detection of Hg2+ based on fluorescence enhancement of Mn-doped ZnSe QDs by Hg^{2+}-Mn^{2+} replacement, 254, (Zhou *et al.*, 2018), 8-15, Copyright (2018), with permission from Elsevier.

Kumar *et al.*, 2017 and Radhakrishnan and Panneerselvam, 2018 were able to synthesize carbon QDs to sense Pb with a LOD of 0.59 nM and As with a LOD of 2.3 nM. The carbon QD sensors showed high sensitivity and selectivity to Pb and As based on the interaction of oxygen functional groups with the HMIs (Radhakrishnan and Panneerselvam, 2018). The oxygen functional groups on the surface of the carbon dots enhanced the formation of As-O passivation on the surface. The fluorescence of the carbon dots decreased, and this can be attributed to electronic transfer between the oxygen and As ions. Similarly, Pb detection was reported by Kumar *et al.*, 2017 with high selectivity and sensitivity achieved using amine-functionalized carbon dots. The vacant Pb d-orbitals interacted with the amine groups attached to the surface of the carbon dots, changing the surface charge of the dots and turning off their fluorescence (Kumar *et al.*, 2017).

Other 2D materials like BP were also utilized in fluorescent sensors to detect HMIs. Gu, Pei, *et al.*, 2017 synthesized BP QDs solvothermally to detect Hg selectively with a LOD of 0.39 nM. The sensing mechanism depended on the overlap between Mn-doped BP QDs excitation spectrum and tetraphenylporphyrin tetrasulfonic acid (TPPS) absorption spectrum. Hg acts as a bridge to enhance the binding between TPPS and Mn^{2+} ions, which decreased the absorption of the whole complex formed, as shown in Figure 22. This absorption decrease was proportional to the concentration of added Hg ions

and this resulted in a gradual fluorescence decrease upon increasing the concentration of Hg, as shown in Figure 22.

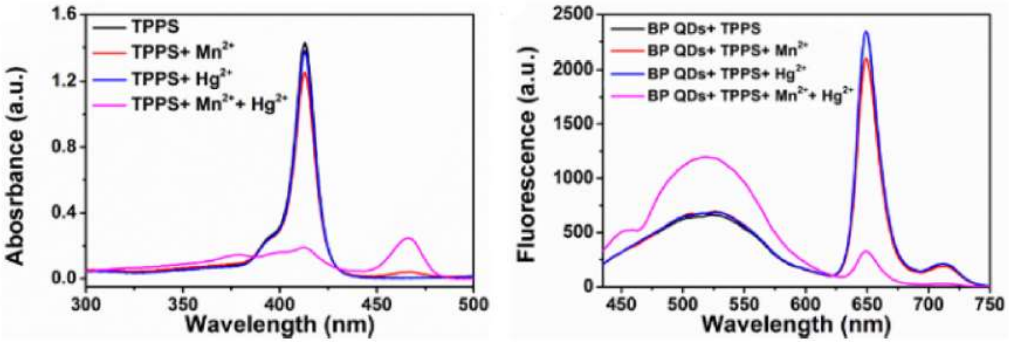

Figure 22. Hg sensing using functionalized BP QDs. Reprinted (adapted) with permission from (Gu, Pei, *et al.*, 2017). Copyright (2017) American Chemical Society.

Lin *et al.*, 2019 was able to functionalize MoS_2 NPs with different functional groups to selectively detect Co, Cd, and Pb ions. COOH, NH_2, and SH functional groups were attached to the surface of the NPs during the hydrothermal synthesis. MoS_2/COOH, MoS_2/NH_2, and MoS_2/SH QDs detected Co^{2+}, Cd, and Pb, respectively. The LOD of Co^{2+}, Cd, and Pb were found to be 54.5, 99.6, and 0.84 nM, respectively. Unfunctionalized MoS_2 NPs are highly fluorescent due to the radiative recombination of electron hole pairs. However, functionalizing MoS_2 NPs enhances the bonding of functional groups with S vacancy sites, decreasing excess free electrons that in turn decreases the electron hole radiative recombination rate. The addition of the HMIs to the solutions containing the functionalized MoS_2 NPs restored the fluorescence of the NPs. The functional groups on the surface of MoS_2 NPs decrease the luminescence of the NPs by capping the sulfur vacancy sites, decreasing the number of excess carriers in the conduction band of the NPs. Upon the addition of HMIs, the metal ions d-orbital electrons repel the capping functional groups, increasing the number of free carriers in the conduction band and turning on the fluorescence of the functionalized NPs. The ability to functionalize the same material (MoS_2) with COOH (Figure 23(a)), NH_2 (Figure 23(b)), and SH (Figure 23(c)) allowed selective sensing of Co^{2+}, Cd^{2+}, and Pb^{2+}, respectively.

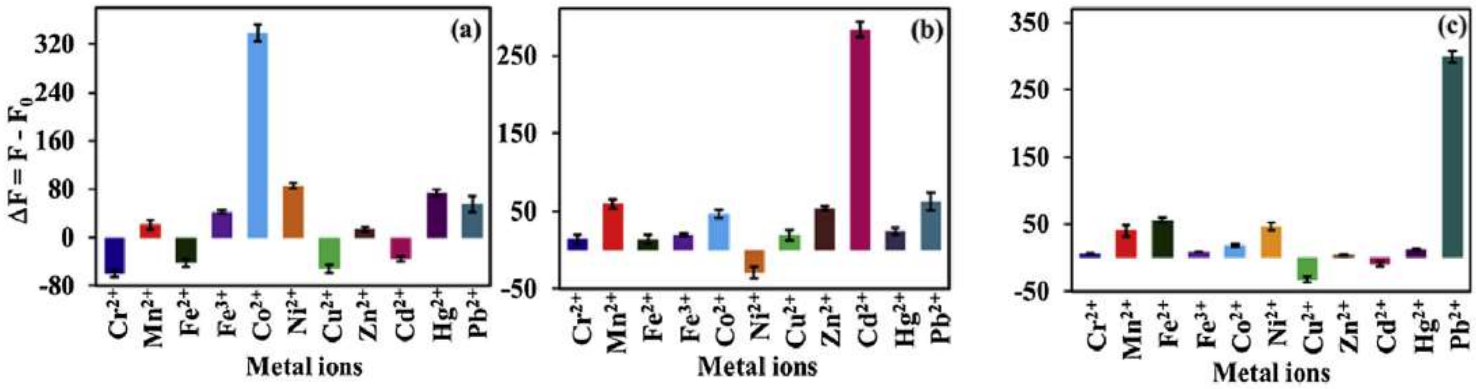

Figure 23. Selective ions sensing using surface functionalized MoS_2 NPs with (a) COOH, (b) NH_2, and (c) SH. Reprinted from Fluorescence turn-on chemosensors based on surface-functionalized MoS_2 quantum dots, 281, (Lin *et al.*, 2019), 659-669, Copyright (2019), with permission from Elsevier.

2.3 Summary

This chapter demonstrated the prominent properties of BP, GO, and MoS_2 NPs. The optical characterization of BP, GO, and MoS_2 NPs demonstrated strong absorption and PL characteristics. Their chemical properties can be tuned via size reduction and the addition of functional groups as confirmed by Raman and XPS analysis of bulk and functionalized NPs. TEM analysis of synthesized 2D NPs showed different lattice spacings owing to the defective and reactive nature of the NPs due to the addition of various functional groups, enabling 2D NPs to be used in HMIs sensing. Different NPs synthesis techniques were discussed, where various properties can be tuned through the addition of different functional groups. 2D NPs' strong absorption, PL, and flexible surface modification have made them strong candidates for sensitive and selective HMIs fluorescence sensors.

Using 2D QDs and NPs as fluorescent sensors allows sensitive on-site HMIs detection. TMDs, GO, and BP can be designed to sense several HMIs based on the synthesis method and precursors used. The main challenge is the selectivity of those NPs towards different HMIs. A thorough study of the affinity of the HMIs to various functional groups is required to sense them selectively with high sensitivity. A quick fs laser technique capable of synthesizing NPs and functionalizing them with solvent-based atoms

will be discussed in the next chapter. Defects created by the fs laser allow a high degree of functionalization and create active chemical sites for HMIs detection.

Chapter 3
Experimental Methods

3.1 Materials

MoS_2 powder and NGO flakes were purchased from Graphene Supermarket and BP powder was purchased from Ossila. Acetonitrile ReagentPlus 99% was purchased from Sigma Aldrich. Lead, mercury, cadmium (0.1 mg/mL), and arsenic (0.01 mg/mL) metal trace standard solutions were dissolved in nitric acid complex with concentrations of 0.5%, 7%, 3%, and 2% v/v, respectively. These were purchased from Inorganic Ventures.

3.2 Solution preparation

200 mg of 2D bulk flakes of BP, NGO, and MoS_2 were dispersed in 20 mL of acetonitrile or ethanol-water (except for BP not being treated in ethanol-water for degradation issues mentioned earlier) to form 1 mg/mL stock solutions. Solutions were sonicated for 10 mins to prevent agglomerations and confirm solution homogeneity. 4 mL of stock solutions and subsequent dilutions of 0.01 and 0.1 mg/mL were poured into separate vials containing magnetic stirrers.

3.3 Femtosecond laser treatment

A fs laser is an ultrafast laser whose pulse has a duration on the order of fs. The time delay of the pulses ranges from 0 to 10 ps (Li *et al.*, 2017). A fs laser can be used as a tool to alter the properties of a material or reduce its size (Gattass and Mazur, 2008). Laser treatment can exfoliate bulk 2D materials into smaller-sized sheets if the fluence of the laser is higher than the ablation threshold of the bulk material (Li *et al.*, 2017). The laser's strong electric field can repel the electrons responsible for holding the 2D sheets in stacks. This leads to Coulombic explosion due to the repulsion of the atomic charges and causes exfoliation of the 2D stacks (Ibrahim *et al.*, 2018). Further material size reduction is possible at longer irradiation times where the high electric field near the energetic laser focal point breaks the 2D material into smaller particles (Ibrahim *et al.*, 2018). The fs laser is also capable of dissociating solvent molecules, producing free radicals that can bond with surface dangling bonds formed on 2D materials by the laser treatment (Ibrahim *et al.*, 2018). Accordingly, a clean and quick method of NPs or QD solution synthesis is through fs laser treatment of the 2D multilayer materials with the added

benefit of being able to functionalize the materials with desired functional groups through appropriate selection of solvents. In this work, a Ti:Sapphire oscillator is used in all laser treatment processes. The tunability and broad emission bandwidth of the Ti:Sapphire oscillator allow it to generate ultrafast pulses in the range of fs. A Spitfire Ace-35F chirped pulse amplification system adds energy to the generated pulses without changing the pulse duration, producing a laser beam with the specifications shown in Table 2.

Table 2. Fs laser specifications used in this work's NPs synthesis.

Wavelength	800 nm
Pulse Duration	35 fs
Beam Waist	1 cm
Energy	2 mJ
Repetition Rate	1 kHz

The solutions were exposed to a 2 W laser beam for up to 100 mins. The fs laser was focused using a 5 cm convex lens where the focal point is 1 cm below the solvent level. The solutions were stirred at 200 rpm during the treatment process as shown in the schematic in Figure 24 and the real setup in Figure 25. The treatment times for BP, NGO, and MoS_2 treated in ethanol-water and acetonitrile are shown in Table 3.

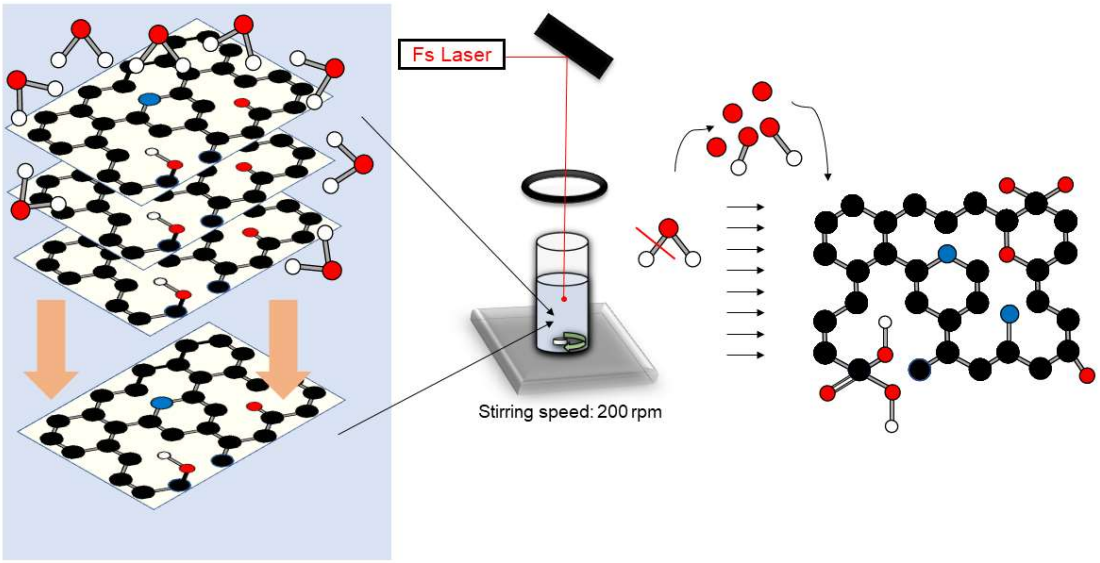

Figure 24. Fs laser treatment of 2D stacks of NGO in ethanol-water mixture stirred at 200 rpm. Dissociated water molecules bonded with chemically active NGO NPs to tune the properties of the NPs.

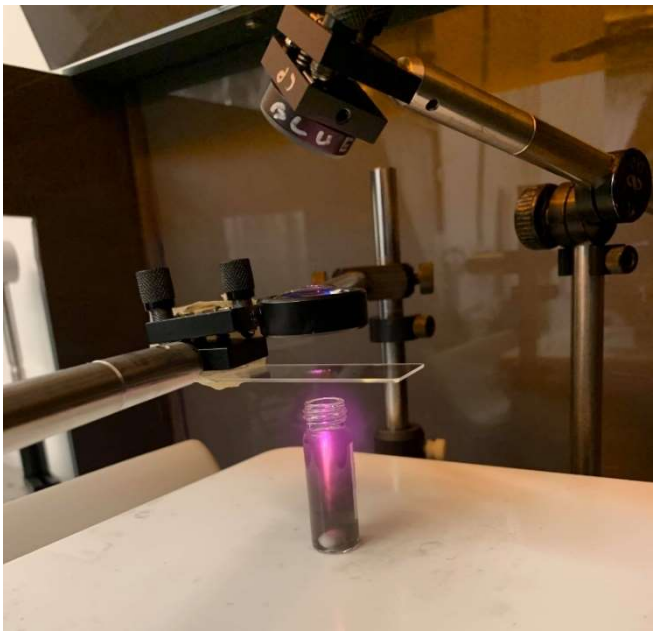

Figure 25. Fs laser treatment setup with MoS_2 flakes dissolved in acetonitrile.

Table 3. Materials and laser treatment time used in this work.

Material	Solvent	Treatment time
NGO	1:1 ethanol-water	100 mins
NGO	Acetonitrile	70 mins
BP	Acetonitrile	70 mins
MoS_2	1:1 ethanol-water	70 mins
MoS_2	Acetonitrile	70 mins

3.4 Nanoparticle Characterization

The NPs solutions were first filtered using a 0.22 μm filter to remove any untreated agglomerations for all characterization tests. A Horiba QuantaMaster 8000 was used to obtain the absorption spectra, PL spectra, PLQY (using a Horiba K sphere discussed next), and PL lifetime decay of the NP solutions. A 350 nm NanoLED was used to excite the NPs solutions for PL lifetime decay measurements. The instrument response function (IRF) of the PL lifetime decay measurements was measured using colloidal silica. For Raman and XPS, untreated solutions and 100 μL of the filtered treated solutions were drop casted on diced and cleaned silicon substrates. A window and two glass slides were used for FTIR sample preparation, where 100 μL of NPs solutions with and without added HMIs were drop casted on one glass slide and the other slide was placed on top of the solution-containing-slide. The two slides were placed in the FTIR window inserted in the SHIMADZU FTIR-8400S spectrometer that was used to obtain the FTIR spectra. A Renishaw micro Raman was used to obtain the Raman spectra of the solutions using a wavelength of 632.8 nm and a power of 20 mW. XPS measurements were performed using a Thermo-VG Scientific ESCALab 250 microprobe and a 1486.6 eV monochromatic Aluminum Kα source. For TEM characterization, NPs solutions were drop casted on lacey carbon grids and filter paper was placed beneath the grid to absorb the solvent and leave only the NPs on the TEM grid. The TEM images were collected using a Zeiss Libra 200 MC operating at 200 kV.

The PLQY is defined as the ratio of the number of photons emitted to the number of photons absorbed by the sample:

$$\text{PLQY} = \frac{\#\ \text{photons emitted}}{\#\ \text{photons absorbed}}$$

The integrating sphere measurements determined the PLQY through the attenuation of the excitation intensity of the beam exciting the sample. Horiba K-sphere (an integrating sphere) was attached to the QuantaMaster 8000 spectrometer entry. The interior part of the integrating sphere is coated with a >99% reflecting material (usually Teflon) to ensure total collection of emitted photons (Porrès *et al.*, 2006). To calculate the number of photons emitted and absorbed, scans of 1. the emission from the sample and 2. the emission across the excitation beam are obtained. Similar measurements are also performed for a blank sample (reference). The measured spectra are integrated (area under the peaks determined) and the PLQY is calculated as:

$$\text{PLQY} = \frac{\text{I}_{\text{em}}(\lambda) - \text{I}_{\text{ref2}}(\lambda)}{\text{I}_{\text{ex}}(\lambda) - \text{I}_{\text{ref1}}(\lambda)} \quad (1)$$

$I_{em}(\lambda)$: Corrected sample emission (PL)

$I_{ref2}(\lambda)$: Corrected blank emission (PL)

$I_{ex}(\lambda)$: Corrected sample emission across excitation (excitation beam)

$I_{ref1}(\lambda)$: Corrected blank emission across excitation (excitation beam)

The blank reference used in all measurements was a quartz cuvette since the NPs and the solvent are laser treated forming a hybrid material and using the original solvent doesn't represent a suitable reference. The sphere emission measurements didn't match the steady-state PL measurements because treated NPs are strongly absorbing, causing reabsorption and re-emission effects. The PLQY values were calculated using the spectrometer software FelixGx that has an integrated math tool that integrates the spectra and finds the PLQY values using equation (1).

3.5 Heavy metal Sensing

The laser treated and functionalized NPs are expected to detect the toxic ions based on the high affinity of the functional groups to the HMIs. HMIs detection was studied by examining the 2D NP PL spectrum before and after adding the toxic metal standard solutions with different concentrations diluted with water and nitric acid. The PL spectra of blank NP solutions were recorded several times to account for the sensitivity of the spectrometer and to calculate the LOD. The LOD is calculated by the 3σ/K method, where σ is the standard deviation (S.D.) of 8 blank measurements as demonstrated in

Figure A-1 and K is the slope of the calibration curve in the linear region (Radhakrishnan and Panneerselvam, 2018), which was obtained as follows: 4 μL of the HMIs standard solution of increasing concentration was added to 1.5 mL of filtered NP solution and the solution was left for 15 minutes. The standard solution with a concentration of 0.1 μM was added first, followed by higher concentrations, and the PL spectrum was measured after every addition. A calibration curve between the HMI concentration and the fluorescence intensity change was then plotted to determine the sensitivity and selectivity of the device. The ratio of the maximum quenched fluorescence intensity to the blank NPs fluorescence intensity is called the quenching factor and it is calculated as $1 - F/F_0$, where F_0 is the fluorescence intensity of the NPs and F is the fluorescence intensity of the saturated quenching curve due to the addition of HMIs.

Chapter 4
Results

4.1 Characterization

4.1.1 Screening of two-dimensional nanoparticle solution sensors

BP characterization was not successful, which was attributed to the oxygen functional groups attached to the NPs' periphery causing material degradation. MoS_2 treated in ethanol-water did not demonstrate any linear fluorescence quenching upon adding any of the HMIs to the NPs solution. Accordingly, the sensing NPs solutions used were NGO treated in acetonitrile and ethanol-water and MoS_2 treated in acetonitrile. The optimal concentration of NPs was found to be 0.1 mg/mL (compared to 1 mg/mL or 0.01 mg/mL) based on the sensing linearity and quenching factor. The following sections will focus on the characterization results of 0.1 mg/mL MoS_2 treated in acetonitrile and NGO treated in ethanol-water and acetonitrile for their superior sensing results over those of the other NPs/solvent combinations.

4.1.2 Absorption Spectroscopy

MoS_2

In general, nitrogen doping broadens the absorption spectrum of the host material to the visible region (Liu *et al.*, 2016), and that can be seen in the absorption spectrum in Figure 26(a). The absorption spectrum of MoS_2 NPs laser treated in acetonitrile is wider and multiple peaks in the range of 300 – 400 nm are observed, where the main peak is situated at 400 nm. The bandgap value of MoS_2 in acetonitrile is determined to be 2.7 eV in Figure 26(b).

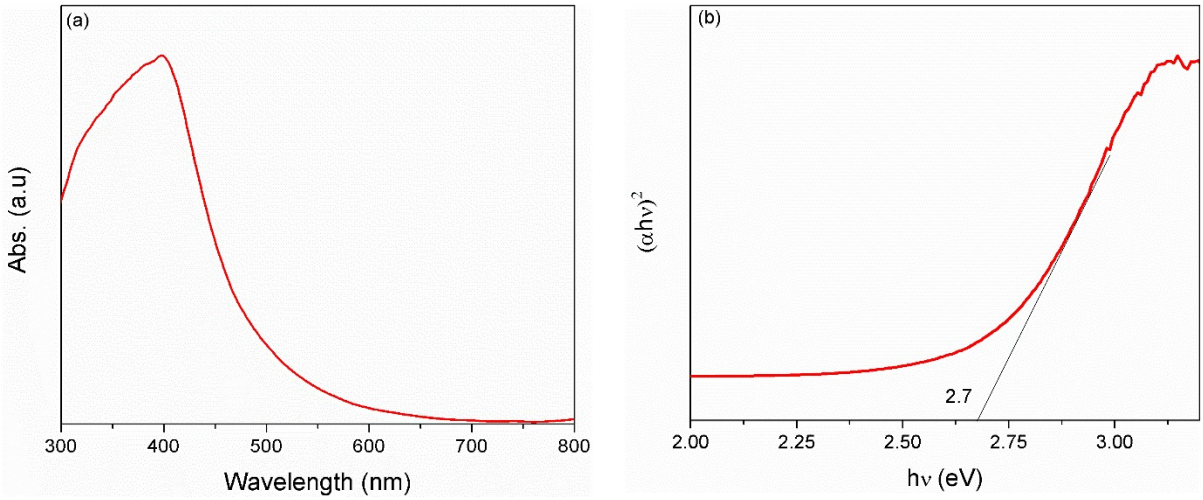

Figure 26. MoS_2 NPs in acetonitrile (a) absorption spectrum and, (b) Tauc plot and bandgap calculation.

NGO

The different solvents used in the laser treatment process are expected to produce materials with hybrid optical properties based on the 2D NPs and the functional groups attached to their surfaces. The hybrid optical properties can be seen in the differences in the absorption spectra of a certain 2D material laser treated in different solvents. NGO NPs synthesized in ethanol-water have an absorption spectrum with a shoulder at 257 nm that can be attributed to the $\pi \rightarrow \pi^*$ transition of the C=C bond and a dominant peak at 294 nm that can be attributed to the $n \rightarrow \pi^*$ transition of C – O – C as seen in Figure 27(a) (Ben Aoun, 2020). The Tauc plot in Figure 27(b) demonstrates a bandgap value of 3.6 eV.

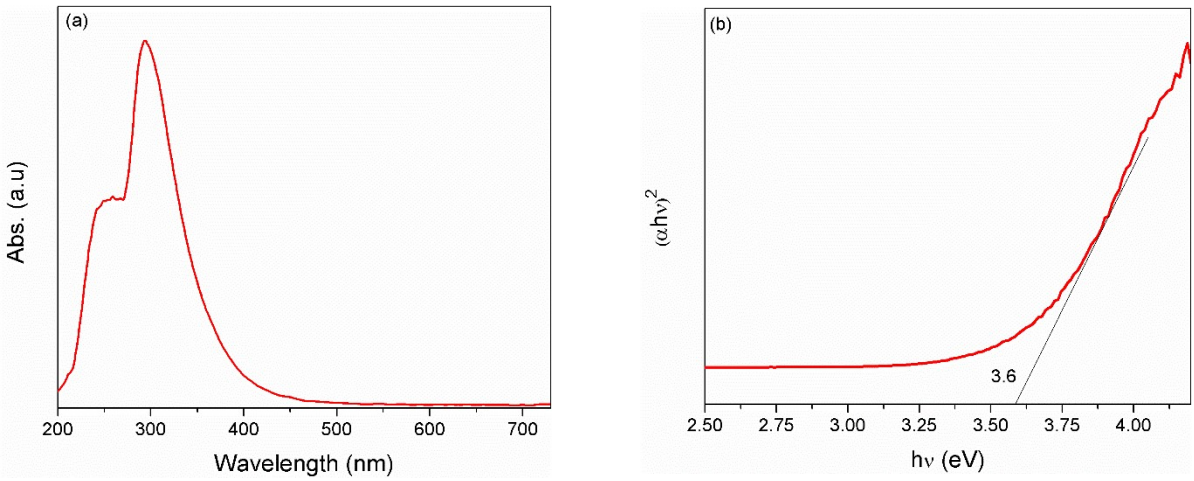

Figure 27. NGO NPs in ethanol-water (a) absorption spectrum and, (b) Tauc plot and bandgap calculation.

The NGO NPs functionalized by acetonitrile possess different absorption properties (Figure 28) that are more similar to those of MoS_2 treated in acetonitrile, which emphasizes the strength of the solvent-induced effects. Graphene based NPs are expected to have multiple peaks in the range of 200 – 400 nm as reported by (Yeh *et al.*, 2014). The main shoulders shown in Figure 28(a) are situated at 256, 292, 320, and 370 nm and they can be attributed to $\pi/n \rightarrow \pi^*$, C=C and C=O, C=N $\pi \rightarrow \pi^*$, and $n \rightarrow \pi^*$ transitions (Yeh *et al.*, 2014). The dominant peak at 413 nm and the broadening of the absorption spectrum in Figure 28(a) is attributed to amine groups formed on the surface of the NGO NPs (Mokhtar Mohamed *et al.*, 2018). The Tauc plot in Figure 28(b) shows that NGO treated in acetonitrile has a bandgap of 2.53 eV, which is lower than that of NGO treated in ethanol-water owing to the presence of oxygen functional groups (originating from water) (Acik and Chabal, 2012).

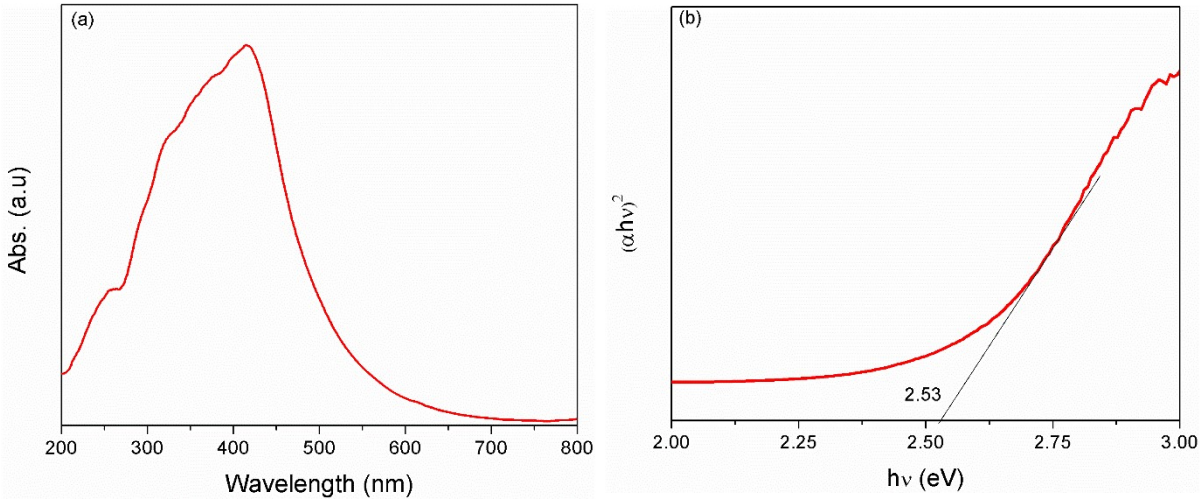

Figure 28. NGO NPs in acetonitrile (a) absorption spectrum and, (b) Tauc plot and bandgap calculation.

4.1.3 Photoluminescence Spectroscopy

The solvent-mediated functionalization of the 2D NPs is similarly evident from the differences in the PL spectra of the materials laser treated in different solvents. The PL spectrum of MoS_2 NPs functionalized by acetonitrile possess a main peak situated at 387 nm and a shoulder that can be seen in Figure 29(a) at 466 – 523 nm, which is attributable to surface state emission luminescence due to nitrogen functionalization (Wu *et al.*, 2020). The PL spectrum of NGO treated in ethanol-water and excited at 320 nm in Figure 29(b) has a major peak at 388 nm with a long tail extended to the blue emission, resembling aromatic cores and mid gap electron transitions in agreement with the GO QDs produced by (Shokry *et al.*, 2019). On the other hand, NGO laser treated in acetonitrile was excited at 360 nm in Figure 29(c) and it possesses a single bell-shaped dominant peak situated at 507 nm resembling $\pi \rightarrow \pi^*$ and $n \rightarrow \pi^*$ transitions (Novoa-De León *et al.*, 2019). The different PL spectra correspond to the different absorption spectra of NGO treated in different solvents, as shown in Figure 27(a) and Figure 28(a).

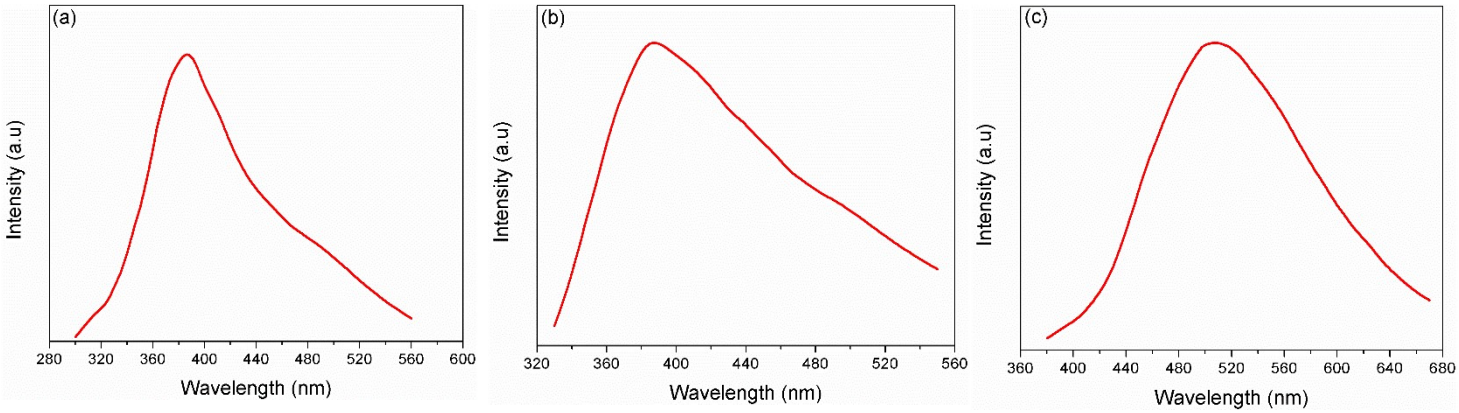

Figure 29. Photoluminescence spectra of laser treated (a) MoS_2 in acetonitrile, (b) NGO in ethanol and water, and (c) NGO in acetonitrile.

4.1.4 Photoluminescence Quantum Yield

The spectra measured for PLQY calculations of MoS_2 NPs in acetonitrile are shown in Figure 30(a)-(b). The excitation beam is shown in Figure 30(a) with and without the MoS_2 NPs in acetonitrile and the emission scan of the MoS_2 NPs in acetonitrile is shown in Figure 30(b). The excitation and emission scans for the NGO laser treated in ethanol-water and acetonitrile are similarly shown in Figure 31 (a)-(b) and (c)-(d), respectively. The calculated PLQY values are summarized in Table 4.

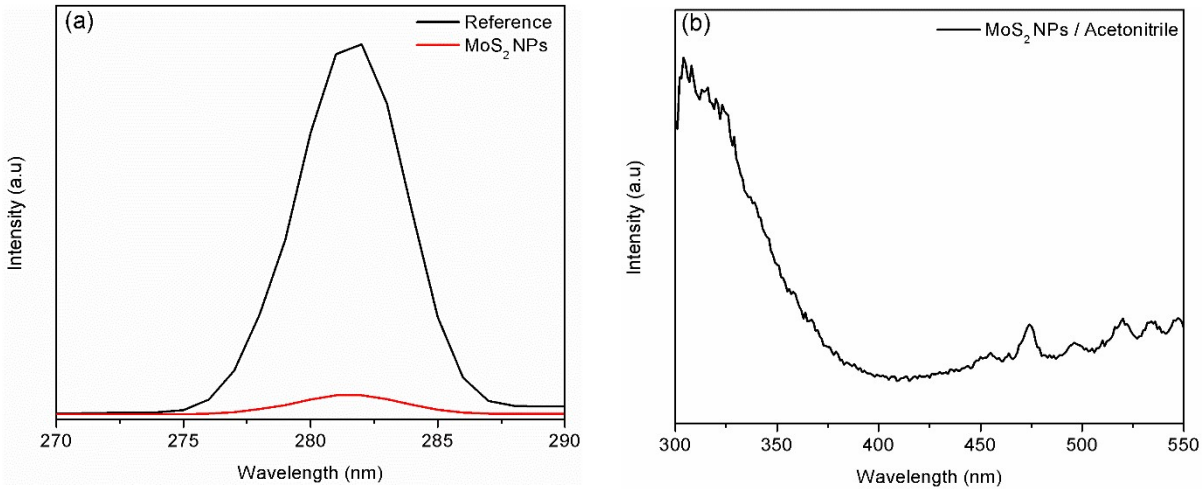

Figure 30. MoS_2 NPs in acetonitrile (a) emission across the excitation and (b) emission scan.

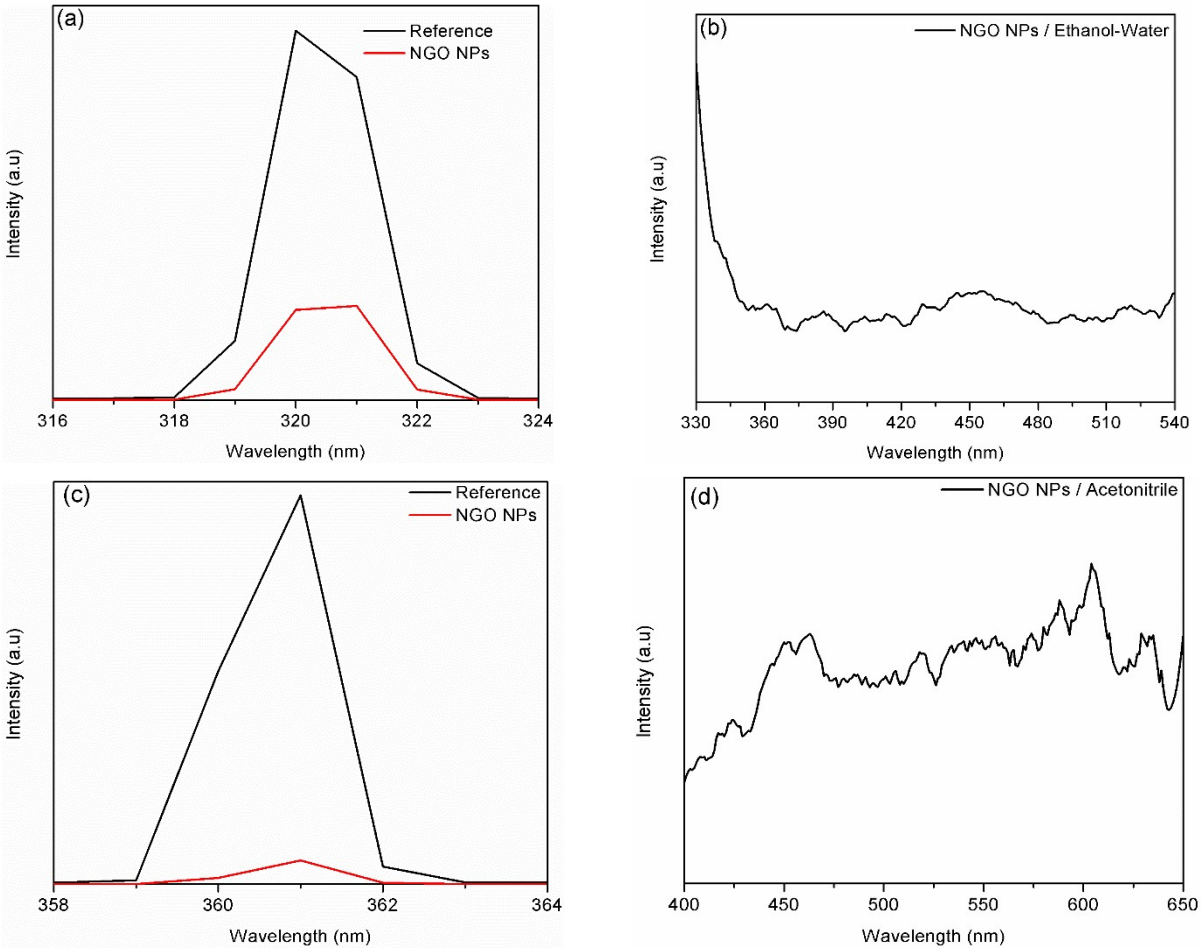

Figure 31. Emission across the excitation in the left panel and emission scans in the right panel of (a) NGO NPs in ethanol-water mixture and (b) NGO NPs in acetonitrile.

Table 4. PLQY values of MoS_2 and NGO NPs in ethanol-water mixture and acetonitrile.

Material	Solvent	PLQY
MoS_2	Acetonitrile	2.4%
NGO	Ethanol-Water	1.2%
NGO	Acetonitrile	1.7%

4.1.5 Raman Spectroscopy

The functionalization of the 2D NPs was confirmed using Raman Spectroscopy by comparing the bulk untreated solutions and laser-treated NP solutions of NGO and MoS_2 in the ethanol-water mixture and acetonitrile. The laser treated NPs displayed similar characteristics as their bulk counterparts in addition to new vibrational modes, altered intensities, and peak shifts.

Laser treated MoS_2 in acetonitrile showed the same Raman characteristics of the bulk MoS_2 flakes with the in-plane and out-of-plane vibrations owing to the characteristic E^2_g (375.6 cm^{-1}) and A^1_g (402.5 cm^{-1}) peaks respectively. However, the Raman spectrum of MoS_2 NPs showed a slight blueshift of the vibrational modes as shown in Figure 32(a), which are attributed to an increased electron density near the chemically active regions of the NPs owing to doping by the nitrogen functional groups and increased sulfur vacancies. An extended Raman spectrum of the MoS_2 NPs treated in acetonitrile was measured, as shown in Figure 32(b), and the laser-treated NPs solution was found to possess characteristic D and G bands owing to the carbon functionalization (Ibrahim *et al.*, 2018).

The Raman spectrum of NGO in ethanol-water before laser treatment and size reduction is shown in Figure 32(c). Clear characteristic peaks are seen at 1330, 1557, and 1614 cm^{-1} owing to the D band (sp^2), G band (sp^3), and D$^{'}$ bands respectively (Novoa-De León *et al.*, 2019)(Wu *et al.*, 2018). The laser treated NGO in ethanol-water (also shown in Figure 32(c)) is expected to be reduced in size and to have increased carbon and oxygen functional groups owing to the dissociated solvent molecules attached to the surface of the NGO. The G and D$^{'}$ peaks of the treated solution were split due to the increased carbon defectiveness and size reduction of the bulk NGO flakes into NPs, which confirms the disruption in the graphitic domains due to the stress added in the graphitic planes by the addition of functional groups (Stankovich *et al.*, 2007). The effect of the water was tangible in the rise of the 1450 cm^{-1} peak in the treated solution that can be attributed to the stretching of the hydroxyl groups attached to the carbon domains of NGO (Wang *et al.*, 2011). The Raman spectrum of NGO in acetonitrile possessed different properties, as seen in Figure 32(d), where the characteristic D and G peaks were broadened till they merged, which shows the high level of defectiveness in the NGO NPs owing to the expected addition of carbon, nitrogen, hydrogen, and oxygen functional groups (Bartolucci *et al.*, 2011).

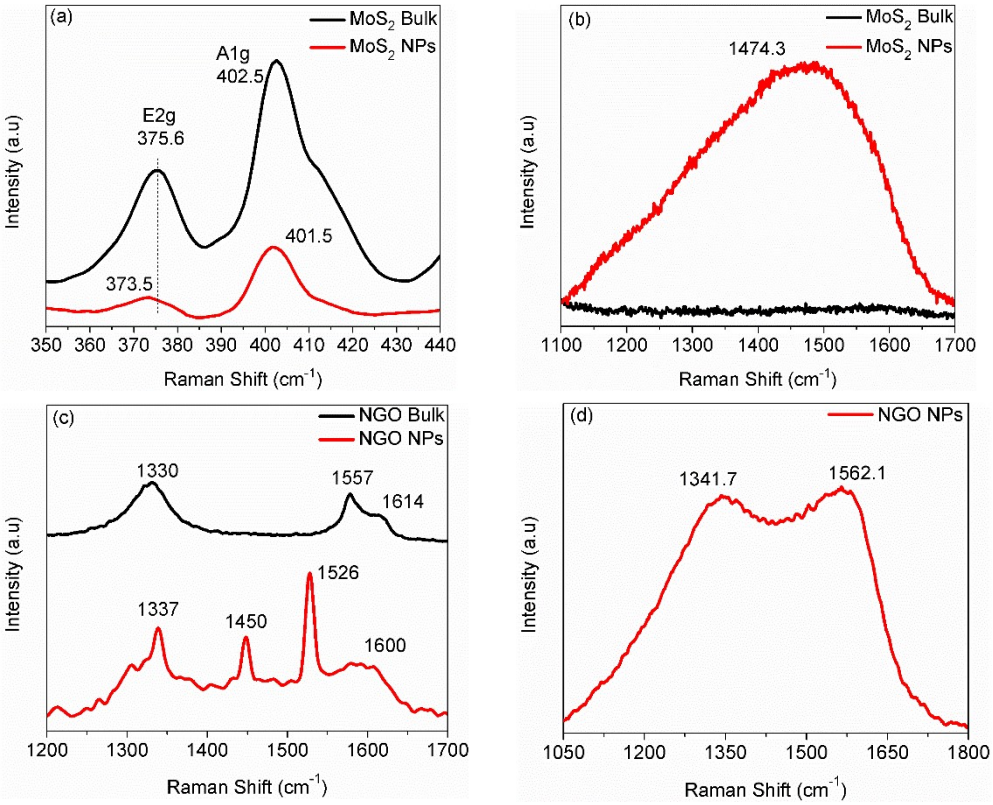

Figure 32. Raman spectra of (a)-(b) MoS_2 NPs in acetonitrile, (c) untreated NGO flakes and NGO NPs in ethanol and water, and (d) NGO NPs in acetonitrile.

4.1.6 Xray Photoelectron Spectroscopy

XPS was performed to confirm the presence of the functional groups attached to the NPs and to investigate the bonds responsible for chemical sensing. The C 1s spectrum of NGO treated in acetonitrile is shown in Figure 33(a). It showed distinctive peaks at 284.3, 285, 286, 287.2, and 287.7 eV, which are attributed to C – C, C=O, C – N /C – OH, C=C, and O – C=O bonds, respectively (Yeh *et al.*, 2014)(Das *et al.*, 2012). The presence of the C – N peak is consistent with the Raman spectroscopy results. The N 1s spectrum in Figure 33(b) showed the three different carbon-nitrogen configurations discussed in Section 2.2.1. The pyrrolic nitrogen is the most intense peak, implying that the surface of the NPs is highly reactive due to the presence of unsatisfied bonds.

The C 1s XPS spectrum of NGO treated in the ethanol-water in Figure 33(c) showed slightly different features when compared to that of NGO treated in acetonitrile. Peaks were observed at 284.4, 285.1, 286, 286.7, and 288.9 owing to C – C, C=C, C – N/C – O, C – OH, and COOH bonds (Wang *et al.*,

2014)(Rabchinskii *et al.*, 2020)(Das *et al.*, 2012). The O 1s spectrum of NGO in ethanol-water in Figure 34(d) showed two distinctive characteristic peaks at 531.8 and 533.4 eV resembling the oxygen functionalization attributed to C – O and C=O/C – OH, respectively (Rakibuddin and Kim, 2019). The compositions (determined from the XPS data) of the NGO NPs laser-treated in acetonitrile and ethanol-water are summarized in Tables 5 and 6, respectively. The compositions are consistent with significant nitrogen functionalization by the acetonitrile solvent and significant incorporation of hydroxyl groups by the ethanol-water. The dominance of oxygen functional groups in NGO treated in ethanol-water and that of nitrogen in NGO treated in acetonitrile can be seen in the relative intensities of O 1s and N 1s peaks in Figure 35(a)-(b).

The Mo 3d spectrum of MoS_2 treated in acetonitrile is shown in Figure 34(a). The presence of the oxidation state Mo^{6+} at 225.8 eV suggests that the laser treatment in ambient conditions can functionalize the NPs with oxygen, despite the fact that little oxygen is expected in the acetonitrile solvent (Li *et al.*, 2017). MoS_2 characteristic XPS peaks are also found at 229.4, 232.3, 235 eV owing to Mo $3d_{3/2}$, Mo $3d_{5/2}$, and S 2p respectively (Li *et al.*, 2017). The S 2p spectrum in Figure 34(b) confirmed the carbon functionalization of the MoS_2 NPs laser-treated in acetonitrile. Carbon-sulfur bonds C – SO, C – S(O) – C, and C – SO_2 were situated at 167, 168.1, and 170.1 eV, respectively (Ibrahim *et al.*, 2018). Nitrogen functionalization of the MoS_2 NPs was confirmed by the dominant N 1s spectrum shown in the N 1s spectrum in Figure 34(c) and the XPS survey in Figure 35(c). The N 1s spectrum includes =N-, NH, and N^+ peaks at 397.7, 399, and 399.8 eV respectively (Maity, Mandal and Nandi, 2017). The compositions of the characteristic peaks are demonstrated in Table 7.

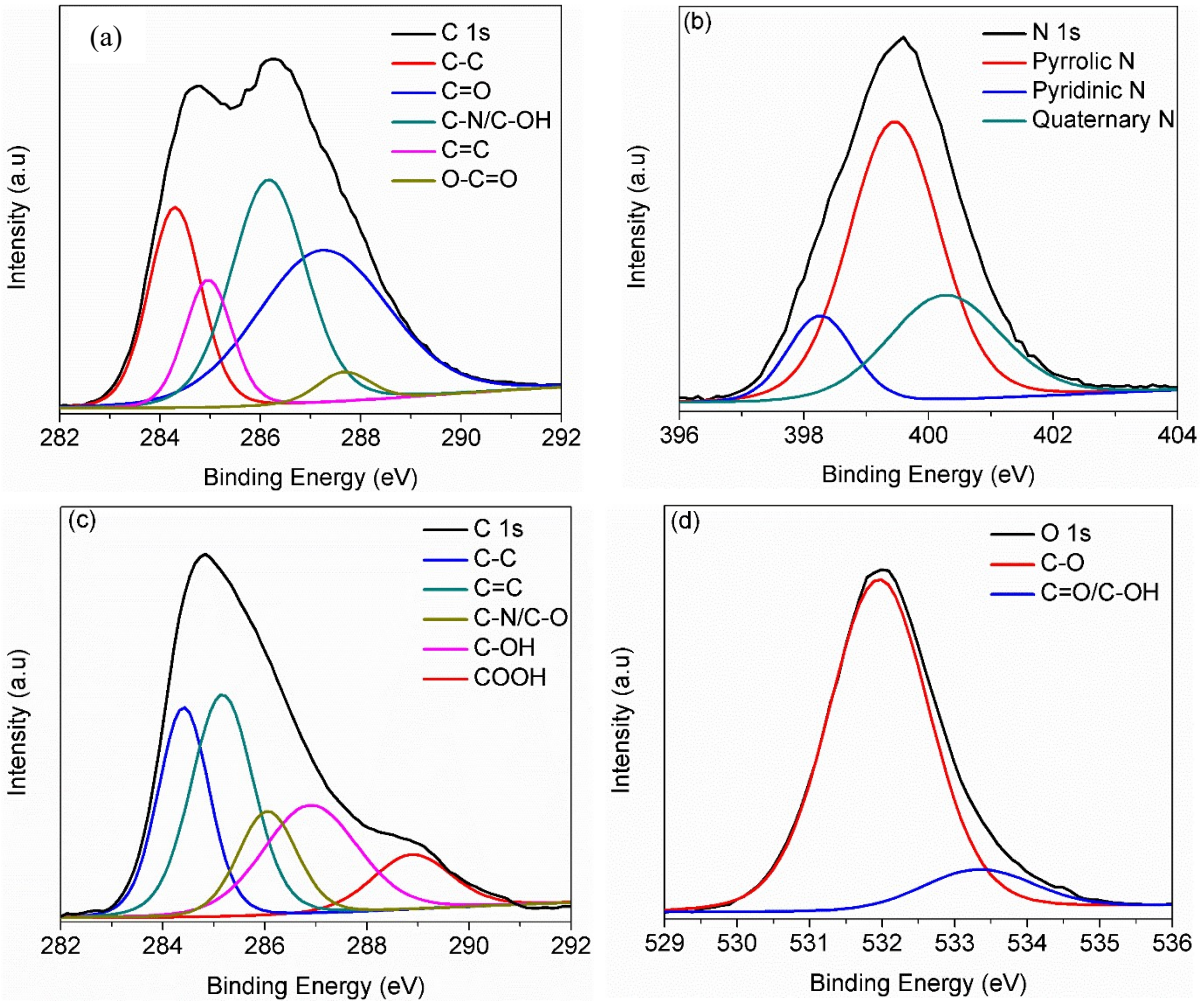

Figure 33. XPS spectra deconvoluted (a) C 1s of NGO in acetonitrile, (b) N 1s of NGO in acetonitrile, (c) C 1s of NGO in ethanol-water, and (d) O 1s of NGO in ethanol-water.

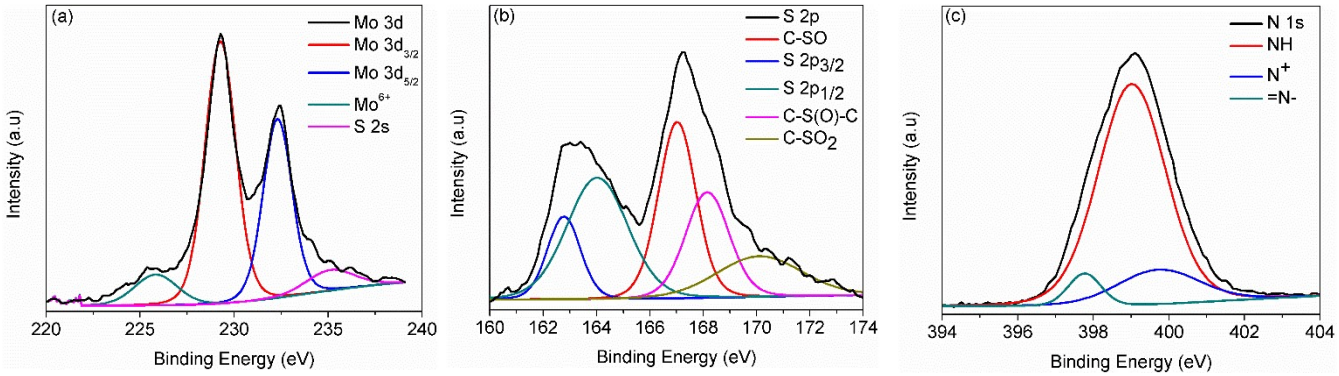

Figure 34. MoS_2 NPs treated in Acetonitrile XPS confirming nitrogen and carbon functionalization (a) Mo 3d, (b) S 2p, and (c) N 1s spectra.

Summary of compositions

Table 5. C 1s (upper row) and N 1s (lower row) compositions table of NGO NPs in acetonitrile

C – C	C=C	C – N/ C – OH	C=O	O – C=O
19.23%	11.02%	30.65%	36.30%	2.80%
Pyridinic N	**Pyrrolic N**	**Quaternary N**		
13.25%	59.18%	27.57%		

Table 6. C 1s (upper row) and O 1s (lower row) compositions table of NGO NPs in ethanol-water

C – C	C=C	C – N/C – O	C – OH	COOH
23.74%	30.57%	13.51%	22.67%	9.51%
C – O	**C=O/C – OH**			
88.08%	11.92%			

Table 7. S 2p (upper row) and Mo 3d (lower row) compositions table of MoS2 NPs in acetonitrile

$S\ 2p_{3/2}$	$S\ 2p_{1/2}$	C – SO	C – S(O) – C	$C – SO_2$
11.05%	29.83%	26.57%	18.61%	13.94%
Mo^{6+}	$Mo\ 3d_{3/2}$	$Mo\ 3d_{5/2}$	S 2s	
8.50%	51.97%	33.18%	6.35%	

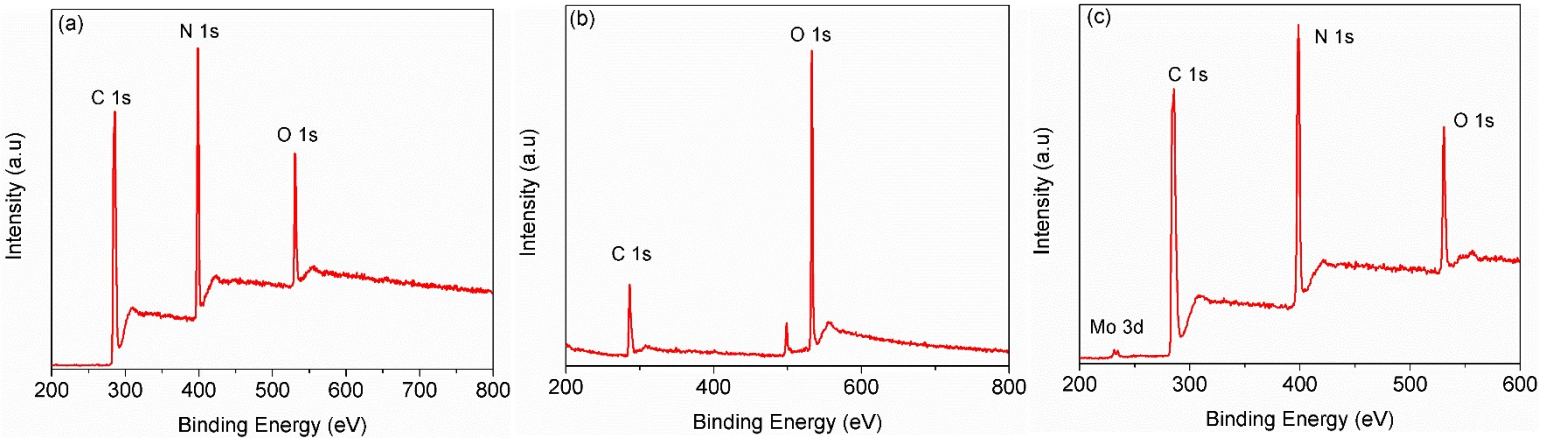

Figure 35. XPS survey of (a) NGO in acetonitrile, (b) NGO in ethanol-water, and (c) MoS_2 in acetonitrile

4.1.7 Transmission Electron Microscopy

TEM was used to investigate the atomic arrangement of MoS_2 NPs laser treated in acetonitrile and to observe the effects of the solvent functional groups on the structure of the NPs. The particle sizes averaged from 7 – 8 nm for 70 mins of laser treatment, as shown in Figure 36. The measured lattice spacing on one side of the particle in Figure 37 is 0.27 nm, which corresponds to the (100) faces of MoS_2 (Ibrahim *et al.*, 2018). However, the center of the same particle showed a lattice spacing of 0.25 nm, which can be attributed to the carbon domains attached to the NPs, consistent with the Raman Spectroscopy and XPS (Fasbender *et al.*, 2019). Vacancies are apparent on the surface of the NP in Figure 37 and one is examined using the lattice profile in the red box marked in Figure 38. Other measured lattice spacings on different locations of the NP in Figure 37 included 0.21 nm and 0.23 nm, which can be attributed to Mo – N bonds due to the nitrogen atom substitution and Mo – S bonds, respectively (Azcatl *et al.*, 2016). The contrast in Figure 37 is consistent with atoms on the surface of

the NPs, owing to the functional groups from the solvent. The vacancy seen in Figure 38 is consistent with the rapid and high energetic process of the laser treatment.

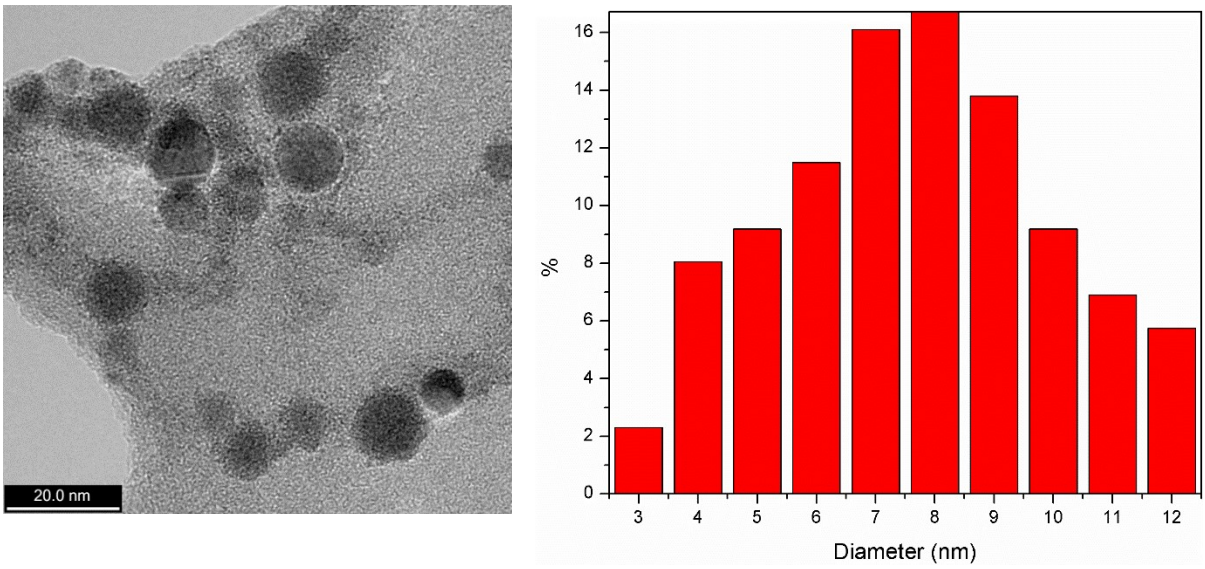

Figure 36. TEM image of the acetonitrile treated MoS_2 NPs and their size distribution

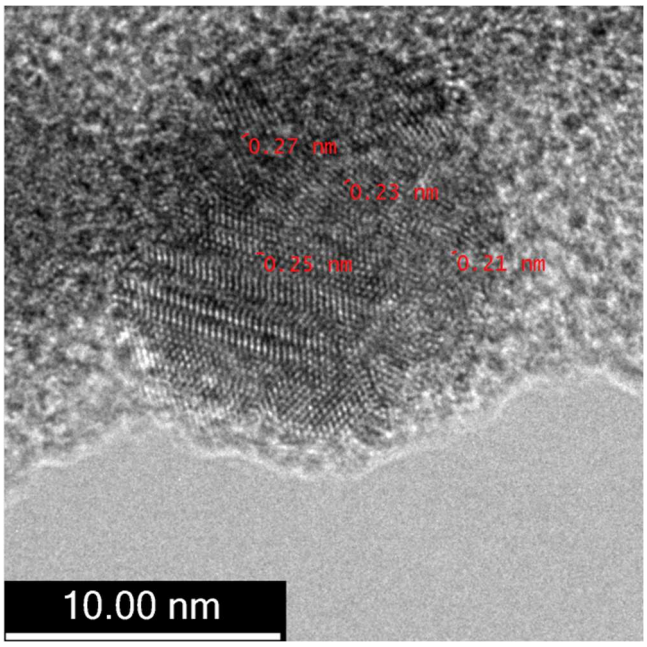

Figure 37. Different lattice spacings owing to the addition of different functional groups

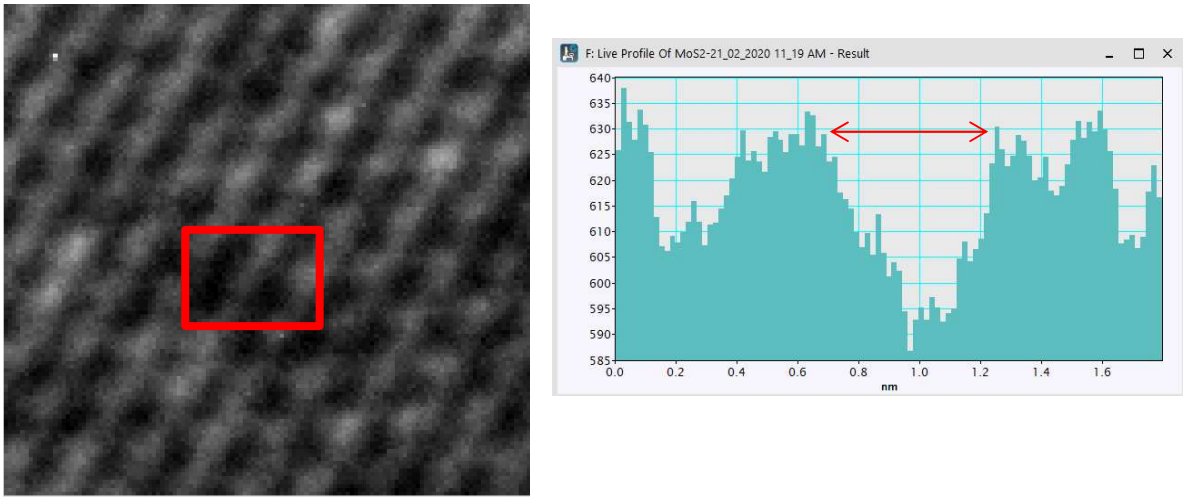

Figure 38. A spotted surface vacancy in a MoS_2 NP due to the rapid and highly energetic fs laser treatment process as seen in the right panel live profile.

4.2 Sensing Results

The characterization results indicate that the laser-treated NPs are functionalized by dissociated species from the solvent, producing NP solutions with hybrid properties (properties of both the host NPs and the functional groups). It is expected that the sensitivity of the NP sensors will be controlled by the degree of the functionalization and the affinity of the functional groups to the HMIs added to the solutions. The functional groups' attachment to the surface of the NPs is expected to have different bond polarities in each NP/solvent combination through charge transfer between the functional groups and the different NPs. Different polarities are expected to play a key role in capturing several HMIs selectively based on the NPs/functional groups net polarities and their HMIs electrostatic attraction strength as seen in Figure 39. The HMIs/functional groups' electrostatic attraction can reduce the number of photoexcited carriers, causing PL quenching as seen in Figure 40. Section 4.2.1 will discuss the best sensing results based on the linearity of luminescence quenching and highest sensitivity. The selectivity of the NP solutions sensors will be investigated in section 4.2.2, and section 4.2.3 will discuss the role of the functional groups in sensing the HMIs.

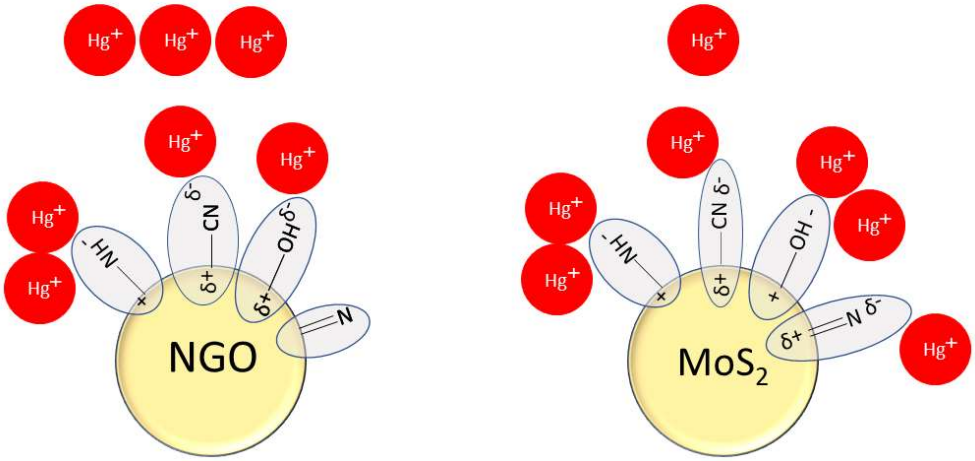

Figure 39. NGO and MoS_2 NPs treated in acetonitrile sensing Hg. The identical functional groups attached to the periphery of both NPs possess different bond polarities that influence the interaction of the functionalized NPs with Hg^+.

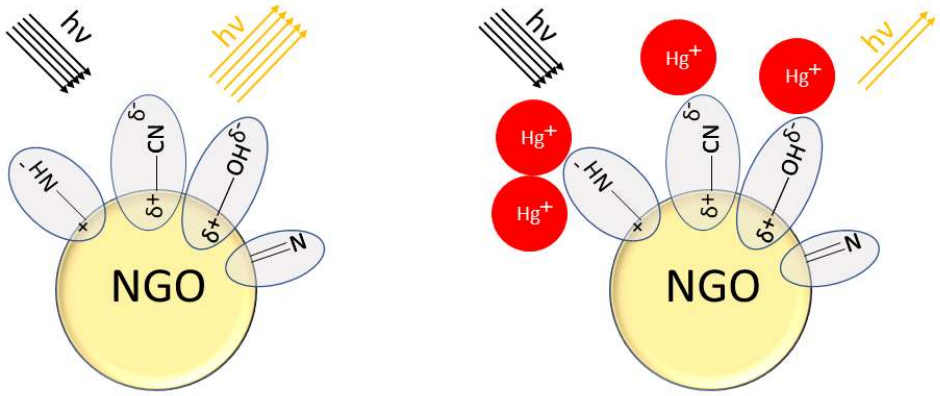

Figure 40. PL quenching due to the interaction of Hg^+ ions with the negatively charged nitrogen and hydroxyl functional groups attached to the periphery of NGO NPs.

4.2.1 Sensitivity

NGO in acetonitrile sensing Hg^{2+}

Figure 41(a) shows the PL of the NGO NPs laser treated in acetonitrile being quenched as Hg^{2+} is added. The onset of the sensing experiment using 0.1 µM Hg^{2+} showed a strong luminescence quenching and followed a linear quenching behavior up to saturation at 10 µM Hg^{2+}. Figure 41(b) shows the PL intensity plotted versus the Hg^{2+} concentration. The calculated LOD is 3 nM and the quenching factor, the ratio of the saturation quenching luminescence intensity and the blank luminescence intensity, described as $1 - F/F_0$ was found to be 0.58.

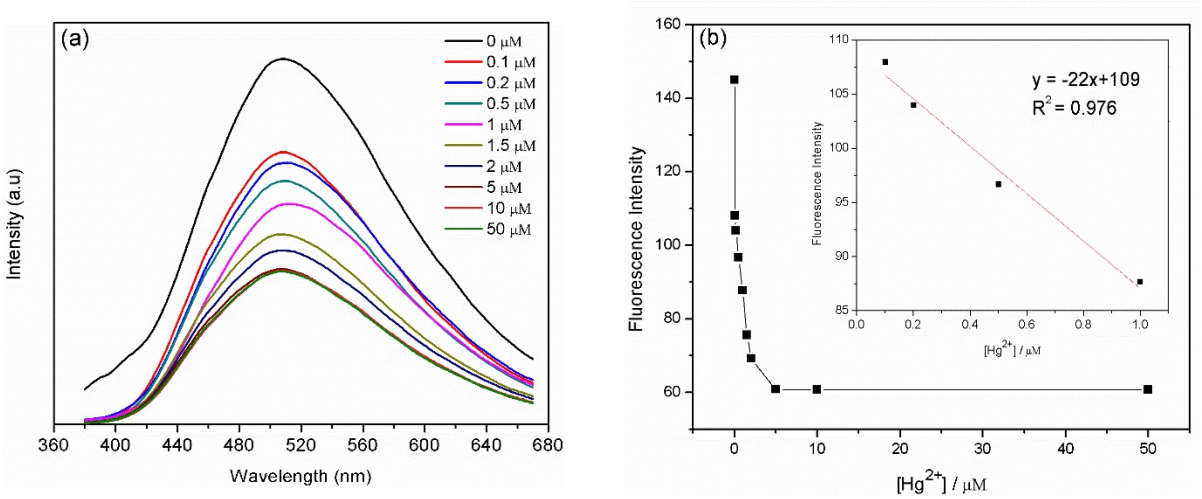

Figure 41. Hg^{2+} sensing (a) fluorescence quenching and (b) calibration curve.

NGO in acetonitrile sensing As^{3+}

Using the same approach, NGO NPs laser treated in acetonitrile sensed As^{3+} with a calculated LOD of 4.68 nM and a quenching factor of 0.56 (Figure 42). However, the sensing experiment didn't possess a strong linear correlation for the As^{3+} concentrations tested.

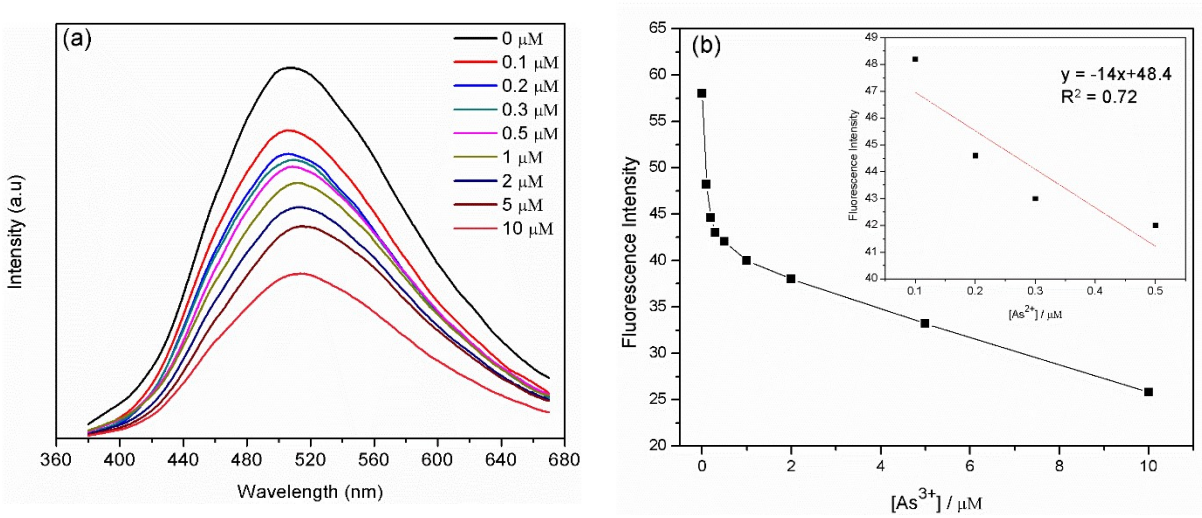

Figure 42. As^{3+} sensing (a) fluorescence quenching and (b) calibration curve.

NGO in ethanol-water sensing Cd^{2+}

Cd^{2+} sensing was most responsive and linear using NGO NPs laser treated in the ethanol-water mixture. A LOD of 1.48 nM and a quenching factor of 0.5 were determined in Figure 43.

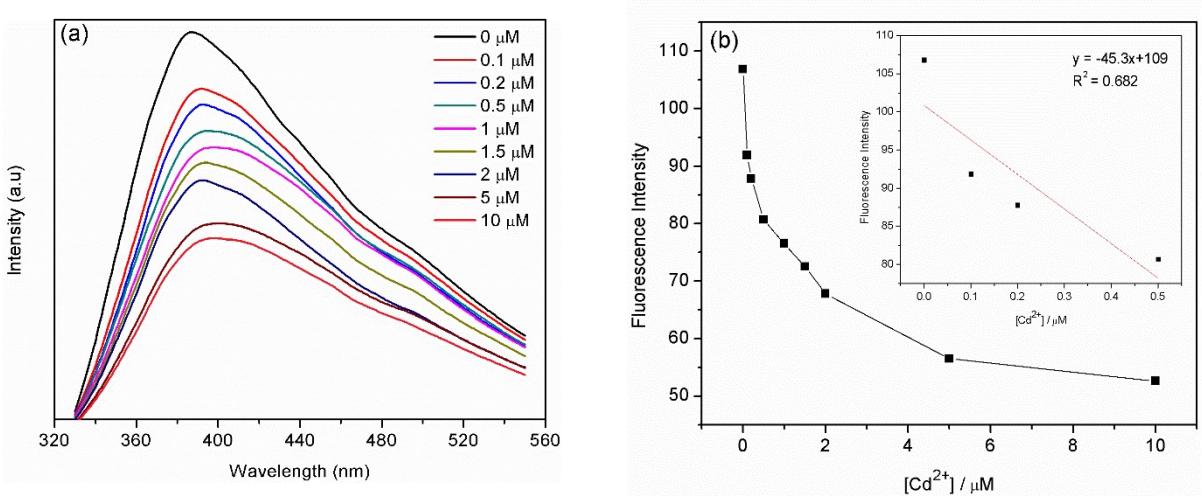

Figure 43. Cd^{2+} sensing (a) fluorescence quenching and (b) calibration curve.

MoS_2 in acetonitrile sensing Pb^{2+}

The MoS_2 NP solution functionalized by acetonitrile sensed Pb^{2+} with a LOD of 1.76 nM and a quenching factor of 0.64 with a strong linear correlation (Figure 44). The luminescence quenching was mainly influenced by the intensity decrease of the 385 nm main peak, more than the quenching observed in the nitrogen functionalization shoulder in the 450 – 550 nm range.

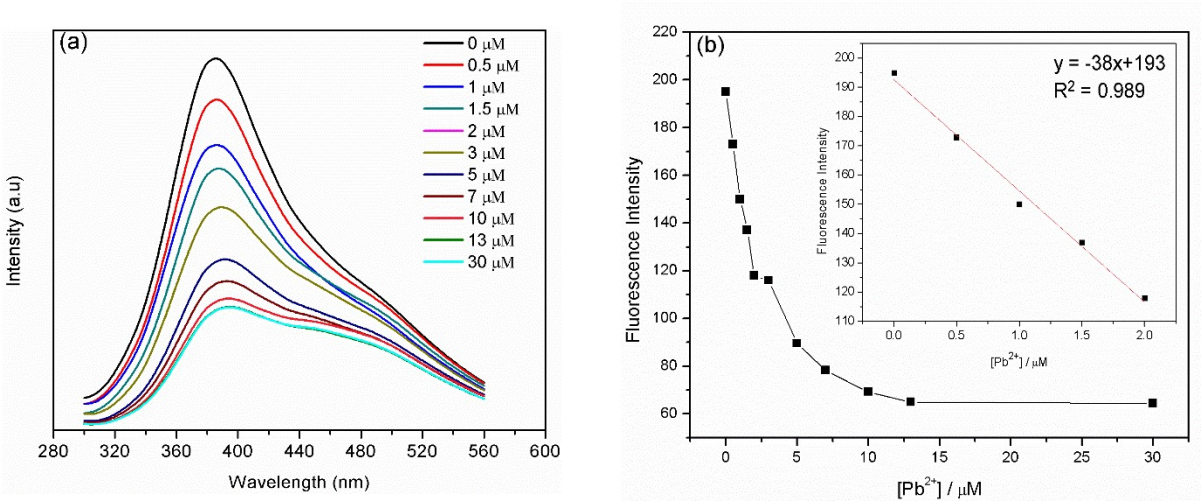

Figure 44. Pb^{2+} sensing (a) fluorescence quenching and (b) calibration curve.

MoS_2 in acetonitrile sensing Hg^{2+}

The MoS_2 NPs solution functionalized by acetonitrile also sensed Hg with a very low LOD of 0.56 nM and a quenching factor of 0.87 with a weak linear correlation (Figure 45). Upon the addition of 10 μM Hg^{2+}, the luminescence was strongly quenched, mainly owing to the main MoS_2 luminescence peak.

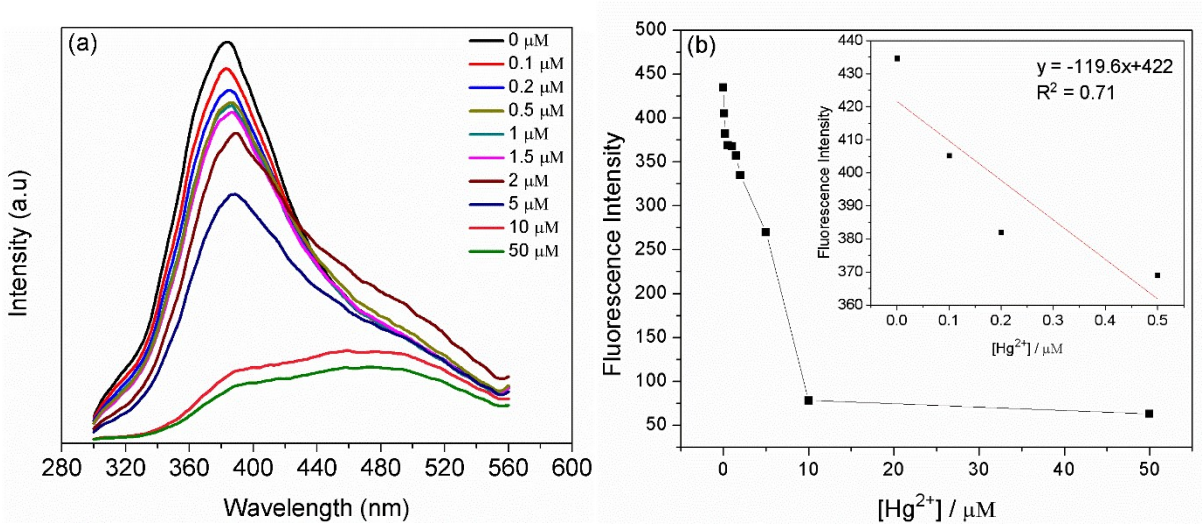

Figure 45. Hg^{2+} sensing (a) fluorescence quenching and (b) calibration curve.

4.2.2 Selectivity

The functional groups attached to the NPs allowed the sensing of different HMIs, however, the interaction of those functional groups with the host NPs is different in each case, allowing selective sensing of HMIs based on the quenching factor and the slope of the calibration curve. The selectivity of the NP solutions towards the different heavy metals is shown in the quenching factor bar graphs in Figure 46(a)-(c). An example of limited quenching is shown in Figure 46(d), where the PL spectrum of NGO treated in acetonitrile is largely unchanged as Pb^{2+} is added and the quenching factor was calculated to be 0.18 only. Quenching factor bar graphs (Figure 46(a)-(c)) showed that MoS_2/acetonitrile is selective to Hg^{2+} and Pb^{2+}, NGO/ethanol-water is selective to Cd^{2+}, and NGO/acetonitrile is selective to As^{3+} and Hg^{2+}. Other HMIs/NPs combinations did not possess stable linear quenching as the fluorescence was turned on and off randomly with different added HMIs. The selectivity of NP solutions for sensing multiple HMIs can be determined through the difference in the slopes as summarized in Table 9 in Section 4.2.4.

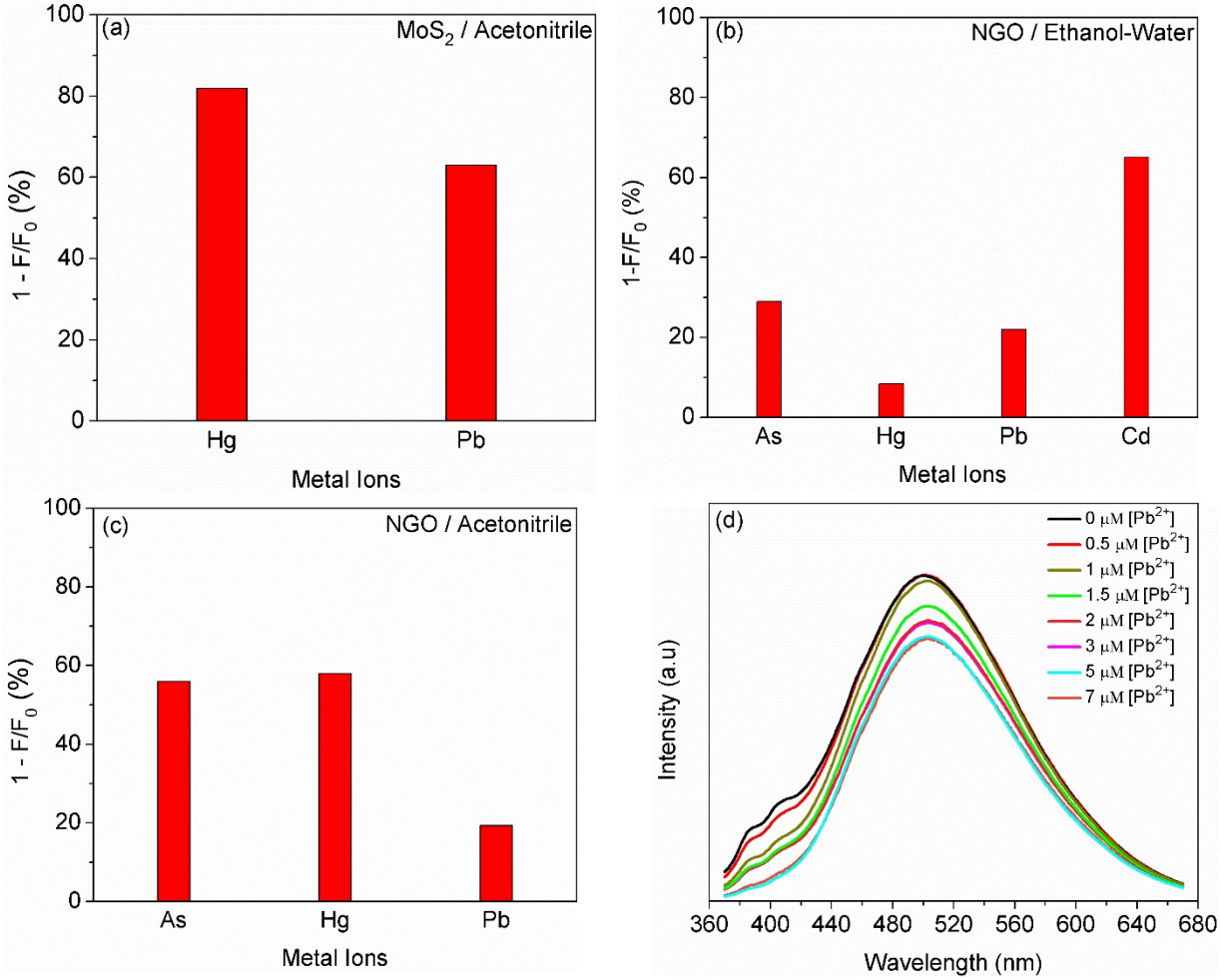

Figure 46. Quenching factor bar graphs of (a) MoS_2 / acetonitrile, (b) NGO / ethanol-water, and (c) NGO / acetonitrile. (d) Limited quenching of NGO / acetonitrile after adding Pb^{2+}.

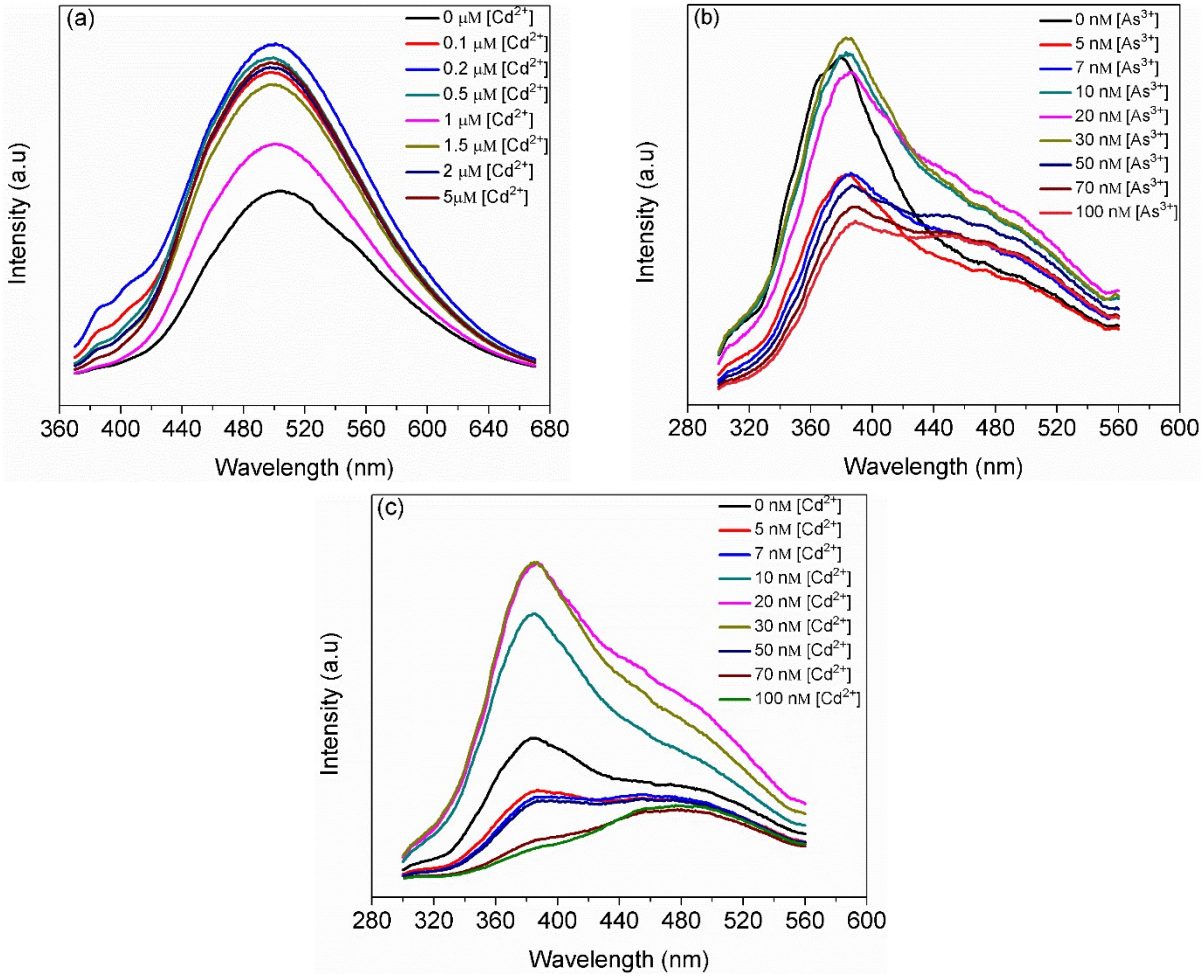

Figure 47. Nonlinear fluorescence quenching of (a) NGO / acetonitrile with added Cd^{2+}, (b) MoS_2 / acetonitrile with added As^{3+}, and (c) MoS_2 / acetonitrile with added Cd^{2+}.

4.2.3 Sensing mechanisms

FTIR Analysis

FTIR spectroscopy was used to study the role of the functional groups in the luminescence quenching and sensing. By examining the FTIR spectra of the laser treated NPs in the absence and presence of the HMIs, insight about the chemical affinity between the functional groups and the HMIs can be obtained. Clear and distinctive FTIR spectra were obtained for NGO and MoS_2 treated in acetonitrile, however, NGO treated in ethanol-water had a noisy FTIR spectrum, so it was not presented in this section. The

FTIR spectrum of NGO NPs in acetonitrile (black curve in Figure 48) showed characteristic C – H bending peaks in the range of 700 – 920 cm^{-1} (Černý, 1995) and C – O and C=O stretching peaks at 1035 and 1830 cm^{-1}, respectively (Schnitzer *et al.*, 2007)(Crowder, 1972). The nitrogen functional groups were observed in the FTIR spectrum as N – H bending, C=N stretch, and CN functional groups at 1635, 2245, and 2070 cm^{-1}, respectively (Alhazmi, 2019)(Kulesza *et al.*, 1996). Hydroxyl functional groups produced a characteristic peak at 3163 cm^{-1}, confirming the presence of oxygen functional groups as mentioned in the XPS analysis (Dovbeshko *et al.*, 2000). Adding 10 µM of As^{3+} caused several changes in the FTIR spectrum including an intensity reduction of the 746, 920, 1035, 1830, and 2245 cm^{-1} peaks, which is attributed to the interaction of the functional groups with the arsenic ions. In addition, the positions of oxygen-based peaks were shifted, implying that charge transfer happens between electron-rich oxygen functional groups and the HMIs, which could be expected to decrease the number of carriers in the NPs and lead to luminescence quenching (Alhazmi, 2019).

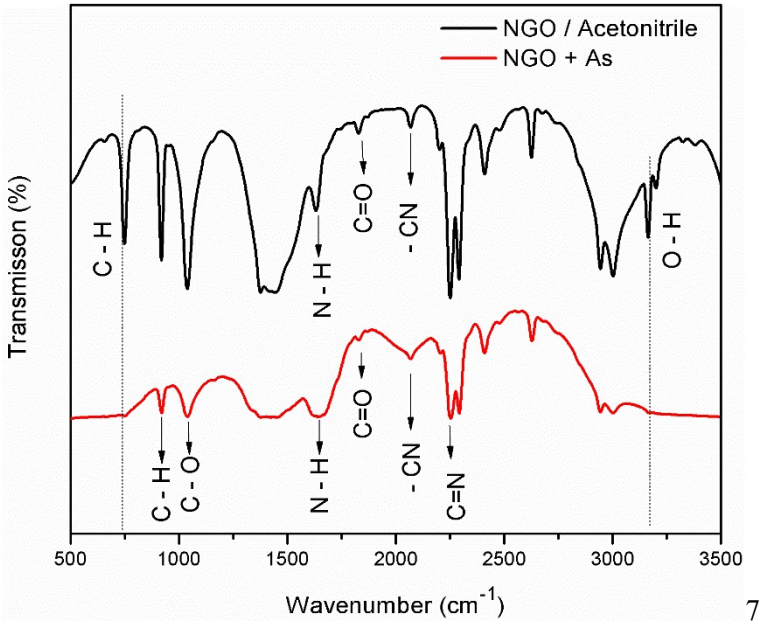

Figure 48. FTIR spectrum of NGO NPs in acetonitrile without (black curve) and with (red curve) the addition of As^{3+}.

Using the same analysis, the FTIR spectra of NGO NPs treated in acetonitrile with and without adding 50 µM Hg^{2+} in Figure 49 showed a reduction in the O – H peak at 3165 cm^{-1}, which is attributed

to the affinity of oxygen and mercury. The broadening and shifting of the 1630 and 2070 cm^{-1} nitrogen-based peaks suggests that the amine groups facilitate charge transfer with the Hg^{2+}.

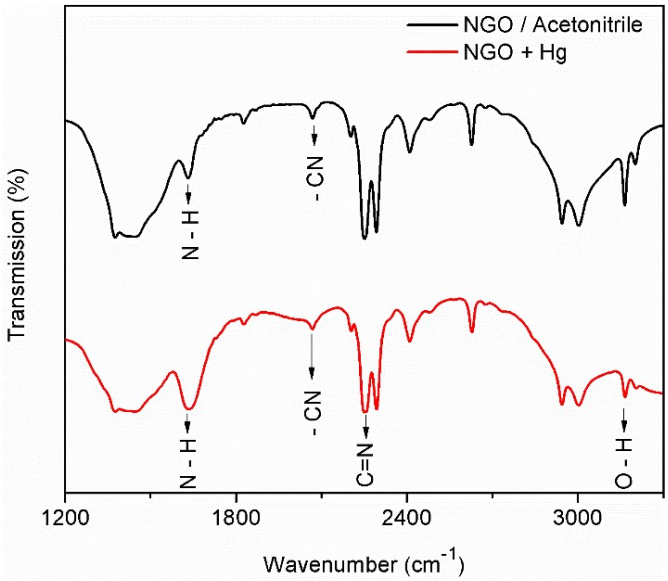

Figure 49. FTIR spectrum of NGO NPs in acetonitrile without (black curve) and with (red curve) the addition of Hg^{2+}.

MoS_2 NPs possessed a similar FTIR spectrum to NGO NPs due to laser treatment in the same solvent, however, the changes in the spectrum were different due to the nature of the interactions of the functional groups with MoS_2 compared to NGO NPs. Figure 50 shows the FTIR spectra of MoS_2 NPs laser treated in acetonitrile with and without Pb^{2+} added. Adding 30 µM Pb^{2+} resulted in an intensity reduction of the C=N 2250 cm^{-1} peak, which is attributed to the interaction of nitrogen functional groups with Pb^{2+}. A slight intensity reduction of the (O – H)-based 2941 and 3001 cm^{-1} peaks occurred, emphasizing the role of the hydroxyl groups attached to the surface of the NPs in sensing. A significant broadening of the N – H 1632 and 3533 and 3625 cm^{-1} O – H peaks also suggests that the charge transfer processes occur between Pb^{2+} and the oxygen functional groups attached to the periphery of the NPs, which may reduce the photoluminescence intensity of the NPs.

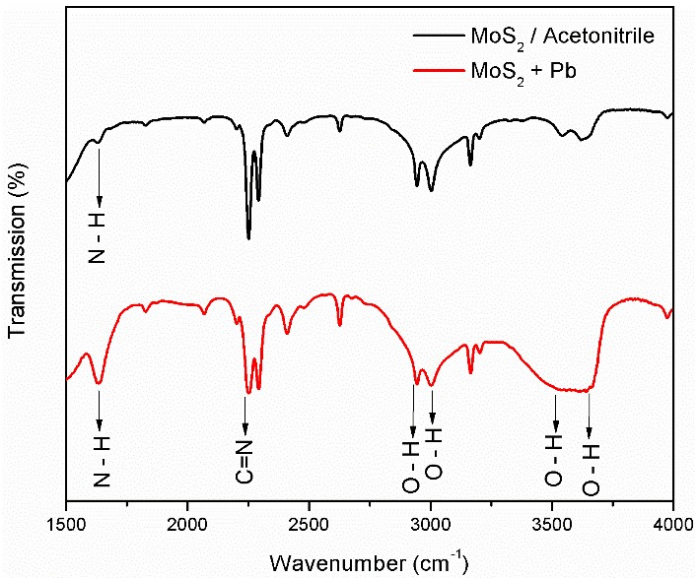

Figure 50. FTIR spectrum of MoS_2 NPs in acetonitrile without (black curve) and with (red curve) the addition of Pb^{2+}.

Similarly, the FTIR spectra of MoS_2 NPs laser treated in acetonitrile with and without 50 µM of Hg^{2+} ions added are shown in Figure 51. Broadening of the O – H (3625 cm^{-1}) peak, a reduced intensity of the C=N (2245 cm^{-1}) peak and broadening of the N – H (1627 cm^{-1}) peak are seen. The broadening of the O – H and N – H peaks may explain the luminescence quenching through charge transfer and a decreased number of photoexcited carriers, as mentioned earlier. However, sensing Hg^{2+} using MoS_2 treated in acetonitrile resulted in different changes in the FTIR spectrum than for sensing Hg^{2+} using NGO treated in acetonitrile (Figure 49), despite the presence of the same functional groups. This result shows how the different polarities of the bonds between the functional groups and different NPs results in distinctive sensing mechanisms.

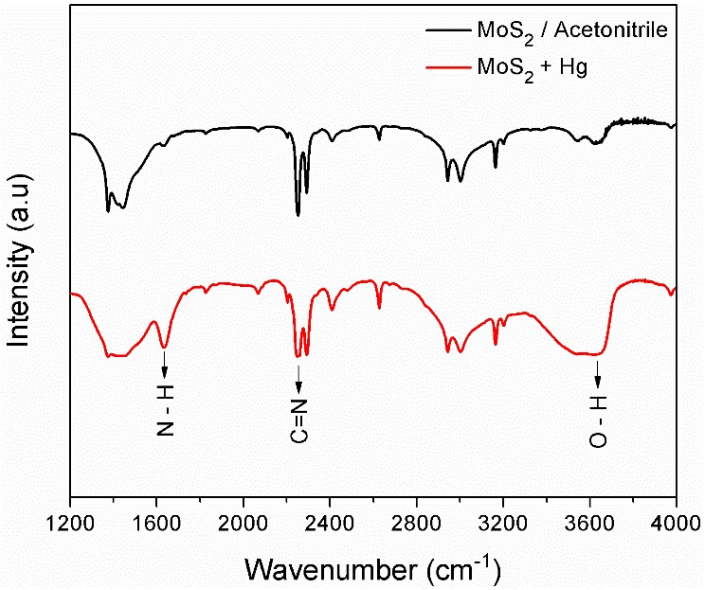

Figure 51. FTIR spectrum of MoS_2 NPs in acetonitrile without (black curve) and with (red curve) the addition of Hg^{2+}.

Photoluminescence lifetime decay

PL lifetime decay measurements of NGO treated in ethanol-water were carried to determine the type of quenching process upon the addition of 10 µM Cd^{2+} and to investigate the role of the oxygen functional groups in sensing Cd^{2+} through the non-radiative pathways created upon the oxygen-$Cd2^{+}$ charge transfer interaction.

The PL lifetime decay of NGO treated in ethanol-water without the addition of Cd^{2+} is shown as the red trace in Figure 52 and is fit with a biexponential decay $A_1 e^{-t/\tau_1} + A_2 e^{-t/\tau_2}$ with τ_1 = 0.65 ns (A_1=98.02%) and τ_2 = 2.8 ns (A_2=1.98%). The average lifetime based on the decay components and amplitudes was found to be $(A_1*\tau_1) + (A_2*\tau_2)$ = 0.69 ns. The addition of Cd (blue trace) slowed the PL decay to τ_1 = 0.708 ns (97.08%) and τ_2 = 3.42 ns (2.92%), leading to an average lifetime decay of 0.79 ns. The added Cd^{2+} increased the lifetime decay components (while reducing the PL intensity), which suggested that the luminescence quenching was a static quenching process (Radhakrishnan and Panneerselvam, 2018). Static quenching refers to the luminescence quenching due to ground state interactions between the added ions and the functional groups attached to the periphery of the host material (Fraiji, Hayes and Werner, 1992).

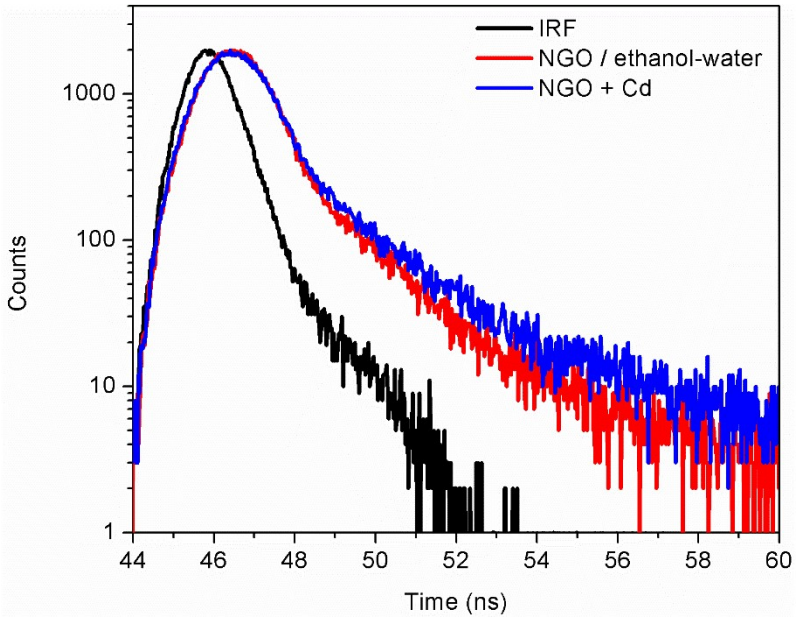

Figure 52. Lifetime decay plot of NGO in ethanol-water with and without added Cd^{2+}.

4.2.4 Summary of results

The fs laser treated NPs possessed dominant solvent-based functional groups that aided their utilization as fluorescence-quenching HMI sensors. The results showed sensitive and selective sensing of the four most toxic heavy metals using NGO treated in acetonitrile and ethanol-water and MoS_2 treated in acetonitrile. The LODs of the sensors were below 5 nM, which is approximately 3 times less than the safe limit recommended by the WHO. Table 8 summarizes the LODs and the functional groups responsible for the sensing (based on FTIR analysis). The functional groups form bonds with the NPs with different polarities. This leads to selective sensing of HMIs based on the affinity of the HMIs towards the bonds with particular polarities, as shown in Figure 39. The shifted FTIR peaks indicated charge transfer between the HMIs and the functional groups, which is expected to reduce the number of photoexcited carriers and quench the PL as described in Figure 40. The selectivity results can be expressed by the quenching factor and the sensing calibration slope as summarized in Table 9.

Table 8. Summary of FTIR results.

HMIs	Material	LOD	Functional Groups
Hg^{2+}	NGO / Acetonitrile	3 nM	O – H, -CN
	MoS_2 / Acetonitrile	0.56 nM	C – H, O – H, C=N
As^{3+}	NGO / Acetonitrile	4.68 nM	C – H, N – H, C=O, C – O, -CN
Pb^{2+}	MoS_2 / Acetonitrile	1.76 nM	C=N, O – H, N – H
Cd^{2+}	NGO / ethanol-water	1.48 nM	O – H, COOH

Table 9. Selectivity table.

HMIs	Material	Slope	Quenching Factor
NGO / Acetonitrile	Hg^{2+}	-22	0.58
	As^{3+}	-14	0.56
MoS_2 / Acetonitrile	Hg^{2+}	-119.57	0.87
	Pb^{2+}	-38	0.64
NGO / ethanol-water	Cd^{2+}	-45	0.5

Chapter 5
Conclusion

Given the hazards of toxic HMIs presented by the WHO, a simple and sensitive sensing tool is required to detect those HMIs with very low concentrations (< 15 nM) to prevent danger to aquatic and human lives. In this work, a fs laser technique was used to synthesize sensing NP solutions in less than 2 hours. The laser treatment allowed the size reduction of 2D materials into sub 10 nm NPs modified with functional groups originating from the solvent. Acetonitrile and 1:1 ethanol-water solvents were used as laser treatment solvents because of the high affinity of Hg, Pb, As, and Cd to carboxylic, hydroxyl, and amine groups. The produced NPs possessed hybrid properties, as observed by UV-Vis spectroscopy, PL spectroscopy, and TEM, owing to the intrinsic properties of the NPs and the solvent-originating functional groups. Raman and X-ray photoelectron spectroscopy affirmed the presence of the functional groups and the dominant functionalization with oxygen and nitrogen using ethanol-water and acetonitrile, respectively.

The fs laser technique is powerful in controlling the degree of the functionalization of the NPs, allowing a high degree of freedom in engineering the properties of the NPs to be used in HMI sensing and other applications. The interaction of the functional groups with the NPs and the degree of functionalization allowed sensitive and selective sensing of the four most toxic heavy metals with LODs less than 5 nm, allowing early detection of the HMIs before exceeding the safe limit suggested by the WHO. FTIR spectroscopy analysis of the functionalized NPs before and after the addition of HMIs showed that specific functional groups interact preferentially with the different HMIs, enabling sensitive and selective sensing. Broadening and shifting of FTIR peaks indicated charge transfer between the functional bonds and different HMIs, consistent with the PL quenching sensing mechanism. The photoluminescence lifetime decay analysis of NGO treated in ethanol-water demonstrated the role of the surface carboxylic and hydroxyl groups in Cd sensing, whereby binding of Cd to these groups appears to result in immediate charge transfer of some of the photoexcited charges and instantaneous PL quenching.

To our knowledge, the current state of the art in sensing HMIs using QDs and nanosheets has not shown a study sensing the four most toxic HMIs using one technique. In addition, most of the previous studies used QD or NP synthesis techniques that demanded 4 – 24 hours of synthesis time. In this study,

selective and sensitive sensing of HMIs was achieved via the rapid fs laser treatment process. A comparison of this work with the current state of the art is shown in Table 10.

Table 10. Current state of the art compared to this work

Ref	Material	HMIs	Selectivity	LOD (nM)	Mechanism	Fabrication
(Gu, Pei, *et al.*, 2017)	BP - QDs	Hg	Selective	0.39	Inner-filter effect	Solvothermal – 12 hr
(Kumar *et al.*, 2017)	C Dots	Pb	Selective	0.59	Binding affinity with functional groups	Hydrothermal – 4 hr
(Lin *et al.*, 2019)	MoS_2 - QDs	Co, Cd, Pb	Selective	Pb 0.84, Cd, 99.6	Binding energy change based on functionalization	Hydrothermal – 8 hr
(Radhakrishnan and Panneerselvam, 2018)	C dots	As	Selective	2.3	Oxygen surface interaction	Solvothermal – 12 hr
(Li *et al.*, 2013)	MoS_2/FAM-DNA nanosheets	As	Selective	18	Surface aptamer affinity to As	Solvothermal – 24 hr
(Shorie *et al.*, 2019)	gCN - QDs	Hg	x	250	Trapping of Hg in the nitrogen defect centers in carbon	Microwave reactor tube – 5 mins
This work	MoS_2 NGO	**Hg, Pb, Cd, As**	Selective	**0.56 1.76 1.48 4.68**	Functional groups charge transfer with HMIs	**Fs laser treatment for 70 and 100 mins**

Chapter 6
Future work

The absorption and PL spectra of the laser treated NPs in different solvents showed a drastic change in their properties, implying the dominance of the solvent-based functionalization over the intrinsic properties of the host materials. The XPS analysis of MoS_2 laser treated in acetonitrile further confirmed that the intensities of the C 1s, N 1s, and O 1s spectra of the solvent-originating functional groups are stronger than those of Mo 3d and S 2p. TEM analysis also showed lattice spacings owing to the graphitic and Mo – N configurations, explaining the high degree of functionalization of the NPs. The degree of functionalization could be controlled by varying the concentration of the 2D materials in the solvent, where higher concentrations of 2D NPs would possess less abundant functional groups. Despite the high sensitivities reported here, the detection selectivity could be enhanced by changing the concentration of the 2D flakes dissolved in acetonitrile, allowing different charge transfer dynamics between the functional groups and the NPs.

The capability of the fs laser technique in producing NPs with hybrid properties depending on the solvent allows the usage of different solvents to functionalize the NPs differently to sensitively and selectively sense HMIs. Another promising step could be adding salt additives to the NP solution prior to laser treatment to enhance the selectivity and functionality of the produced NP sensors. For example, HMIs tend to form compounds with chlorine ions, so the addition of NaCl to the solution and the fs laser dissociation of the dissolved salt into Na^+ and Cl^- could further enhance the selectivity by forming chlorine-NP bonds. Varying the fs laser properties including the power and laser treatment time can produce NPs with different sizes that can interact differently with functional groups essential for HMIs sensing. Above all else, using the NPs solutions for testing real aquatic samples contaminated with HMIs is a promising step towards commercializing the NPs solutions.

Chapter 7
Contributions

Jones, A., Kao, M., Mistry, K., Shahin, A., Yavuz, M. and Musselman, K., 2020. In-situ spatial and temporal electrical characterization of ZnO thin films deposited by atmospheric pressure chemical vapour deposition on flexible polymer substrates. *Scientific Reports*.

Yeow, T., Mistry, K., Shahin, A., Yavuz, M. and Musselman, K., 2020. Atmospheric-pressure spatial chemical vapor deposition of tungsten oxide. *Journal of Vacuum Science & Technology A*, 38(5).

Bibliography

Acik, M. and Chabal, Y. J. (2012) 'A Review on Reducing Graphene Oxide for Band Gap Engineering', *Journal of Materials Science Research*, 2(1), pp. 101–112. doi: 10.5539/jmsr.v2n1p101.

Akinwande, D. *et al.* (2017) 'A review on mechanics and mechanical properties of 2D materials—Graphene and beyond', *Extreme Mechanics Letters*, 13, pp. 42–77. doi: https://doi.org/10.1016/j.eml.2017.01.008.

Alhazmi, H. A. (2019) 'FT-IR spectroscopy for the identification of binding sites and measurements of the binding interactions of important metal ions with bovine serum albumin', *Scientia Pharmaceutica*, 87(1). doi: 10.3390/scipharm87010005.

Amani, M. *et al.* (2015) 'Near-unity photoluminescence quantum yield in MoS2', *Science*, 350(6264), pp. 1065–1068. doi: 10.1126/science.aad2114.

Anichini, C. *et al.* (2018) 'Chemical sensing with 2D materials', *Chem. Soc. Rev.* The Royal Society of Chemistry, 47(13), pp. 4860–4908. doi: 10.1039/C8CS00417J.

Ben Aoun, S. (2020) 'Nanostructured carbon electrode modified with N-doped graphene quantum dots–chitosan nanocomposite: a sensitive electrochemical dopamine sensor', *Royal Society Open Science*. Royal Society, 4(11), p. 171199. doi: 10.1098/rsos.171199.

Azcatl, A. *et al.* (2016) 'Covalent Nitrogen Doping and Compressive Strain in MoS2 by Remote N2 Plasma Exposure', *Nano Letters*. American Chemical Society, 16(9), pp. 5437–5443. doi: 10.1021/acs.nanolett.6b01853.

Bai, J. *et al.* (2010) 'Graphene nanomesh', *Nature Nanotechnology*, 5(3), pp. 190–194. doi: 10.1038/nnano.2010.8.

Balog, R. *et al.* (2010) 'Bandgap opening in graphene induced by patterned hydrogen adsorption', *Nature Materials*, 9(4), pp. 315–319. doi: 10.1038/nmat2710.

Banhart, F., Kotakoski, J. and Krasheninnikov, A. V (2011) 'Structural Defects in Graphene', *ACS Nano*. American Chemical Society, 5(1), pp. 26–41. doi: 10.1021/nn102598m.

Bansod, B. *et al.* (2017) 'A review on various electrochemical techniques for heavy metal ions detection with different sensing platforms', *Biosensors & bioelectronics*. CSIR-Central

Scientific Instruments Organisation, Chandigarh 160030, India. Electronic address: csiobabankumar@gmail.com., 94, pp. 443–455. doi: 10.1016/j.bios.2017.03.031.

Bartolucci, S. F. *et al.* (2011) 'Graphene–aluminum nanocomposites', *Materials Science and Engineering: A*, 528(27), pp. 7933–7937. doi: https://doi.org/10.1016/j.msea.2011.07.043.

Batmunkh, M. *et al.* (2019) 'Microwave-assisted synthesis of black phosphorus quantum dots: Efficient electrocatalyst for oxygen evolution reaction', *Journal of Materials Chemistry A*. Royal Society of Chemistry, 7(21), pp. 12974–12978. doi: 10.1039/c9ta02513h.

Baykal, A. (2014) 'Solvothermal Synthesis of Pure SrFe12O19 Hexaferrite Nanoplatelets', *Journal of Superconductivity and Novel Magnetism*, 27(3), pp. 877–880. doi: 10.1007/s10948-013-2369-z.

Berkelbach, T. C., Hybertsen, M. S. and Reichman, D. R. (2013) 'Theory of neutral and charged excitons in monolayer transition metal dichalcogenides', *Physical Review B*. American Physical Society, 88(4), p. 45318. doi: 10.1103/PhysRevB.88.045318.

Bhargava, R. and Khan, S. (2018) 'Structural, optical and dielectric properties of graphene oxide', *AIP Conference Proceedings*, 1953. doi: 10.1063/1.5032346.

Buscema, M. *et al.* (2014) 'Fast and Broadband Photoresponse of Few-Layer Black Phosphorus Field-Effect Transistors', *Nano Letters*. American Chemical Society, 14(6), pp. 3347–3352. doi: 10.1021/nl5008085.

Buso, D. *et al.* (2008) 'Gold Nanoparticle-Doped TiO2 Semiconductor Thin Films: Gas Sensing Properties', *Advanced Functional Materials*. John Wiley & Sons, Ltd, 18(23), pp. 3843–3849. doi: 10.1002/adfm.200800864.

Buzica, D. *et al.* (2006) 'Comparison of voltammetry and inductively coupled plasma-mass spectrometry for the determination of heavy metals in PM10 airborne particulate matter', *Atmospheric Environment*, 40(25), pp. 4703–4710. doi: https://doi.org/10.1016/j.atmosenv.2006.04.015.

Cai, Y. *et al.* (2016) 'Highly Itinerant Atomic Vacancies in Phosphorene', *Journal of the American Chemical Society*. American Chemical Society, 138(32), pp. 10199–10206. doi: 10.1021/jacs.6b04926.

Carolin, C. F. *et al.* (2017) 'Efficient techniques for the removal of toxic heavy metals from aquatic environment: A review', *Journal of Environmental Chemical Engineering*, 5(3), pp. 2782–2799. doi:

https://doi.org/10.1016/j.jece.2017.05.029.

Černý, J. (1995) ‘ALIPHATIC C-H BOND RESPONSES IN THE 900-700 cm−1 REGION OF THE FTIR SPECTRA OF COAL TARS’, *Fuel Science and Technology International*. Taylor & Francis, 13(6), pp. 807–818. doi: 10.1080/08843759508947707.

Chen, P. *et al.* (2017) ‘The rising star of 2D black phosphorus beyond graphene: synthesis, properties and electronic applications’, *2D Materials*. IOP Publishing, 5(1), p. 14002. doi: 10.1088/2053-1583/aa8d37.

Chen, W. *et al.* (1997) ‘Thermoluminescence of ZnS nanoparticles’, *Applied Physics Letters*, 70(11), pp. 1465–1467. doi: 10.1063/1.118563.

Chen, W. (2008) ‘Nanoparticle fluorescence based technology for biological applications’, *Journal of Nanoscience and Nanotechnology*, 8(3), pp. 1019–1051. doi: 10.1166/jnn.2008.301.

Chhowalla, M., Liu, Z. and Zhang, H. (2015) ‘Two-dimensional transition metal dichalcogenide (TMD) nanosheets’, *Chemical Society Reviews*. Royal Society of Chemistry, 44(9), pp. 2584–2586. doi: 10.1039/c5cs90037a.

Conde, J., Doria, G. and Baptista, P. (2012) ‘Noble Metal Nanoparticles Applications in Cancer’, *Journal of Drug Delivery*. Edited by P. C. de Morais. Hindawi Publishing Corporation, 2012, p. 751075. doi: 10.1155/2012/751075.

Crowder, G. A. (1972) ‘Infrared and Raman spectra of pentafluoropropionic acid’, *Journal of Fluorine Chemistry*, 1(4), pp. 385–389. doi: https://doi.org/10.1016/S0022-1139(00)82959-0.

Culver, B. R. and Surles, T. (1975) ‘Interference of molecular spectra due to alkali halides in nonflame atomic absorption spectrometry’, *Analytical Chemistry*. American Chemical Society, 47(6), pp. 920–921. doi: 10.1021/ac60356a037.

Das, S. K. *et al.* (2012) ‘Synthesis{,} characterization and catalytic activity of gold nanoparticles biosynthesized with Rhizopus oryzae protein extract’, *Green Chem.* The Royal Society of Chemistry, 14(5), pp. 1322–1334. doi: 10.1039/C2GC16676C.

Dong, H. *et al.* (2016) ‘Fluorescent MoS2 Quantum Dots: Ultrasonic Preparation, Up-Conversion and Down-Conversion Bioimaging, and Photodynamic Therapy’, *ACS Applied Materials & Interfaces*. American Chemical Society, 8(5), pp. 3107–3114. doi: 10.1021/acsami.5b10459.

Dovbeshko, G. I. *et al.* (2000) ‘FTIR spectroscopy studies of nucleic acid damage’, *Talanta*, 53(1),

pp. 233–246. doi: https://doi.org/10.1016/S0039-9140(00)00462-8.

Dressler, V. L., Pozebon, D. and Curtius, A. J. (1998) 'Determination of heavy metals by inductively coupled plasma mass spectrometry after on-line separation and preconcentration', *Spectrochimica Acta Part B: Atomic Spectroscopy*, 53(11), pp. 1527–1539. doi: https://doi.org/10.1016/S0584-8547(98)00180-3.

Du, K. *et al.* (2020) 'High-quality black phosphorus quantum dots fabricated via microwave-tailored technology', *Nanomaterials*, 10(1). doi: 10.3390/nano10010139.

Dvorak, M., Oswald, W. and Wu, Z. (2013) 'Bandgap Opening by Patterning Graphene', *Scientific Reports*, 3(1), p. 2289. doi: 10.1038/srep02289.

Elgallal, M., Fletcher, L. and Evans, B. (2016) 'Assessment of potential risks associated with chemicals in wastewater used for irrigation in arid and semiarid zones: A review', *Agricultural Water Management*. Elsevier B.V., 177, pp. 419–431. doi: 10.1016/j.agwat.2016.08.027.

Engel, M., Steiner, M. and Avouris, P. (2014) 'Black Phosphorus Photodetector for Multispectral, High-Resolution Imaging', *Nano Letters*. American Chemical Society, 14(11), pp. 6414–6417. doi: 10.1021/nl502928y.

Fan, W. *et al.* (2016) 'Water-compatible graphene oxide/molecularly imprinted polymer coated stir bar sorptive extraction of propranolol from urine samples followed by high performance liquid chromatography-ultraviolet detection', *Journal of Chromatography A*, 1443, pp. 1–9. doi: https://doi.org/10.1016/j.chroma.2016.03.017.

Fang, H. *et al.* (2013) 'Degenerate n-Doping of Few-Layer Transition Metal Dichalcogenides by Potassium', *Nano Letters*. American Chemical Society, 13(5), pp. 1991–1995. doi: 10.1021/nl400044m.

Fasbender, S. *et al.* (2019) 'The Low Toxicity of Graphene Quantum Dots is Reflected by Marginal Gene Expression Changes of Primary Human Hematopoietic Stem Cells', *Scientific Reports*, 9(1), p. 12028. doi: 10.1038/s41598-019-48567-6.

Favron, A. *et al.* (2015) 'Photooxidation and quantum confinement effects in exfoliated black phosphorus', *Nature Materials*, 14(8), pp. 826–832. doi: 10.1038/nmat4299.

Fraiji, L. K., Hayes, D. M. and Werner, T. C. (1992) 'Static and dynamic fluorescence quenching experiments for the physical chemistry laboratory', *Journal of Chemical Education*. American

Chemical Society, 69(5), p. 424. doi: 10.1021/ed069p424.

Gao, F. *et al.* (2019) 'Tuning the photoluminescence of graphene oxide quantum dots by photochemical fluorination', *Carbon*, 141, pp. 331–338. doi: https://doi.org/10.1016/j.carbon.2018.09.068.

Gattass, R. R. and Mazur, E. (2008) 'Femtosecond laser micromachining in transparent materials', *Nature Photonics*, 2(4), pp. 219–225. doi: 10.1038/nphoton.2008.47.

Gu, W., Pei, X., *et al.* (2017) 'Black Phosphorus Quantum Dots as the Ratiometric Fluorescence Probe for Trace Mercury Ion Detection Based on Inner Filter Effect', *ACS Sensors*, 2(4), pp. 576–582. doi: 10.1021/acssensors.7b00102.

Gu, W., Yan, Y., *et al.* (2017) 'Fluorescent black phosphorus quantum dots as label-free sensing probes for evaluation of acetylcholinesterase activity', *Sensors and Actuators, B: Chemical*. Elsevier B.V., 250, pp. 601–607. doi: 10.1016/j.snb.2017.05.017.

Guo, J., Zhou, M. and Yang, C. (2017) 'Fluorescent hydrogel waveguide for on-site detection of heavy metal ions', *Scientific Reports*, 7(1), p. 7902. doi: 10.1038/s41598-017-08353-8.

He, X., Gao, L. and Ma, N. (2013) 'One-Step Instant Synthesis of Protein-Conjugated Quantum Dots at Room Temperature', *Scientific Reports*, 3(1), p. 2825. doi: 10.1038/srep02825.

Ibrahim, K. H. *et al.* (2018) 'Simultaneous Fabrication and Functionalization of Nanoparticles of 2D Materials with Hybrid Optical Properties', *Advanced Optical Materials*, 6(11), pp. 1–7. doi: 10.1002/adom.201701365.

Jayanthi, K. *et al.* (2007) 'Structural, optical and photoluminescence properties of ZnS: Cu nanoparticle thin films as a function of dopant concentration and quantum confinement effect', *Crystal Research and Technology*. John Wiley & Sons, Ltd, 42(10), pp. 976–982. doi: 10.1002/crat.200710950.

Jiang, S. *et al.* (2015) 'Highly sensitive detection of mercury(II) ions with few-layer molybdenum disulfide', *Nano Research*, 8(1), pp. 257–262. doi: 10.1007/s12274-014-0658-x.

Jiang, Y. *et al.* (2018) 'Contamination levels and human health risk assessment of toxic heavy metals in street dust in an industrial city in Northwest China', *Environmental Geochemistry and Health*, 40(5), pp. 2007–2020. doi: 10.1007/s10653-017-0028-1.

De Jong, W. H. and Borm, P. J. A. (2008) 'Drug delivery and nanoparticles:applications and hazards',

International journal of nanomedicine. Dove Medical Press, 3(2), pp. 133–149. doi: 10.2147/ijn.s596.

Kanazawa, M. *et al.* (2019) 'Effects of the solvent during the preparation of MoS2 nanoparticles by laser ablation', *Journal of Physics: Conference Series*, 1230(1). doi: 10.1088/1742-6596/1230/1/012100.

Khan, Ibrahim, Saeed, K. and Khan, Idrees (2019) 'Nanoparticles: Properties, applications and toxicities', *Arabian Journal of Chemistry*. The Authors, 12(7), pp. 908–931. doi: 10.1016/j.arabjc.2017.05.011.

Kiraly, B. *et al.* (2017) 'Probing Single Vacancies in Black Phosphorus at the Atomic Level', *Nano Letters*. American Chemical Society, 17(6), pp. 3607–3612. doi: 10.1021/acs.nanolett.7b00766.

Kulesza, P. J. *et al.* (1996) 'In Situ FT-IR/ATR Spectroelectrochemistry of Prussian Blue in the Solid State', *Analytical Chemistry*. American Chemical Society, 68(14), pp. 2442–2446. doi: 10.1021/ac950380k.

Kumar, A. *et al.* (2017) 'Green synthesis of carbon dots from Ocimum sanctum for effective fluorescent sensing of Pb2+ ions and live cell imaging', *Sensors and Actuators, B: Chemical*. Elsevier B.V., 242, pp. 679–686. doi: 10.1016/j.snb.2016.11.109.

Kunkel, R. and Manahan, S. E. (1973) 'Atomic absorption analysis of strong heavy metal chelating agents in water and waste water', *Analytical Chemistry*. American Chemical Society, 45(8), pp. 1465–1468. doi: 10.1021/ac60330a024.

Lee, C. W., Suh, J. M. and Jang, H. W. (2019) 'Chemical Sensors Based on Two-Dimensional (2D) Materials for Selective Detection of Ions and Molecules in Liquid', *Frontiers in Chemistry*, 7, p. 708. doi: 10.3389/fchem.2019.00708.

Levenson, R. *et al.* (2001) *More Modern Chemical Techniques*. The Royal Society of Chemistry.

Li, B. *et al.* (2017) 'Preparation of Monolayer MoS2 Quantum Dots using Temporally Shaped Femtosecond Laser Ablation of Bulk MoS2 Targets in Water', *Scientific Reports*, 7(1), p. 11182. doi: 10.1038/s41598-017-10632-3.

Li, L. *et al.* (2014) 'Black phosphorus field-effect transistors', *Nature Nanotechnology*, 9(5), pp. 372–377. doi: 10.1038/nnano.2014.35.

Li, M. *et al.* (2013) 'Detection of lead (II) with a "turn-on" fluorescent biosensor based on energy transfer from CdSe/ZnS quantum dots to graphene oxide', *Biosensors and Bioelectronics*. Elsevier,

43(1), pp. 69–74. doi: 10.1016/j.bios.2012.11.039.

Li, X.-B. *et al.* (2015) 'Structures, stabilities and electronic properties of defects in monolayer black phosphorus', *Scientific Reports*, 5(1), p. 10848. doi: 10.1038/srep10848.

Lin, T. W. *et al.* (2019) 'Fluorescence turn-on chemosensors based on surface-functionalized MoS2 quantum dots', *Sensors and Actuators, B: Chemical*. Elsevier, 281(November 2018), pp. 659–669. doi: 10.1016/j.snb.2018.11.009.

Liu, M. *et al.* (2017) 'Boron Nitride Quantum Dots with Solvent-Regulated Blue/Green Photoluminescence and Electrochemiluminescent Behavior for Versatile Applications', *Advanced Optical Materials*. John Wiley & Sons, Ltd, 5(3), p. 1600661. doi: 10.1002/adom.201600661.

Liu, P. *et al.* (2016) 'Flower-like N-doped MoS2for photocatalytic degradation of RhB by visible light irradiation', *Nanotechnology*. IOP Publishing, 27(22), p. 225403. doi: 10.1088/0957-4484/27/22/225403.

Long, F. *et al.* (2013) 'Rapid on-site/in-situ detection of heavy metal ions in environmental water using a structure-switching DNA optical biosensor', *Scientific Reports*, 3(1), p. 2308. doi: 10.1038/srep02308.

Lopez-Bezanilla, A. (2016) 'Effect of atomic-scale defects and dopants on phosphorene electronic structure and quantum transport properties', *Physical Review B*. American Physical Society, 93(3), p. 35433. doi: 10.1103/PhysRevB.93.035433.

Lv, W. *et al.* (2018) 'Sulfur-Doped Black Phosphorus Field-Effect Transistors with Enhanced Stability', *ACS Applied Materials & Interfaces*. American Chemical Society, 10(11), pp. 9663–9668. doi: 10.1021/acsami.7b19169.

Ma, B. C. *et al.* (2015) 'Conjugated microporous polymer nanoparticles with enhanced dispersibility and water compatibility for photocatalytic applications', *Journal of Materials Chemistry A*. Royal Society of Chemistry, 3(31), pp. 16064–16071. doi: 10.1039/c5ta03820k.

Maity, N., Mandal, A. and Nandi, A. K. (2017) 'High dielectric poly(vinylidene fluoride) nanocomposite films with MoS2 using polyaniline interlinker via interfacial interaction', *J. Mater. Chem. C*. The Royal Society of Chemistry, 5(46), pp. 12121–12133. doi: 10.1039/C7TC03593D.

Miao, J., Zhang, L. and Wang, C. (2019) 'Black phosphorus electronic and optoelectronic devices', *2D Materials*. IOP Publishing, 6(3), p. 32003. doi: 10.1088/2053-1583/ab1ebd.

Mokhtar Mohamed, M. *et al.* (2018) 'Nitrogen Graphene: A New and Exciting Generation of Visible Light Driven Photocatalyst and Energy Storage Application', *ACS Omega*. American Chemical Society, 3(2), pp. 1801–1814. doi: 10.1021/acsomega.7b01806.

Musselman, K. P., Ibrahim, K. H. and Yavuz, M. (2018) 'Research Update: Beyond graphene - Synthesis of functionalized quantum dots of 2D materials and their applications', *APL Materials*, 6(12). doi: 10.1063/1.5067250.

Needleman, S. B. and Romberg, R. W. (1990) 'Limits of linearity and detection for some drugs of abuse.', *Journal of analytical toxicology*. England, 14(1), pp. 34–38. doi: 10.1093/jat/14.1.34.

Nguyen, V. *et al.* (2019) 'Facile synthesis of photoluminescent MoS2 and WS2 quantum dots with strong surface-state emission', *Journal of Luminescence*. Elsevier B.V., 214(February), p. 116554. doi: 10.1016/j.jlumin.2019.116554.

Novoa-De León, I. C. *et al.* (2019) 'Tuning the luminescence of nitrogen-doped graphene quantum dots synthesized by pulsed laser ablation in liquid and their use as a selective photoluminescence on–off–on probe for ascorbic acid detection', *Carbon*, 150, pp. 455–464. doi: https://doi.org/10.1016/j.carbon.2019.05.057.

O'Brien, M. *et al.* (2014) 'Plasma assisted synthesis of WS2 for gas sensing applications', *Chemical Physics Letters*, 615, pp. 6–10. doi: https://doi.org/10.1016/j.cplett.2014.09.051.

Ouyang, W. *et al.* (2019) 'Chapter 5 - Nanoparticles within functional frameworks and their applications in photo(electro)catalysis', in Prieto, J. P. and Béjar, M. G. B. T.-P. I. N. (eds) *Micro and Nano Technologies*. Elsevier, pp. 109–138. doi: https://doi.org/10.1016/B978-0-12-814531-9.00005-1.

Ozhukil Valappil, M. *et al.* (2018) 'A single-step, electrochemical synthesis of nitrogen doped blue luminescent phosphorene quantum dots', *Chemical Communications*. Royal Society of Chemistry, 54(83), pp. 11733–11736. doi: 10.1039/c8cc07266c.

Ping, J. *et al.* (2017) 'Recent Advances in Sensing Applications of Two-Dimensional Transition Metal Dichalcogenide Nanosheets and Their Composites', *Advanced Functional Materials*. John Wiley & Sons, Ltd, 27(19), p. 1605817. doi: 10.1002/adfm.201605817.

Porrès, L. *et al.* (2006) 'Absolute measurements of photoluminescence quantum yields of solutions using an integrating sphere', *Journal of Fluorescence*, 16(2), pp. 267–273. doi: 10.1007/s10895-005-

0054-8.

Rabchinskii, M. K. *et al.* (2020) ‘Graphene oxide conversion into controllably carboxylated graphene layers via photoreduction process in the inert atmosphere’, *Fullerenes, Nanotubes and Carbon Nanostructures*. Taylor & Francis, 28(3), pp. 221–225. doi: 10.1080/1536383X.2019.1686625.

Radhakrishnan, K. and Panneerselvam, P. (2018) ‘Green synthesis of surface-passivated carbon dots from the prickly pear cactus as a fluorescent probe for the dual detection of arsenic(iii) and hypochlorite ions from drinking water’, *RSC Advances*. Royal Society of Chemistry, 8(53), pp. 30455–30467. doi: 10.1039/c8ra05861j.

Rakibuddin, M. and Kim, H. (2019) ‘Reduced graphene oxide supported C3N4 nanoflakes and quantum dots as metal-free catalysts for visible light assisted CO2 reduction’, *Beilstein Journal of Nanotechnology*, 10, pp. 448–458.

Rasheed, T. *et al.* (2018) ‘Fluorescent sensor based models for the detection of environmentally-related toxic heavy metals’, *Science of The Total Environment*, 615, pp. 476–485. doi: https://doi.org/10.1016/j.scitotenv.2017.09.126.

Ravikumar, A. *et al.* (2018) ‘MoS 2 nanosheets as an effective fluorescent quencher for successive detection of arsenic ions in aqueous system’, *Applied Surface Science*. Elsevier B.V., 449, pp. 31–38. doi: 10.1016/j.apsusc.2017.12.098.

Robinson, J. T. *et al.* (2008) ‘Reduced Graphene Oxide Molecular Sensors’, *Nano Letters*. American Chemical Society, 8(10), pp. 3137–3140. doi: 10.1021/nl8013007.

Schmidt, H., Giustiniano, F. and Eda, G. (2015) ‘Electronic transport properties of transition metal dichalcogenide field-effect devices: surface and interface effects’, *Chem. Soc. Rev.* The Royal Society of Chemistry, 44(21), pp. 7715–7736. doi: 10.1039/C5CS00275C.

Schnitzer, M. I. *et al.* (2007) ‘The conversion of chicken manure to biooil by fast pyrolysis I. Analyses of chicken manure, biooils and char by 13C and 1H NMR and FTIR spectrophotometry’, *Journal of Environmental Science and Health, Part B*. Taylor & Francis, 42(1), pp. 71–77. doi: 10.1080/03601230601020894.

Shi, X. *et al.* (2007) ‘Improved biocompatibility of surface functionalized dendrimer-entrapped gold nanoparticles’, *Soft Matter*, 3(1), pp. 71–74. doi: 10.1039/b612972b.

Shih, T.-T. *et al.* (2016) ‘A high-throughput solid-phase extraction microchip combined with

inductively coupled plasma-mass spectrometry for rapid determination of trace heavy metals in natural water.', *Analytica chimica acta*. Netherlands, 916, pp. 24–32. doi: 10.1016/j.aca.2016.02.027.

Shokry, A. *et al.* (2019) 'Highly Luminescent Ternary Nanocomposite of Polyaniline, Silver Nanoparticles and Graphene Oxide Quantum Dots', *Scientific Reports*, 9(1), p. 16984. doi: 10.1038/s41598-019-53584-6.

Shorie, M. *et al.* (2019) 'Graphitic carbon nitride QDs impregnated biocompatible agarose cartridge for removal of heavy metals from contaminated water samples', *Journal of Hazardous Materials*. Elsevier, 367(December 2018), pp. 629–638. doi: 10.1016/j.jhazmat.2018.12.115.

Stankovich, S. *et al.* (2007) 'Synthesis of graphene-based nanosheets via chemical reduction of exfoliated graphite oxide', *Carbon*, 45(7), pp. 1558–1565. doi: https://doi.org/10.1016/j.carbon.2007.02.034.

Su, S., Chen, S. and Fan, C. (2018) 'Recent advances in two-dimensional nanomaterials-based electrochemical sensors for environmental analysis', *Green Energy & Environment*, 3(2), pp. 97–106. doi: https://doi.org/10.1016/j.gee.2017.08.005.

Terrones, H., López-Urías, F. and Terrones, M. (2013) 'Novel hetero-layered materials with tunable direct band gaps by sandwiching different metal disulfides and diselenides', *Scientific Reports*, 3(1), p. 1549. doi: 10.1038/srep01549.

Thakar, R., Chen, Y. and Snee, P. T. (2007) 'Efficient Emission from Core/(Doped) Shell Nanoparticles: Applications for Chemical Sensing', *Nano Letters*. American Chemical Society, 7(11), pp. 3429–3432. doi: 10.1021/nl0719168.

Thirumalai, J., Jagannathan, R. and Trivedi, D. C. (2007) 'Y2O2S:Eu3+ nanocrystals, a strong quantum-confined luminescent system', *Journal of Luminescence*, 126(2), pp. 353–358. doi: 10.1016/j.jlumin.2006.08.064.

Toh, R. J. *et al.* (2017) '3R phase of MoS2 and WS2 outperforms the corresponding 2H phase for hydrogen evolution', *Chem. Commun.* The Royal Society of Chemistry, 53(21), pp. 3054–3057. doi: 10.1039/C6CC09952A.

Vilela, D. *et al.* (2016) 'Graphene-Based Microbots for Toxic Heavy Metal Removal and Recovery from Water', *Nano Letters*, 16(4), pp. 2860–2866. doi: 10.1021/acs.nanolett.6b00768.

Wang, D. H. *et al.* (2014) 'Holey reduced graphene oxide nanosheets for high performance room

temperature gas sensing', *Journal of Materials Chemistry A*. The Royal Society of Chemistry, 2(41), pp. 17415–17420. doi: 10.1039/C4TA03740E.

Wang, J. *et al.* (2020) 'PEGylated-folic acid-modified black phosphorus quantum dots as near-infrared agents for dual-modality imaging-guided selective cancer cell destruction', *Nanophotonics*, 9(8), pp. 2425–2435. doi: 10.1515/nanoph-2019-0506.

Wang, L. *et al.* (2011) 'Characteristics of Raman spectra for graphene oxide from ab initio simulations', *The Journal of Chemical Physics*. American Institute of Physics, 135(18), p. 184503. doi: 10.1063/1.3658859.

Wilschefski, S. C. and Baxter, M. R. (2019) 'Inductively Coupled Plasma Mass Spectrometry: Introduction to Analytical Aspects.', *The Clinical biochemist. Reviews*, 40(3), pp. 115–133. doi: 10.33176/AACB-19-00024.

Wu, F.-Y. *et al.* (2020) 'Nitrogen-doped MoS2 quantum dots: Facile synthesis and application for the assay of hematin in human blood', *Materials Science and Engineering: C*, 112, p. 110898. doi: https://doi.org/10.1016/j.msec.2020.110898.

Wu, G. *et al.* (2016) 'Carbon nanocomposite catalysts for oxygen reduction and evolution reactions: From nitrogen doping to transition-metal addition', *Nano Energy*, 29, pp. 83–110. doi: https://doi.org/10.1016/j.nanoen.2015.12.032.

Wu, J.-B. *et al.* (2018) 'Raman spectroscopy of graphene-based materials and its applications in related devices', *Chem. Soc. Rev.* The Royal Society of Chemistry, 47(5), pp. 1822–1873. doi: 10.1039/C6CS00915H.

Xia, F. *et al.* (2009) 'Ultrafast graphene photodetector', *Nature Nanotechnology*, 4(12), pp. 839–843. doi: 10.1038/nnano.2009.292.

Xia, F., Wang, H. and Jia, Y. (2014) 'Rediscovering black phosphorus as an anisotropic layered material for optoelectronics and electronics', *Nature Communications*, 5(1), p. 4458. doi: 10.1038/ncomms5458.

Xiang, Z. *et al.* (2014) 'Nitrogen-Doped Holey Graphitic Carbon from 2D Covalent Organic Polymers for Oxygen Reduction', *Advanced Materials*. John Wiley & Sons, Ltd, 26(20), pp. 3315–3320. doi: 10.1002/adma.201306328.

Xu, Y. *et al.* (2019) 'Fabrication of transition metal dichalcogenides quantum dots based on

femtosecond laser ablation', *Scientific Reports*. Springer US, 9(1), pp. 1–9. doi: 10.1038/s41598-019-38929-5.

Yadav, R. and Dixit, C. K. (2017) 'Synthesis, characterization and prospective applications of nitrogen-doped graphene: A short review', *Journal of Science: Advanced Materials and Devices*, 2(2), pp. 141–149. doi: https://doi.org/10.1016/j.jsamd.2017.05.007.

Yang, S. *et al.* (2012) 'Efficient Synthesis of Heteroatom (N or S)-Doped Graphene Based on Ultrathin Graphene Oxide-Porous Silica Sheets for Oxygen Reduction Reactions', *Advanced Functional Materials*. John Wiley & Sons, Ltd, 22(17), pp. 3634–3640. doi: 10.1002/adfm.201200186.

Yeh, T.-F. *et al.* (2014) 'Nitrogen-Doped Graphene Oxide Quantum Dots as Photocatalysts for Overall Water-Splitting under Visible Light Illumination', *Advanced Materials*. John Wiley & Sons, Ltd, 26(20), pp. 3297–3303. doi: 10.1002/adma.201305299.

Zhang, J., Xia, Z. and Dai, L. (2015) 'Carbon-based electrocatalysts for advanced energy conversion and storage', *Science Advances*, 1(7), p. e1500564. doi: 10.1126/sciadv.1500564.

Zhang, P. *et al.* (2018) 'Electrochimica Acta Large-scale synthesis of nitrogen doped MoS 2 quantum dots for ef fi cient hydrogen evolution reaction', *Electrochimica Acta*. Elsevier Ltd, 270, pp. 256–263. doi: 10.1016/j.electacta.2018.03.097.

Zhang, X. *et al.* (2015) 'Black Phosphorus Quantum Dots ** Angewandte', 210023, pp. 3653–3657. doi: 10.1002/anie.201409400.

Zhang, Y. *et al.* (2014) 'Direct observation of the transition from indirect to direct bandgap in atomically thin epitaxial MoSe 2', 9(February), pp. 111–115. doi: 10.1038/NNANO.2013.277.

Zhang, Y. *et al.* (2017) '2D Black Phosphorus for Energy Storage and Thermoelectric Applications', *Small*, 13(28), pp. 1–20. doi: 10.1002/smll.201700661.

Zhao, M. *et al.* (2017) 'MoS 2 Quantum Dots as New Electrochemiluminescence Emitters for Ultrasensitive Bioanalysis of Lipopolysaccharide'. doi: 10.1021/acs.analchem.7b01558.

Zhao, Y. *et al.* (2016) 'Surface Coordination of Black Phosphorus for Robust Air and Water Stability', *Angewandte Chemie International Edition*. John Wiley & Sons, Ltd, 55(16), pp. 5003–5007. doi: 10.1002/anie.201512038.

Zhou, S. Y. *et al.* (2007) 'Substrate-induced bandgap opening in epitaxial graphene', *Nature*

Materials, 6(10), pp. 770–775. doi: 10.1038/nmat2003.

Zhou, Z. Q. *et al.* (2018) 'Highly selective and sensitive detection of Hg2+ based on fluorescence enhancement of Mn-doped ZnSe QDs by Hg2+-Mn2+ replacement', *Sensors and Actuators, B: Chemical*. Elsevier B.V., 254, pp. 8–15. doi: 10.1016/j.snb.2017.07.033.

Zou, X., Liu, Y. and Yakobson, B. I. (2013) 'Predicting Dislocations and Grain Boundaries in Two-Dimensional Metal-Disulfides from the First Principles', *Nano Letters*. American Chemical Society, 13(1), pp. 253–258. doi: 10.1021/nl3040042.

Appendix A
Limit of detection calculation

Sensitivity (LOD) calculations are dependent on the accuracy of the instrument PL measurements and the calibration curve of the sensing data. HMIs detection sensitivity was quantified using LOD = 3σ/K, σ being the standard deviation of several blank NP PL intensities and K being the slope of the sensing calibration curve in the linear region. 8 blank NP PL measurements were recorded using the same measurement conditions (fixed sample, excitation wavelength, and slit width). For example, 8 blank measurements of MoS_2 NPs treated in acetonitrile were recorded as seen in Figure A-1 and the peak intensity values were determined and σ was calculated accordingly to be 0.023. Sensing calibration curves were expected to be linear in small HMIs concentration regions and saturated upon increasing the concentration of HMIs due to the saturation of HMI/NPs bonds. Accordingly, the first 3-5 sensing points were fitted linearly, and the slope K was determined from the fitted curve as seen in Figure 42 to be implemented in the LOD equation.

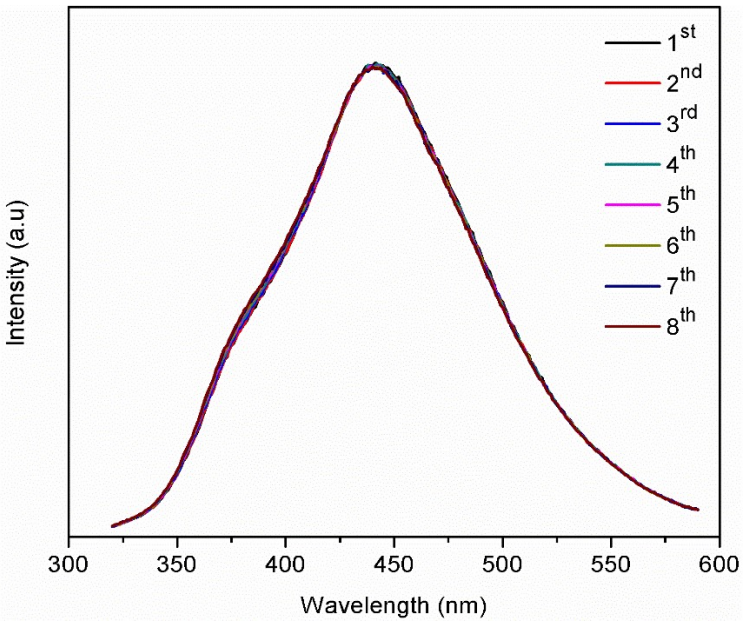

Figure A - 1. Determination of PL peak intensities S.D of 8 blank acetonitrile-treated MoS_2 NPs.